biophysica

MDPI

Article

HLA Binding Peptide-Based Designing of Non-Spike Universal Nanovaccine Against SARS-CoV-2: A Computational Approach

Puja Jaishwal and Satarudra Prakash Singh *

Department of Biotechnology, Mahatma Gandhi Central University, Motihari 845401, India; pujajaishwal26@gmail.com
* Correspondence: sprakashsingh@mgcub.ac.in

Abstract

The continuous evolution of the SARS-CoV-2 virus, marked by the emergence of new variants, poses a significant threat to the efficacy of existing vaccines. However, a promising approach to addressing vaccine failure caused by viral mutations (particularly in the spike protein) is the development of a variant-proof (conserved), non-spike, multiepitope universal nanostructure vaccine with multifunctionality, biocompatibility, self-adjuvanticity, and structural similarity to pathogens in terms of size and shape. This study aimed to design a self-assembled nanostructure vaccine (SANV) featuring pentameric and trimeric coiled-coil peptide motifs, as well as other functional motifs, including epitopes, TAT, PADRE, and adjuvant. The cytotoxic T lymphocyte (CTL), helper T lymphocyte (HTL), and B lymphocyte (BL) epitopes of SANV were screened from the IEDB with more than 50% individual predicted population coverage (PPC) and fused using linkers to enable self-assembly. The multimerization of the 24 SANV monomers was modeled using the GalaxyHomomer and AlphaFold web servers. Subsequently, the leading SANV constructs with (SANVa9) and without (SANVb6) adjuvant were analyzed for their physicochemical profiles and assessed for antigenicity, allergenicity, solubility, and antioxidant potential. Furthermore, the molecular interactions, specificity, and stability of SANVa9 and SANVb6 with the broadly neutralizing sarbecovirus antibody 5817 and toll-like receptors (TLR2, TLR3, and TLR7) were analyzed using molecular docking and simulation over a 100-nanosecond time scale. Finally, the comparative immune simulation profiles of SANVa9 and SANVb6 with controls indicated stronger, broad-spectrum immune responses that could be translated into in vitro and in vivo studies and warrant further evaluation before clinical use.

Keywords: SARS-CoV-2; COVID-19; HLA; self-assembly; nano vaccine

Check for updates

Academic Editor: Christopher Robinson

Received: 23 April 2026
Revised: 5 June 2026
Accepted: 14 June 2026
Published: 25 June 2026

Copyright: © 2026 by the authors. Licensee MDPI, Basel, Switzerland. This article is an open access article distributed under the terms and conditions of the Creative Commons Attribution (CC BY) license.

1. Introduction

The SARS-CoV-2 virus, the etiological agent of the novel coronavirus disease (COVID-19), was first identified in December 2019 in Wuhan, Hubei Province, China [1,2]. As of 2025, there have been 779,060,919 confirmed COVID-19 cases and 7,108,587 reported deaths globally (WHO COVID-19 Dashboard). The SARS-CoV-2 genome (NC_045512.2) has a total of 11 genes with open reading frames (ORFs): 1ab, 2, 3a, 4, 5, 6, 7a, 7b, 8, 9, and 10. A polyprotein consisting of 16 nonstructural (NS) proteins (NS1–NS16) is encoded by the first gene (ORF1ab) [3,4]. Additionally, the genome encodes accessory proteins via the ORFs 3a, 6, 7a, 7b, and 8. At present, pharmacological treatment options for COVID-19 are mostly limited to repurposed drugs or plant-derived extracts/bioactive compounds that relieve symptoms [5–9], including a few novel drugs designed specifically for SARS-CoV-2.

Therefore, extensive global research efforts have been directed toward developing safer, more effective vaccines using various technological platforms, including inactivated viruses, viral vectors, protein subunits, and mRNA-based approaches. Among them, mRNA-based vaccines such as BNT162b2 and mRNA-1273 demonstrated approximately 94–95% efficacy towards symptomatic COVID-19 [10,11]. Inactivated virus vaccines, including CoronaVac and BBIBP-CorV, showed a broader efficacy range between 50.7% and 91% [12], while protein subunit vaccines like NVX-CoV2373 achieved a 95.6% efficacy rate against the wild-type SARS-CoV-2 strain [13]. Most vaccines have demonstrated the ability to evade neutralizing antibodies, thereby potentially compromising the efficacy of existing vaccines [14]. The reduced effectiveness of COVID-19 vaccines can be attributed to several factors, including the emergence of new SARS-CoV-2 variants like Alpha (B.1.1.7), Beta (B.1.351), Gamma (P.1), Delta (B.1.617.2), Omicron, etc., with spike (S) protein mutations that reduce the capability of vaccine-induced antibodies to neutralize the virus. Additionally, individual genetic factors, such as human leukocyte antigen (HLA) allele diversity, can influence vaccine response and immune recognition. Furthermore, immunity tends to wane over time, resulting in decreased protection, particularly against mild or asymptomatic infections. Most current vaccines are based on the original SARS-CoV-2 strain's spike protein. However, continuous viral evolution increases the risk that these vaccines may eventually lose their protective efficacy, even with repeated booster doses. Commercial vaccines have shown a steady decline in T cell epitope conservation as SARS-CoV-2 variants have evolved. It highlights the urgent need for a broadly protective genome-derived vaccine capable of eliciting robust immunity against both existing and future variants, referred to as a variant-proof vaccine [15]. To address this concern, it is necessary to focus on designing a genome-derived vaccine and identifying epitopes that can support timely updates to existing vaccine formulations.

The existing vaccine candidates have focused on the virus's structural proteins, including S protein [16], Membrane (M) protein [17], Nucleocapsid (N) protein [18], Envelope (E) protein, or a combination of these antigens [19]. Notably, vaccine formulations that incorporate both structural and non-structural proteins, commonly referred to as cocktail vaccines, are predicted to elicit enhanced immunity compared to those based solely on structural components or a combination [20–24]. In recent years, several studies have focused on computational epitope prediction, conserved antigen targeting, mutational analysis of epitopes, and advanced vaccine engineering approaches, including structure-based protein nanoparticle design to counter the continuously emerging SARS-CoV-2 strains [24,25]. Self-assembling peptide nanoparticles (SAPN), with variable size, shape, and surface characteristics, offer significant advantages for vaccine development, including their ability to enhance antigen presentation and immune responses [24,26].

In general, vaccines targeting multiple conserved epitopes from different antigens can elicit strong cellular immune responses that synergize with B-cell responses, leading to long-term vaccine efficacy [27]. Moreover, the inclusion of epitopes from non-spike proteins in SARS-CoV-2 vaccines may be important for inducing protective T cell memory [28,29]. Therefore, vaccine design strategies targeting evolutionarily constrained epitopes are more promising candidates for broad-spectrum COVID-19 vaccines, providing strong protection against both existing and future coronavirus threats [30,31]. This method holds great potential for developing mutation-resistant or even pan-genome vaccines [32]. In some cases, the reduced efficacy of these vaccines may be attributed to rapid degradation in the extracellular environment, rapid dispersion from the injection site, or poor uptake by antigen-presenting cells (APC) [33,34]. Several studies suggest that conjugating epitope vaccines to carriers such as polymeric or lipid-based nanostructures can help overcome these limitations by improving stability, retention, and cellular uptake [34,35]. Moreover,

a multiepitope-based coiled-coil self-assembling nanostructure vaccine (SANV) design strategy offers several advantages over conventional vaccines, including enhanced immunogenicity, stability, and solubility [36,37]. As per the available literature survey, no COVID-19 universal vaccine has been reported to date that utilizes experimentally known conserved B lymphocyte (BL), Helper T lymphocyte (HTL), and cytotoxic T lymphocyte (CTL) epitopes from non-spike proteins, and that also uses a self-assembling pentameric and trimeric coiled-coil domain as a scaffold for epitope presentation.

The current study explored the design of cocktail SANV constructs without/with (SANVa/SANVb) adjuvant, TAT, and PADRE, integrating conserved B and T cell epitopes resultant from structural (devoid of S), non-structural (replicase polyprotein 1a (RPP1a)), and accessory proteins across the spectrum of SARS-CoV-2 variants, with the goal of eliciting broad-spectrum neutralizing antibodies as well as strong cell-mediated immune responses. Comprehensive in silico analyses were conducted to evaluate epitope conservation, global population coverage, cytokine-induction potential, and T-cell receptor (TCR) cross-reactivity of the screened epitopes. The designed coiled-coil SANV constructs were subsequently assessed for their physicochemical traits, allergenicity, solubility, antigenicity, and antioxidant potential. Finally, the interaction of selected SANV constructs with the broad sarbecovirus-neutralizing antibody (5817) and TLR-2, -3, and -7, along with experimentally validated binding ligands (positive controls), was analyzed using molecular docking and simulation. Moreover, immune simulations and in silico cloning experiments were carried out to assess the safety and immunogenicity profile, as well as the expression ability of the most potent SANVb/SANVa construct in *E. coli*.

2. Materials and Methods

2.1. Retrieval of SARS-CoV-2 Epitopes and Their Source Proteins

The identification of epitopes was carried out using data available in the Immune Epitope Database (IEDB v3.10.0) (https://www.iedb.org; accessed on 22 March 2023) by applying particular selection criteria, including epitope type (linear peptides), source organism (SARS-CoV-2; ID: 2697049), host (human), assay type (B-cell or T-cell assays with positive outcomes), MHC restriction (any), and disease category (any)). A total of 10 target proteins were considered, comprising three structural proteins (N, M, and E), one non-structural protein (RPP1a), and six accessory proteins (ORF3a, ORF6, ORF7a, ORF7b, ORF8, and ORF10). The extracted epitopes were divided into three categories: BL epitopes, HTL epitopes restricted with HLA class II alleles, and CTL epitopes associated with HLA class I alleles. Only epitopes with four-digit HLA allele nomenclature were retained; excluded formats included HLA class II, including H2-Db, H2-Kb, HLA-A2, HLA-DR, HLA-DRA01:01/DRB104:01, and HLA-DP (Figure 1). The NCBI Virus Database (https://www.ncbi.nlm.nih.gov/labs/virus/vssi/#/, accessed on 13 June 2026) was then used to obtain the corresponding amino acid sequences of the source proteins across several SARS-CoV-2 variants (Table 1).

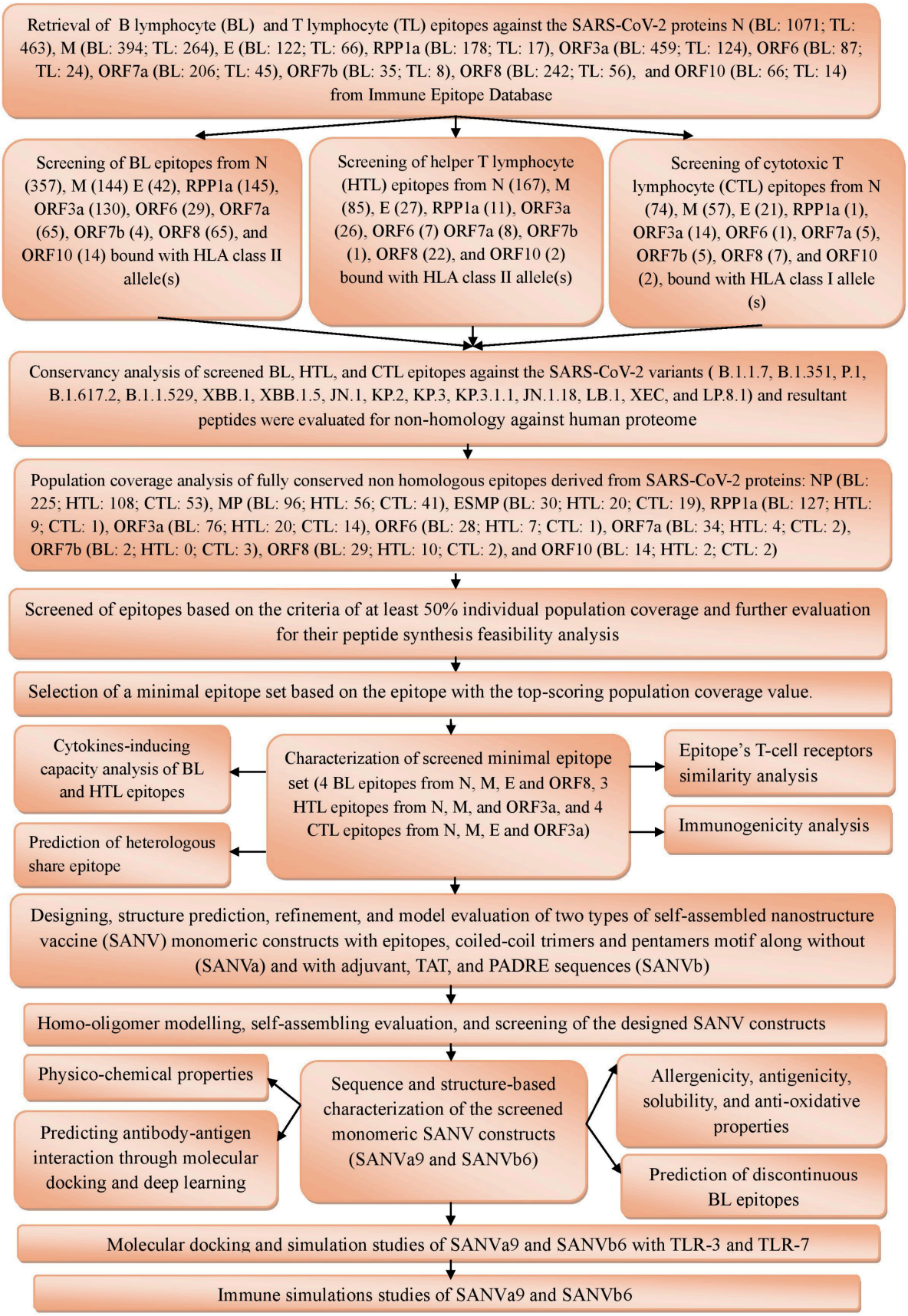


Figure 1. The workflow outlines the computational pipeline employed for the design and evaluation of cocktail self-assembling nanostructure vaccine (SANV) constructs against SARS-CoV-2. N—Nucleocapsid protein, M—Membrane protein, E—Envelope small membrane protein, RPP1a—Replicase polyprotein1a, ORF—Open reading frame.

Table 1. Details of SARS-CoV-2 proteins along with their accession numbers across variants.

Protein	B.1.1.7	B.1.351	B.1.617.2	P.1	B.1.1.529	JN.1	XBB.1	XBB.1.5	KP.2	KP.3	KP.3.1.1	JN.1.18	LB.1	XEC	LP.8.1
N	WWQ76901.1	WVH48565.1	WWZ28265.1	WWQ50657.1	WVR50305.1	WWZ86293.1	BDE46852.1	WWZ84749.1	XOL11111.1	XOL57736.1	XOL32195.1	XHV18295.1	XOL61088.1	XOL32065.1	XOL32255.1
M	XNJ16174.1	XPO66386.1	XNJ24964.1	XNJ20829.1	XOX23704.1	XOP74628.1	XNL94515.1	BDE46847.1	XNO66846.1	XOL57731.1	XOL32191.1	XLV33858.1	XOL61107.1	XOT63748.1	XOT63630.1
E	ULQ63199.1	UFQ05200.1	UEA15882.1	XNJ21388.1	XLU40735.1	XOP75889.1	XNL95530.1	XNL92260.1	XNO66845.1	XOL57730.1	XOL32190.1	XLV33857.1	XOL61106.1	XOT63747.1	XOT63629.1
RPP1a	XNJ22325.1	XND52779.1	XQJ39130.1	XNJ20978.1	XKD21092.1	XOL58764.1	XNL93172.1	XNL92015.1	XNO66842.1	XOL57727.1	XOL32282.1	XLO33783.1	XQT59775.1	XQT65412.1	XQP13616.1
ORF3a	UFQ05187.1	QWW93437.1	XNC83392.1	XNJ20980.1	XOX23702.1	XPK52095.1	XNL95529.1	XNL92259.1	XPQ60993.1	XOL57729.1	XOL32189.1	XLV33856.1	XOL61105.1	XOT63746.1	XOT63628.1
ORF6	UFQ05190.1	UFQ05202.1	UEA15884.1	XNC81955.1	XOX23705.1	XOL58769.1	XIT91752.1	XNL93010.1	XNO66847.1	XOL57732.1	XOL32192.1	XLV33859.1	XOL61108.1	XOT63749.1	XOT63631.1
ORF7a	XNJ16614.1	XPO66436.1	XNC85376.1	XNJ22859.1	XOX23884.1	XOL58770.1	XIT91585.1	XNL93000.1	XNO66848.1	XOL57733.1	XOL32193.1	XLV33860.1	XOL61109.1	XOT63750.1	XOT63738.1
ORF7b	UFQ05192.1	UFQ05204.1	UEA15886.1	XNJ22944.1	XOX23981.1	XOL58771.1	XKT60046.1	XNL92632.1	XNO66849.1	XOL57734.1	XOL32194.1	XLV33861.1	XOL61110.1	XOT63751.1	XOT63739.1
ORF8	UPE78472.1	XND03925.1	XND99302.1	XDF47973.1	WDD75399.1	XJO57807.1	WGO03549.1	WGH15690.1	XJJ54324.1	XKT95006.1	XPQ61628.1	XAN95851.1	XJW02963.1	XQH91555.1	XQK96978.1
ORF10	UFQ05195.1	UFQ05206.1	UEA15888.1	XNJ23652.1	XOX24319.1	XOL58774.1	XIT90504.1	XNL92904.1	XNO66805.1	XOL57737.1	XOL32196.1	XLV33864.1	XOL61113.1	XOT63706.1	XOT63612.1

2.2. Screening of Minimal Epitope Set Based on Conservancy, Non-Homology, Population Coverage, and Peptide Synthesis Feasibility

2.2.1. Screening of Fully Conserved Epitopes

The IEDB Conservancy Analysis Tool (v3.0.2) (http://tools.iedb.org/conservancy/, accessed on 13 June 2026) was used to evaluate epitope conservation within the respective source proteins of SARS-CoV-2 variants, as shown in Table 1, using default parameters.

2.2.2. Non-Homology Analysis

The PepMatch tool (v0.1.0) (https://nextgen-tools.iedb.org/pipeline?tool=pepmatch, accessed on 13 June 2026) was used to evaluate the fully conserved epitopes for non-homology. The prediction settings were adjusted to allow zero mismatches, thereby eliminating peptides with potential cross-reactivity to human proteins.

2.2.3. Analysis of Population Coverage

The worldwide population coverage of non-homologous, fully conserved individual BL, HTL, and CTL epitopes was assessed using the IEDB Population Coverage Analysis Tool (3.0.2) (https://tools.iedb.org/population/, accessed on 13 June 2026) with the default parameters.

2.2.4. Peptide Synthesis Analysis

The synthetic feasibility analysis of the resulting BL, HTL, and CTL epitope sets, screened for at least 50% individual population coverage and availability of CDR3 sequences, was performed using the PepSySco tool (v2.27) (http://tools.iedb.org/pepsysco/, accessed on 13 June 2026).

2.2.5. Minimal Epitope Set Selection

The minimal epitope set of BL, HTL, and CTL epitopes was selected based on the top-scoring population coverage value for the source antigen. When multiple epitopes from the source antigen exhibited the same population coverage value, preference was given to those with a higher number of available CDR3 sequences. When CDR3 sequences were unavailable, the epitope with the highest synthesis score was selected.

2.3. In Silico Functional Characterization of the Screened Minimal Epitope Set

2.3.1. Analysis of Combined Population Coverage

The screened minimal epitope set was evaluated for Class I and II combined population coverage using the IEDB web server (v3.0.2) (https://tools.iedb.org/population/, accessed on 13 June 2026) against the world population.

2.3.2. Analysis of Cytokine-Inducing Potential

The IFNepitope Tool (http://crdd.osdd.net/raghava/ifnepitope/, accessed on 13 June 2026) was employed to assess the ability of selected B-cell and T-cell epitopes to stimulate interferon-gamma (IFN-γ) responses. The IL10pred Tool (https://webs.iiitd.edu.in/raghava/il10pred/, accessed on 13 June 2026) was further utilized to assess the IL-10-induced potential of these epitopes, applying a threshold value of -0.3) [38,39]. Similarly, IL-4 induction was predicted using the IL4pred Tool (https://webs.iiitd.edu.in/raghava/il4pred/, accessed on 13 June 2026) utilizing a threshold of 0.2. In addition, antibody class-specific B-cell epitopes were identified with the IgPred Tool (https://webs.iiitd.edu.in/raghava/igpred/pep-fix-pred.html, accessed on 13 June 2026). Designed with a user-friendly interface, the server facilitates the identification of epitopes that induce specific antibody classes, namely IgG, IgE, and IgA. Predictions were performed at a threshold of 0.9.

2.3.3. Immunogenicity Analysis

The Class I Immunogenicity prediction tool (v3.0) on the IEDB website (http://tools.iedb.org/immunogenicity, accessed on 13 June 2026) with default parameters was used to assess the immunogenic potential of the selected CTL epitopes. Similarly, the CD4 T Cell Immunogenicity prediction tool from IEDB (v0.1.0) (http://tools.iedb.org/CD4episcore/, accessed on 13 June 2026), likewise using default parameters, was used to evaluate the immunogenicity of HTL and B-cell epitopes. Furthermore, the DeepImmuno tool (https://deepimmuno.research.cchmc.org, accessed on 13 June 2026) was subsequently used to examine the immunogenicity of CD8+ T-cell epitopes, considering peptide MHC interactions and focusing on prevalent HLA alleles, independent of conventional predictions of MHC–peptide binding affinity.

2.3.4. Prediction of Heterologous Shared Epitopes

To identify common heterologous epitopes within the screened minimal epitope set across various pathogens, the Peptide Search tool on the UniProt platform (https://www.uniprot.org/peptide-search, accessed on 13 June 2026) was used with default parameters. Additionally, MAIT Match 1.0 (http://www.cbs.dtu.dk/services/MAIT_Match, accessed on 13 June 2026) and TCRmatch (http://tools.iedb.org/tcrmatch/, accessed on 13 June 2026) were used at default settings to analyze the similarity of epitope-associated CDR3 sequences from the T-cell receptor beta (TCRβ) chain, utilizing data information available in the IEDB.

2.4. Designing Monomeric Vaccine Constructs with Self-Assembling Coiled Coil Motifs

There are 2 distinct SANV constructs, designated SANVa and SANVb (Figure 2), that were developed by incorporating a pentameric and a trimeric self-assembling coiled-coil domain, in addition to a minimal epitope set comprising BL, HTL, and CTL epitopes. These constructs also included the PADRE peptide (as a universal pan-HLA-DR-binding epitope), human β-defensin-3 (as an adjuvant), and the TAT peptide, all of which were connected using appropriate linkers. By utilizing 12 distinct pentameric and trimeric self-assembling coiled-coil motif sequences combination described in earlier studies (SAPN-K [40], LFC4 [41], NP-L/C [42], P6c [43], P6HRC1 [44], P4c-Mal SAPN [45], Mono-M2e [46], PfCSP-KMY SAPN [47], MPER-SAPN [48], GRA7$_{(20–28)}$ SAPN [49], SAPN-Combo [50] and PfCSP-SAPN [47]) a total of 24 SANV constructs were generated including 12 constructs with adjuvant, TAT, and PADRE sequences, and 12 constructs without them.

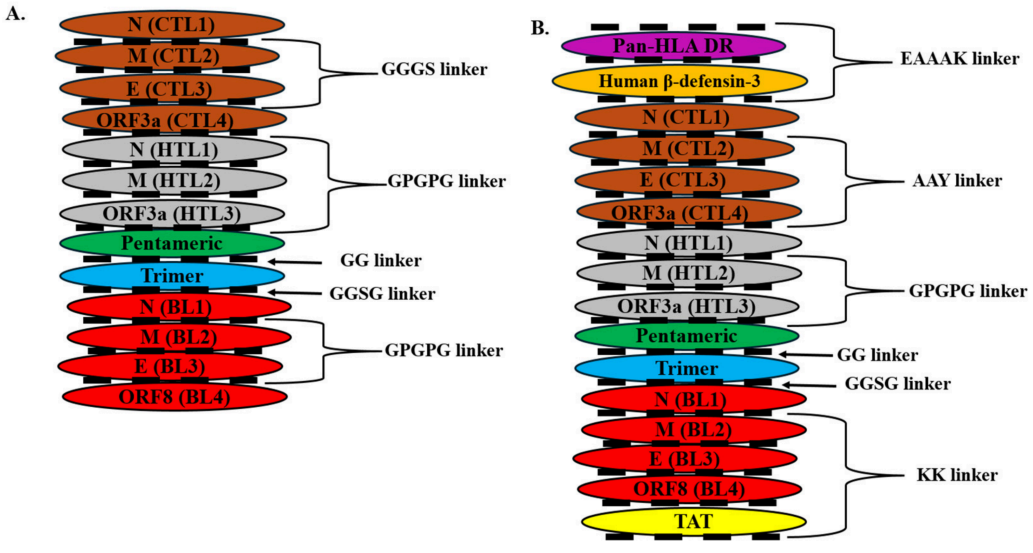


Figure 2. Schematic illustration of two types of self-assembling peptide vaccine constructs (SANVa and SANVb). (**A**) In the SANVa construct, linkers are represented in black. CTL epitopes from the

N, M, E, and ORF3a proteins (CTL1-CTL4) (shown in brown) are connected using GGGS linkers. The pentameric motifs (shown in green) and the trimeric motifs (depicted in sky blue) are connected through glycine–glycine (GG) linkers. BL epitopes from the N, M, E, and ORF8 proteins (BL1-BL4) (red) are linked using GPGPG linkers. An HTL epitope (gray colour), derived from the N, M, and ORF3a proteins (HTL1-HTL3) and placed among the pentameric and the CTL epitopes, is joined via a GPGPG spacer, as reported by Babapoor et al. [46] and Kaba et al. [47]. (**B**) In the SANVb construct, black color represents the linkers. CTL epitopes from the N, M, E, and ORF3a proteins (CTL1-CTL4) (brown) are connected using AAY linkers. The pentameric (green) and trimeric (sky blue) domains are connected using GG linkers. B-cell (BL) epitopes from the N, M, E, and ORF8 proteins (BL1–BL4; red) are fused through KK linkers. An HTL epitope (gray colour), derived from the N, M, and ORF3a proteins (HTL1–HTL3) and situated within the pentameric domain and the CTL epitopes, is joined via a GPGPG linker. In addition, human β-defensin-3 (shown in orange), along with pan-HLA DR-binding epitopes (PADRE, depicted in pink), is introduced at the N-terminus using EAAAK linkers, while a TAT sequence (shown in blue) is added to the C-terminus through a KK linker, following the approach of Dong et al. [21] and Yu et al. [51].

2.5. Tertiary Structure Modeling, Refinement, and Validation of the Monomeric SANV Construct

The three-dimensional structures of 24 self-assembling monomeric vaccine constructs (SANVa1–12 and SANVb1–12) were generated using GalaxyTBM (http://galaxy.seoklab.org/, accessed on 13 June 2026) and AlphaFold3 through default parameters. The resulting 3D models were subsequently refined using the GalaxyRefine server (https://galaxy.seoklab.org/cgi-bin/submit.cgi?type=REFINE, accessed on 13 June 2026), which improves structural quality through relaxation, loop optimization, and molecular dynamics–based refinement [52,53]. The structural quality of the refined models was estimated using validation tools such as ERRAT and PROCHECK, available through the SAVES v6.1 server (https://saves.mbi.ucla.edu/, accessed on 13 June 2026). Furthermore, the ProSA-web server (https://prosa.services.came.sbg.ac.at/prosa.php, accessed on 13 June 2026) was employed to calculate the z-score, which measures the deviation of the model's atomic structure from those of proteins verified experimentally [54].

2.6. Homo-Oligomer Modeling for Designed SANV Monomeric Constructs

Prediction of homo-oligomeric forms for each monomeric SANV construct (SANVa1–12 and SANVb1–12) was carried out using the GalaxyHomomer tool (https://galaxy.seoklab.org/cgi-bin/submit.cgi?type=HOMOMER, accessed on 13 June 2026) and AlphaFold3 (https://alphafoldserver.com/, accessed on 13 June 2026) under default settings, with the oligomeric state set to 12 in GalaxyHomomer. Homo-oligomers are multimeric assemblies formed through interactions among identical protein subunits [55]. For each construct type, the top-ranked GalaxyHomomer model was selected based on the largest interface area. The best-scoring model was subsequently used to predict homo-multimeric structures using AlphaFold-Multimer (https://deepmind.google/technologies/alphafold/alphafold-server/, accessed on 13 June 2026), which enables the modeling of both homo- and hetero-multimeric protein complexes. For homo-multimer prediction, the number of identical chains was adjusted according to the tool's upper limit of 50,000 amino acids per sequence. Previously reported vaccine constructs, MPER-SAPN (C1) [48] and P4c-Mal SAPN (C2) [45], were included as positive controls to validate the highest-scoring performing SANV models. The His-tag was removed from the amino acid sequences of these control constructs before analysis.

2.7. Characterization of the Screened SANV Constructs Modeled by Homo-Oligomer Modeling

2.7.1. Physicochemical Properties Prediction of the SANV Construct

Physicochemical profiling of the selected SANV constructs was performed via the ProtParam tool available on the ExPASy platform (https://web.expasy.org/protparam/,

accessed on 13 June 2026). considering key parameters including molecular weight (MW), aliphatic index (AI), grand average of hydropathicity (GRAVY) score, isoelectric point (pI), predicted half-life, and instability index (II).

2.7.2. Antigenicity, Allergenicity, Solubility, and Antioxidant Characteristics Prediction of the SANV Construct

To ensure that the selected SANV constructs are non-allergenic, highly antigenic, soluble, and possess antioxidant properties, several computational tools with default parameters were used to characterize them. Allergenicity was assessed using AllerTOP v1.1 (https://www.ddg-pharmfac.net/allertop/, accessed on 13 June 2026) and AllergenFP v1.1 (https://ddg-pharmfac.net/AllergenFP/, accessed on 13 June 2026). Antigenicity was predicted through ANTIGENpro (https://scratch.proteomics.ics.uci.edu/, accessed on 13 June 2026) and VaxiJen v2.0 (http://www.ddg-pharmfac.net/vaxijen, accessed on 13 June 2026). Solubility of the constructs was assessed using SOLpro (http://scratch.proteomics.ics.uci.edu/, accessed on 13 June 2026) and Protein-Sol (https://protein-sol.manchester.ac.uk/, accessed on 13 June 2026), as well as additional predictive tools. The AnOxPePred v1.0 web server (http://services.bioinformatics.dtu.dk/service.php?AnOxPePred-1.0, accessed on 13 June 2026), which uses a convolutional neural network to predict the free radical-scavenging capacity of peptides, was used to assess antioxidant potential. Additionally, SignalP v4.1 (http://www.cbs.dtu.dk/services/SignalP-4.1/, accessed on 13 June 2026) and TMHMM v2.0 (https://services.healthtech.dtu.dk/service.php?TMHMM-2.0, accessed on 13 June 2026) were used to predict transmembrane helices and signal peptides, respectively. Additionally, the Evolutionary Scale Modeling inverse folding (ESM-IF) generative framework was used to assess absolute protein folding stability (ΔG), implemented using the freely accessible Colab notebook suggested by Cagiada et al. [56].

2.7.3. Discontinuous BL Epitope Prediction for SANV Constructs

The DiscoTope v2.0 web server (http://www.cbs.dtu.dk/services/DiscoTope/, accessed on 13 June 2026) was used to anticipate discontinuous B-cell epitopes within the 3D structures of the selected SANV constructs along with N protein (PDB ID: 7SUE), M protein (PDB ID: 7VGR), E protein (PDB ID: 7M4R), and ORF8 protein (PDB ID: 7MX9), using the default threshold of −3.7 as advised by Kringelum et al. [57].

2.7.4. Computational Prediction of Antibody–Antigen Binding Using Docking and Deep Learning Methods

The 3D structures of the selected SANV constructs were docked by the broad sarbecovirus neutralizing antibody 5817 (PDB ID: 8KHD) by utilizing the ClusPro v2.0 server, applying the "Advanced Options" through "Antibody Mode" enabled and the setting to "Automatically Mask non-CDR regions." To serve as a positive control (C3), the experimentally validated ligand of antibody 5817, the Omicron RBD protein (PDB ID: 98KHD), was used as reported by Wang et al. [58], facilitating comparative analysis of the docking results. Moreover, for antibody–antigen (Ab–Ag) docking prediction using AlphaFold 3 (https://alphafoldserver.com/, accessed on 13 June 2026), the amino acid sequences of the antibody heavy chain, light chain, and the target antigen were first prepared in FASTA format. These sequences were then submitted to AlphaFold 3, enabling direct prediction of the antibody–antigen complex rather than modeling each component independently. The interaction residues within the docked complexes were discovered using the PDBSum web server (http://www.ebi.ac.uk/thornton-srv/databases/pdbsum/, accessed on 13 June 2026). The antigen–antibody binding affinity was further evaluated utilizing the AREA-AFFINITY web server (https://affinity.cuhk.edu.cn/, accessed on 13 June 2026) with default parameter, employing the docked complex PDB structure as input. The antibody

was specified as binding partner 1, and the antigen as binding partner 2, in accordance with the guidelines provided by Yang et al. [59]. Additionally, to assess binding interactions of the selected SANV constructs (antigen) with various SARS-CoV-2 neutralizing antibodies (antibody), including broad sarbecovirus neutralizing antibody 5817 (PDB ID: 8KHD), broadly neutralizing human monoclonal antibody (bNAb) K501SP6 (PDB ID: 9FJK) [60] and other neutralizing antibodies (nAbs) such as K501SP6 (PDB ID: 9FJK), S309 (PDB ID: 7TLY), LY-CoV555 (PDB ID: 7KMG), CB6 (PDB ID: 7C01), 76E1 (PDB ID: 7X9E), CR3022 (PDB ID: 7JN5), 5–7 (PDB ID: 7RW2), and S2P6 (PDB ID: 7RNJ), as reported by Chen et al. [61], the AbAgIntPre web server (http://www.zzdlab.com/AbAgIntPre, accessed on 13 June 2026) was used to predict antibody-antigen interaction scores, employing the specific SARS-CoV model under default conditions [62].

2.8. SANV Constructions with TLR2, TLR3, and TLR7: Molecular Docking and Simulated Analysis

To investigate the interactions within selected SANV constructs (as ligands) and the TLR-2, TLR-3, and TLR-7 (receptors), protein–protein interaction studies were conducted using the web servers ClusPro v2.0 (https://cluspro.org/help.php, accessed on 13 June 2026) and AlphaFold 3 (https://alphafoldserver.com/, accessed on 13 June 2026) with default parameters. Experimentally validated ligands of TLR-2, TLR-3, and TLR-4, namely, the Staphylococcal Superantigen-Like protein 3 (PDB ID: 5D3I), UNC93B1 (PDB IDs: 7C76 and 7CYN), served as positive controls (designated as C4, C5, and C6, respectively). Prior to docking, all water molecules and non-essential components were removed from the receptor and ligand PDB files using AutoDock Tools version 1.5.7. The binding free energy (ΔG) of each molecular complex was estimated utilizing the PRODIGY web server (https://wenmr.science.uu.nl/prodigy/, accessed on 13 June 2026), while PDBSum (http://www.ebi.ac.uk/thornton-srv/databases/pdbsum/, accessed on 13 June 2026) was used to identify interaction residues within the complexes.

Additionally, molecular dynamics (MD) simulations were conducted on the best-docked SANV constructs with TLR, compared with the control, using the GROMACS program with the CHARMM 27 force field to explore temporal stability and interaction dynamics of the protein complexes. In which the protein was placed in a 90 Å cubic simulation box and solvated with the SPCE water model to replicate a realistic biological environment. Energy minimization was performed using the steepest descent algorithm to remove steric clashes and stabilize the system. The equilibration phase was divided into two key steps. First, a 10-nanosecond temperature equilibration was carried out under the NVT ensemble using v-rescale temperature coupling, maintaining the system at 300 K and applying positional restraints to stabilize solvent orientation. This was followed by a 10-nanosecond pressure equilibration under the NPT ensemble at 1 bar, during which restraints were gradually released to allow the system to adapt to the pressure conditions while preserving its overall structural integrity. A 100-nanoseconds production simulation was then performed under constant temperature and pressure conditions to observe natural molecular behavior and protein interactions. Throughout this phase, critical dynamic parameters, including root mean square deviation (RMSD), root mean square fluctuation (RMSF), radius of gyration (Rg), solvent-accessible surface area (SASA), and hydrogen bonding (H-bond) patterns, were systematically analysed.

2.9. In Silico Immune Simulation of Selected Monomeric SANV Constructs

The C-ImmSim web server (https://kraken.iac.rm.cnr.it/C-IMMSIM/index.php, accessed on 13 June 2026) was used to simulate immune responses to the chosen monomeric SANV constructs (SANVa9 and SANVb6). Positive controls included a recombinant SARS-CoV-2 multivalent epitope vaccine (rSMEV) (C7) created by Yu et al. [51] and a clinically

trialed (Phase I/II) subunit vaccine, UB-612/C8, reported by Wang et al. [63] to provide a more real-world benchmark involving the following high-frequency allele of the host's HLA heterozygous combination HLA-A (A*0201, A*2402), HLA-B (B*0702, B*0801), and HLA-DR (DRB1_1501, DRB1_0701). The injection protocol included three doses administered at once every four-week intervals, corresponding to simulation time steps of 1, 84, and 168 (with each time step representing 8 h), and the total simulation step was set to 1050 steps, following previously reported studies [64,65]. The default condition was set to a random seed of 12,345, a simulation volume of 10, an adjuvant level of 100, and 1000 antigen injections.

2.10. In Silico Cloning Optimization of Selected Monomeric SANV Constructs

Using the Java Codon Adaptation Tool (JCat) (http://www.jcat.de, accessed on 13 June 2026), the protein sequences of SANVa9 and SANVb6 were back-translated into nucleotide sequences and subsequently optimized for codon usage. The codon optimization was performed to improve gene expression efficiency in the *E. coli* (K-12 strain) host system. Throughout this process, sequence elements such as rho-independent transcription terminators, prokaryotic ribosome-binding sites, and restriction enzyme recognition sites were carefully avoided [66]. The codon-optimized nucleotide sequences of SANVa9 and SANVb6, including stop codons, were cloned into the pET-28a (+) vector utilizing SnapGene v8.2 software (https://snapgene.com/, accessed on 13 June 2026). Prior to cloning, the DNA sequences of SANVa9 and SANVb6 were screened to ensure the absence of restriction enzyme recognition sites intended for cloning. After verification, appropriate restriction enzyme sites were introduced at the N- and C-termini of the constructs to facilitate efficient insertion into the vector [67].

3. Results

3.1. IEDB-Based Screening of Cross-Reactive BL, HTL, and CTL Epitopes Across the SARS-CoV-2 Proteins, Excluding the Spike Protein

Neutralizing antibody titers are crucial markers of immune defense towards SARS-CoV-2 and are commonly used to evaluate vaccine efficacy. However, protective immunity also involves multiple components activated during infection or vaccination. In this research, we evaluated promising epitopes for vaccine design by analyzing experimentally known epitopes from various SARS-CoV-2 proteins (N, M, E, RPP1a, and accessory proteins ORF3a, ORF6, ORF7a, ORF7b, ORF8, and ORF10), excluding the spike and ORF1ab proteins. The details of the epitope screening results are presented in the respective table found in Supplementary File S1. The total number of identified linear BL and T-lymphocyte (TL) epitopes were as follows: N (BL: 1071; T: 463) (Tables S1 and S2), M (BL: 394; T: 264) (Tables S6 and S7), E (BL: 122; T: 66) (Tables S11 and S12), RPP1a (BL: 178; T: 17) (Tables S16 and S17), ORF3a (BL: 459; T: 124) (Tables S21 and S22), ORF6 (BL: 87; T: 24) (Tables S26 and S27), ORF7a (BL: 206; T: 45) (Tables S31 and S32), ORF7b (BL: 35; T: 8) (Tables S36 and S37), ORF8 (BL: 242; T: 56) (Tables S41 and S42), and ORF10 (BL: 66; T: 14) (Tables S46 and S47). From these, screened BL epitopes capable of binding to HLA class II alleles were as follows: N (357) (Table S3), M (144) (Table S8), E (42) (Table S13), RPP1a (145) (Table S18), ORF3a (130) (Table S23), ORF6 (29) (Table S28), ORF7a (65) (Table S33), ORF7b (4) (Table S38), ORF8 (65) (Table S43), and ORF10 (14) (Table S48), as provided in Supplementary File S1. However, HTL epitopes binding to HLA class II alleles were identified as follows: N (167) (Table S4), M (85) (Table S9), E (27) (Table S14), RPP1a (11) (Table S19), ORF3a (26) (Table S24), ORF6 (7) (Table S29), ORF7a (8) (Table S34), ORF7b (1) (Table S39), ORF8 (22) (Table S44), and ORF10 (2) (Table S49), as detailed in Supplementary File S1. Additionally, CTL epitopes binding

to HLA class I alleles were screened as follows: N (74) (Table S5), M (57) (Table S10), E (21) (Table S15), RPP1a (1) (Table S20), ORF3a (14) (Table S25), ORF6 (1) (Table S30), ORF7a (5) (Table S35), ORF7b (5) (Table S40), ORF8 (7) (Table S45), and ORF10 (2) (Table S50), as given in Supplementary File S1. Among the analyzed proteins, several shared BL and HTL epitopes, indicating potential cross-reactivity. The numbers of such identified epitopes shown in Supplementary File S1 were as follows: N (162; Tables S3 and S4), M (60; Tables S8 and S9), E (19; Tables S13 and S14), RPP1a (10; Tables S18 and S19), ORF3a (14; Tables S23 and S24), ORF6 (7; Tables S28 and S29), ORF7a (6; Tables S33 and S34), ORF8 (21; Tables S43 and S44), and ORF10 (1; Tables S48 and S49). For the N protein, two epitopes were found to be common between BL and CTL (Supplementary File S1; Tables S3 and S5). Moreover, in the M protein, three BL epitopes were identified that bind to HLA class I alleles (Supplementary File S1; Table S8). While one epitope was found common to both BL and CTL along with HLA class I alleles' binding profile (Supplementary File S1; Tables S8 and S10), another was identified in 1 BL epitopes with binding affinities for both HLA class I and II alleles (Supplementary File S1; Table S8). Additionally, one epitope was common between HTL and CTL epitopes and demonstrated binding affinity to both HLA class I and II alleles (Supplementary File S1; Tables S8 and S10). More importantly, one epitope was shared among BL, HTL, and CTL and showed binding potential with both HLA class I and class II alleles, suggesting strong cross-reactivity (Supplementary File S1; Tables S8–S10). For the E protein, only one BL epitope was found with HLA class I and class II allele binding (Supplementary File S1; Table S13). This in-depth screening highlights promising candidates for the development of a subunit vaccine along with enhanced specificity and immunological significance.

3.2. Screening of Minimal Epitope Set

3.2.1. Analysis of Fully Conserved Epitopes

The IEDB-based epitope conservancy analysis tool evaluates the degree of conservation and calculates the proportion of protein sequences that correspond to each epitope at various sequence identity levels. This examination of the conservation of screened aforementioned BL, HTL, and CTL epitopes within the N, M, E, RPP1a, ORF3a, ORF6, ORF7a, ORF7b, ORF8, and ORF10 protein sequences against the various SARS-CoV-2 variants (B.1.1.7, B.1.351, P.1, B.1.617.2, B.1.1.529, XBB.1, XBB.1.5, JN.1, KP.2, KP.3, KP.3.1.1, JN.1.18, LB.1, XEC, and LP.8.1) revealed varying levels of conservancy ranging from 0% to 100% The details of the epitopes conservancy screening results are shown in respective Tables of Supplementary File S2. Among the analysed proteins, 100% epitope conservancy were observed for the N (BL: 225; HTL: 108; CTL: 53) (Tables S1–S3), M (BL: 96; HTL: 56; CTL: 41) (Tables S4–S6), E (BL: 30; HTL: 20; CTL: 19) (Tables S7–S9), RPP 1a (BL: 127; HTL: 9; CTL: 1) (Tables S10–S12), ORF3a (BL: 76; HTL: 20; CTL: 14) (Tables S13–S15), ORF6 (BL: 28; HTL: 7; CTL: 1) (Tables S16–S18), ORF7a (BL: 34; HTL: 4; CTL: 2) (Tables S19–S21), ORF7b (BL: 2; HTL: 0; CTL: 3) (Tables S22–S24), ORF8 (BL: 29; HTL: 10; CTL: 2) (Tables S25–S27), and ORF10 (BL: 14; HTL: 2; CTL: 2) (Tables S28–S30).

3.2.2. Analysis of Non-Homology

None of the selected fully conserved BL, HTL, and CTL epitopes derived from the N, M, E, RPP1a ORF3a, ORF6, ORF7a, ORF7b, ORF8, and ORF10 shared sequence identity in contrast to the reference proteome of humans. This finding supports the safety of the selected epitopes for potential inclusion in the development of the SARS-CoV-2 vaccine, minimizing the probability of autoimmune responses [68].

3.2.3. Analysis of Population Coverage

Successful vaccine development requires a thorough understanding of epitope-binding profiles across HLA alleles and their associated population coverage [69,70]. Accordingly, population coverage assessment of the fully conserved BL, HTL, and CTL epitopes derived from the N, M, E, RPP1a, ORF3a, ORF6, ORF7a, ORF7b, ORF8, and ORF10 revealed considerable variation across proteins. The population coverage of epitopes ranged from 0% to 94% and is shown in the respective Tables of Supplementary File S3. The observed % population coverage for epitopes ranged from 0 to 94 (shown in Supplementary File S3). The details are as follows: N (BL: 0–88.05%; HTL: 0–88.05%; CTL: 0–94.70%) (Tables S1–S3), M (BL: 0–87.17% for class II; BL: 16.84–75.16% for class I; HTL: 0–87.17%; CTL: 0–77.68%) (Tables S4–S7), E (BL: 0–87.17%; HTL: 0–87.17%; CTL: 0–51.01%) (Tables S8–S10), RPP1a (BL: 4.74–55.61%; HTL: 9.75–55.61%; CTL: 1.20–12.78%) (Tables S11–S13), ORF3a (BL: 9.75–55.61%; HTL: 0–83.81%; CTL: 0–64.14%) (Tables S14–S16), ORF6 (BL: 9.75–38.62%; HTL: 9.75–38.62%; CTL: 15.83–43.68%) (Tables S17–S19), ORF7a (BL: 9.75–55.61%; HTL: 0–55.61%; CTL: 0–30.32%) (Tables S20–S22), ORF7b (BL: 9.75–38.62%; CTL: 3.37–43.68%) (Tables S23 and S24), ORF8 (BL: 0–83.81%; HTL: 0–83.81%; CTL: 3.37–39.08%) (Tables S25–S27), and ORF10 (BL: 9.75–38.62%; HTL: 9.75–38.62%; CTL: 3.37–39.08%) (Tables S28–S30), as presented in Supplementary File S3. This epitope set was further screened based on a minimum 50% population coverage value, along with available CDR3 sequences, for feasibility analysis of peptide synthesis.

3.2.4. Analysis of Peptide Synthesis Feasibility

The peptide synthetic feasibility prediction of the aforementioned BL, HTL, and CTL epitopes exhibited synthesis scores ranging from 0.67659 to 0.99998. The PepSySco tool predicts the possibility of a successful peptide synthesis based on amino acid composition and sequence characteristics [71]. Higher values in the scoring system range from 0 to 1, indicating a higher probability of synthetic success.

3.2.5. Selection of Minimal Epitope Set

The final minimal epitope set comprising 4 BL epitopes from N, M, E, and ORF8, 3 HTL epitopes from N, M, and ORF3a protein, and 4 CTL epitopes from N, M, E, and ORF3a protein was selected from various SARS-CoV-2 proteins based on top-scoring individual epitope population coverage (minimum 50%) for each protein. In cases where multiple epitopes from the same protein exhibited the same % population coverage, preference was given to the epitope associated with the highest number of available CDR3 sequences. If no CDR3 sequences were available, selection was based on the highest peptide-synthesis feasibility score (Table 2). Moreover, an additional literature survey revealed that several epitopes, such as BL1, BL2, BL4, HTL1, HTL2, and HTL3, are common to the epitopes analyzed by Dos Santos Alves et al. [72] in their in vivo studies against human coronavirus OC43 (common cold)-elicited CD4+ T cell responses that cross-react with SARS-CoV-2.

Table 2. Details of the screened minimal epitope set comprising epitopes from SARS-CoV-2 proteins (nucleoproteins, membrane, envelope small membrane, ORF3a, and ORF8 protein) used in designing SANV constructs.

Protein Name	Types of Epitopes	IEBD ID	Epitope Sequence with Position (Name)	HLA Binding Allele(s)	Positive T Cell Assay(s)	Population Coverage	Peptide Synthesis Score	IEDB-Based Predicted CD4/CD8 Immunogenicity Score	CD8 Immunogenicity Prediction by DeepImmuno			
									High Frequency MHC Allele (Frequency)	Score	Other HLA Alleles	Score
N	B lymphocyte (BL)	1131160	81DDQIGYYRRA TRRIR95 (BL1)	HLA-DRB1*07:01, HLA-DRB1*15:01, HLA-DRB1*01:01, HLA-DRB1*04:05, HLA-DRB1*08:02, HLA-DRB1*09:01, HLA-DRB1*11:01, HLA-DRB3*01:01, HLA-DRB5*01:01, HLA-DRB1*04:01, HLA-DRB3*02:02, HLA-DRB1*03:01, HLA-DRB1*12:01, HLA-DRB1*13:02, HLA-DRB4*01:01, HLA-DPB1*02:01, HLA-DRB1*08:03, HLA-DRB1*04:04, HLA-DRB1*14:05	Release of IFN-γ, TNF-α, IL-5, and activation	88.05%	0.95874	66.8175				
M		1310529	166KEITVATSRT LSYYK180 (BL2)	HLA-DRB1*07:01, HLA-DRB1*15:01, HLA-DRB1*11:01, HLA-DRB1*01:01, HLA-DRB1*03:01, HLA-DRB1*04:01, HLA-DRB1*04:05, HLA-DRB1*08:02, HLA-DRB1*09:01, HLA-DRB1*12:01, HLA-DRB1*13:02, HLA-DRB3*01:01, HLA-DRB4*01:01, HLA-DRB5*01:01, HLA-DRB3*02:02, HLA-DPB1*02:01, HLA-DRB1*04:04	Release of IFN-γ, TNF-α, and activation	87.17%	0.88896	91.8158				

Table 2. *Cont.*

Protein Name	Types of Epitopes	IEBD ID	Epitope Sequence with Position (Name)	HLA Binding Allele(s)	Positive T Cell Assay(s)	Population Coverage	Peptide Synthesis Score	IEDB-Based Predicted CD4/CD8 Immunogenicity Score	CD8 Immunogenicity Prediction by DeepImmuno			
									High Frequency MHC Allele (Frequency)	Score	Other HLA Alleles	Score
E	B lymphocyte (BL)	1310627	51LVKPSFYVYS RVKNL65 (BL3)	HLA-DRB1*07:01, HLA-DRB1*15:01, HLA-DPB1*02:01, HLA-DRB1*01:01, HLA-DRB1*04:01, HLA-DRB1*04:05, HLA-DRB1*08:02, HLA-DRB1*09:01, HLA-DRB1*11:01, HLA-DRB1*12:01, HLA-DRB1*13:02, HLA-DRB3*01:01, HLA-DRB3*02:02, HLA-DRB4*01:01, HLA-DRB5*01:01, HLA-DRB1*03:01, HLA-DRB1*04:04	Release of IFN-γ	87.17%	0.90733	63.0472				
ORF8 protein		1310428	41FYSKWYI RVGARKSA55 (BL4)	HLA-DRB1*07:01, HLA DRB1*15:01, HLA-DRB1*01:01, HLA-DRB1*04:01, HLA-DRB1*04:05, HLA-DRB1*08:02, HLA-DRB1*09:01, HLA-DRB1*11:01, HLA-DRB1*12:01, HLA-DRB3*01:01, HLA-DRB3*02:02, HLA-DRB4*01:01, HLA-DRB5*01:01, HLA-DRB1*03:01, HLA-DRB1*04:04, HLA-DRB1*13:02	Release of IFN-γ, TNF-α, IL-5, and activation	83.81%	0.92548	84.5565				

Table 2. *Cont.*

Protein Name	Types of Epitopes	IEBD ID	Epitope Sequence with Position (Name)	HLA Binding Allele(s)	Positive T Cell Assay(s)	Population Coverage	Peptide Synthesis Score	IEDB-Based Predicted CD4/CD8 Immunogenicity Score	CD8 Immunogenicity Prediction by DeepImmuno			
									High Frequency MHC Allele (Frequency)	Score	Other HLA Alleles	Score
N	Helper T lymphocyte (HTL) epitopes	1329005	86YYRRATRRIRG GDGK100 (HTL1)	HLA-DRB1*07:01, HLA-DRB1*15:01, HLA-DRB1*01:01, HLA-DRB1*08:02, HLA-DRB1*09:01, HLA-DRB1*11:01, HLA-DRB3*01:01, HLA-DRB4*01:01, HLA-DRB5*01:01, HLA-DRB1*04:01, HLA-DRB1*04:05, HLA-DRB1*12:01, HLA-DRB3*02:02, HLA-DRB1*03:01, HLA-DRB1*13:02, HLA-DRB1*08:03, HLA-DPB1*02:01, HLA-DRB1*04:04, HLA-DRB1*14:05	Release of IFN-γ, TNF-α and activation	88.05%	0.96146	Not predicted				
M		1310622	176LSYYKLGAS QRVAGD190 (HTL2)	HLA-DRB1*15:01, HLA-DRB1*01:01, HLA-DRB1*04:01, HLA-DRB1*07:01, HLA-DRB1*11:01, HLA-DRB1*04:05, HLA-DRB1*08:02, HLA-DRB1*09:01, HLA-DRB1*13:02, HLA-DRB3*01:01, HLA-DRB3*02:02, HLA-DRB4*01:01, HLA-DRB5*01:01, HLA-DRB1*03:01, HLA-DRB1*12:01, HLA-A*02:01, HLA-A*03:01, HLA-A*11:01, HLA-A*24:02, HLA-DPB1*02:01, HLA-DQA1*01:01/DQB1*05:01, HLA-DQA1*01:02/DQB1*06:02, HLA-DQA1*05:01/DQB1*02:01, HLA-DQA1*05:01/DQB1*03:01, HLA-DPA1*01:03/DPB1*04:01, HLA-DQA1*03:01/DQB1*03:02, HLA-DRB1*04:04	Release of IFN-γ, TNF-α activation, and degranulation	87.17%	0.8392	85.1196				

Table 2. *Cont.*

Protein Name	Types of Epitopes	IEBD ID	Epitope Sequence with Position (Name)	HLA Binding Allele(s)	Positive T Cell Assay(s)	Population Coverage	Peptide Synthesis Score	IEDB-Based Predicted CD4/CD8 Immunogenicity Score	CD8 Immunogenicity Prediction by DeepImmuno			
									High Frequency MHC Allele (Frequency)	Score	Other HLA Alleles	Score
ORF3a	Helper T lymphocyte (HTL) epitopes	1310751	116QSINFVRII MRLWLC130 (HTL3)	HLA-DRB1*07:01, HLA-DRB1*15:01, HLA-DRB1*01:01, HLA-DRB1*03:01, HLA-DRB1*04:01, HLA-DRB1*04:05, HLA-DRB1*08:02, HLA-DRB1*09:01, HLA-DRB1*11:01, HLA-DRB1*12:01, HLA-DRB4*01:01, HLA-DRB5*01:01, HLA-DRB1*04:04, HLA-DRB1*13:02, HLA-DRB3*01:01, HLA-DRB3*02:02	Release of IFN-γ, TNF-α. IL-5 release and activation	83.81%	0.67659	81.5944				
N	Cytotoxic T lymphocyte (CTL) epitopes	33667	361KTFPPTEPK 369 (CTL1)	HLA-A*11:01, HLA-A*03:01, HLA-A*02:01, HLA-A*31:01, HLA-A*01:01, HLA-B*07:02, HLA-B*15:01, HLA-B*40:01, HLA-B*58:01, HLA-A*68:01, HLA-A*24:02, HLA-A*26:01, HLA-A*33:01, HLA-A*69:01, HLA-B*08:01, HLA-B*27:05	Release of IFN-γ, TNF-α, IL-2, cytotoxicity, and activation	94.48%	0.99998	0.1306	HLA-A*02:01 (21.95)	0.79123	HLA-B*0801	0.86470383
											HLA-A*0301	0.84171104
											HLA-A*6802	0.81842554
											HLA-A*0201	0.79123014
											HLA-B*3501	0.62893331
M		5149	171ATSRTLSYY179 (CTL2)	HLA-A*01:01, HLA-A*03:01, HLA-A*11:01, HLA-A*26:01, HLA-A*29:02, HLA-A*30:02, HLA-A*31:01, HLA-A*68:01, HLA-A*23:01, HLA-A*24:02, HLA-A*33:01	Release of IFN-γ, activation and cytotoxicity	77.68%	0.99995	−0.17295	HLA-A*24:02 (11.33)	0.18188	HLA-A*0301	0.91671658
											HLA-A*1101	0.69838208
											HLA-B*0801	0.63991845
											HLA-B*3501	0.61305189
											HLA-A*6802	0.43553025

Table 2. *Cont.*

Protein Name	Types of Epitopes	IEBD ID	Epitope Sequence with Position (Name)	HLA Binding Allele(s)	Positive T Cell Assay(s)	Population Coverage	Peptide Synthesis Score	IEDB-Based Predicted CD4/CD8 Immunogenicity Score	CD8 Immunogenicity Prediction by DeepImmuno			
									High Frequency MHC Allele (Frequency)	Score	Other HLA Alleles	Score
E	Cytotoxic T lymphocyte (CTL) epitopes	35886	19LFLAFVVFLL28 (CTL3)	HLA-A*01:01, HLA-A*02:07, HLA-A*23:01, HLA-A*26:01, HLA-A*29:02, HLA-A*30:02, HLA-A*24:02	Release of IFN-γ	51.01%	0.99976	0.32115	HLA-A*24:02 (11.33)	0.4055	HLA-A*6802	0.96065456
											HLA-A*0202	0.95476264
											HLA-A*0301	0.90145504
											HLA-B*0801	0.86044049
											HLA-B*3501	0.84200841
ORF3a		1311180	139LLYDANYFL147 (CTL4)	HLA-A*02:01, HLA-A*24:02, HLA-C*07:01	Release of IFN-γ, TNF-α, cytotoxicity activation and degranulation	64.14%	0.99989	0.11841	HLA-A*02:01 (21.95)	0.622939	HLA-A*6802	0.81244862
											HLA-B*0801	0.80622929
											HLA-B*3501	0.79976201
											HLA-A*0301	0.77097487
											HLA-A*1101	0.68420529

3.3. In Silico Evaluation of Screened Minimal Epitope Set

3.3.1. Analysis of Combined Population Coverage

The population coverage analysis provides additional insight into the efficacy of the minimal epitope set across the global population and can inform in silico vaccine design and optimization strategies of real-world vaccine sequences [73,74]. For the World, East Asia, Europe, West Indies, and North America, a combined (Class I and Class II) percent population coverage assessment of the screened minimal epitope set (4BL epitopes, 3HTL epitopes, and 4 CTL epitopes) showed 99.67, 99.66, 99.93, 99.25, and 99.79, respectively (Figure 3). Therefore, the identified minimal epitope set is expected to retain its effectiveness and applicability in global vaccine development against newly developing SARS-CoV-2 variants.

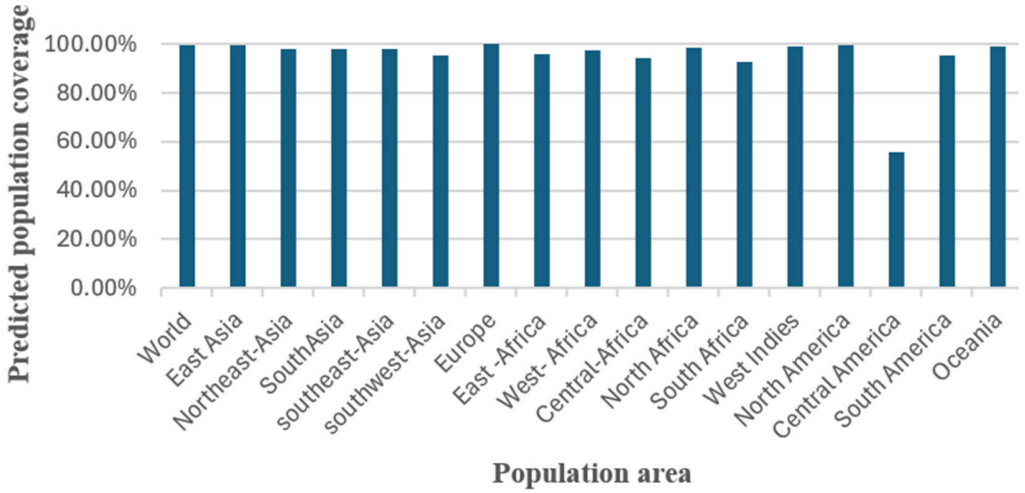


Figure 3. Diagrammatic representation of the combined (HLA class I and II) predicted population coverage for the screened minimal epitope set (n = 11) across 16 geographical areas and the world, including frequencies of 3245 alleles. The HLA allele frequencies and associated data for different populations from worldwide studies were obtained from the Allele Frequency Net Database.

3.3.2. Analysis of Cytokine-Inducing Potential and Antibody-Specific B-Cell Epitopes of BL and HTL Epitopes

Interferon-gamma (IFN-γ) is a crucial cytokine predominantly secreted by activated T cells and natural killer (NK) cells. It plays a key role in modulating immune responses by activating macrophages, enhancing antigen presentation, stimulating the innate immune system, and contributing to antiviral and antibacterial defenses [75]. IFN-γ also regulates both humoral and innate immune functions, playing significant roles in antiviral, antitumor, and immunoregulatory mechanisms. Table 2 reports IEDB-restricted data from experimental positive T-cell assays for specific cytokine-inducing characteristics of selected BL and HTL epitopes. These positive T-cell tests provide clarity on the immunological responses triggered by epitopes. For example, according to experimental cytokine assay reports available in IEDB, BL1 and BL4 epitopes were found to induce IFN-γ, TNF-α, and IL-5, as well as activate immune cells. BL2 and HTL1 triggered the release of IFN-γ and TNF-α, leading to significant immune activation. BL3 was specifically associated with IFN-γ release, whereas HTL2 induced IFN-γ, TNF-α, and TNF release, along with cellular activation and degranulation. HTL3 induced the production of IFN-γ, TNF-α, and IL-5 and activated immune cells. Moreover, the selected epitopes for vaccine design were further predicted to assessed for their ability to induce the production of key cytokines, including IFN-γ, IL-4, and IL-10. Additionally, the IgPred server was employed to predict antibody class-specific B-cell epitopes, enabling the identification of epitopes capable of inducing specific antibody isotypes such as IgG, IgE, and IgA. Predictions indicated that BL1 and BL2 epitopes induced both IFN-γ and IL-4 but did not induce IL-10. Additionally, BL1 was

identified as an IgG-specific epitope. In contrast, BL3 and BL4 did not induce IFN-γ but were positive for IL-4 and IL-10. Among the HTL epitopes, HTL1 stimulated IFN-γ and IL-4 but not IL-10, whereas HTL2 and HTL3 induced only IL-4 with no induction of IFN-γ and IL-10.

3.3.3. Evaluation of the Immunogenicity of Epitope

Among the minimal epitope set, a few HLA class I peptide complexes may be better recognized by CTL, as predicted by the IEDB-based Class I Immunogenicity score [76]. However, the CD4 T cell immunogenicity predictor identified the allele-independent HTL immunogenicity at the population level [77]. The immunogenicity analysis of the selected minimal epitope set, comprising BL, HTL, and CTL epitopes, yielded promising results using IEDB-based Class I and Class II pMHC immunogenicity prediction tools. These tools estimate the probability that a given peptide will elicit an immune response. The scoring system for HLA class I (CTL) epitopes is directly proportional to immunogenicity, with higher scores indicating greater immunogenicity [76]. Conversely, for HLA class II (HTL and BL) epitopes, the scoring is inversely proportional; lower scores indicate higher immunogenicity, while higher scores indicate reduced T helper cell-stimulatory capacity. Among the BL epitopes, the peptide BL2 showed the highest predicted immunogenicity score of 91.8158, followed by BL4 with 84.5565. The peptides BL1 and BL3 had the lowest immunogenicity score (66.8175 and 63.0472), indicating a relatively higher immunogenic potential. For HTL epitopes, the peptide HTL2 exhibited the highest predicted immunogenicity score, 85.1196, followed by HTL3 with a score of 81.5944. The immunogenicity score for HTL1 was found to be immunogenic at the 50% percentile rank threshold. Among the CTL epitopes, all peptides showed low immunogenicity scores, indicating favorable potential to induce cytotoxic responses. CTL2 had the lowest score (−0.17295), suggesting the strongest immunogenic potential, followed by CTL4 (0.11841), CTL1 (0.1306), and CTL3 (0.32115) (Table 2).

Additionally, the immunogenicity analysis of four CTL epitopes was exciting, as predicted by the DeepImmuno-CD8 web server. This tool estimates the probability of inducing a CD8+ T cell response using a neural network-based model that integrates peptide sequence characteristics and MHC allele-specific context. The immunogenicity score generated by this tool ranges from 0 to 1, with values closer to 1.0 indicating greater immunogenicity. Among the epitopes, CTL1 showed strong immunogenic potential with high-frequency allele HLA-A*02:01 (0.7912) and even higher scores with other alleles, including HLA-B*08:01 (0.8647), HLA-A*03:01 (0.8417), and HLA-A*68:02 (0.8184), indicating broad population coverage. CTL4 also demonstrated favorable immunogenicity with HLA-A*02:01 (0.6229) and high scores across multiple alleles, including HLA-A*68:02 (0.8124), HLA-B*08:01 (0.8062), and HLA-B*35:01 (0.7998), suggesting it is a strong candidate for inducing cytotoxic responses across diverse HLA backgrounds. CTL3 (19LFLAFVVFLL28) exhibited moderate immunogenicity with its high-frequency allele HLA-A*24:02 (0.4055) but scored highly with HLA-A*68:02 (0.9607) and HLA-A*02:02 (0.9548), as well as HLA-A*03:01 (0.9015) and HLA-B*35:01 (0.8420), highlighting its cross-allelic immunogenicity. In contrast, CTL2 had the lowest score with HLA-A*24:02 (0.1819), indicating a relatively poor response, but it performed strongly with HLA-A*03:01 (0.9167) and moderately with HLA-A*11:01 (0.6984) and HLA-B*08:01 (0.6399). Overall, CTL1 and CTL4 emerged as the most consistently immunogenic epitopes across multiple high-frequency HLA alleles, particularly HLA-A*02:01, HLA-A*03:01, and HLA-B*08:01, which are widely distributed in global populations. These findings support their potential inclusion in CD8+ T cell-targeted vaccine formulations to achieve broader immune coverage.

3.3.4. Analyzing TCRMatch and MAIT Match for Minimal Epitope Set

The TCRMatch tool (IEDB-based) demonstrated excellent similarity between the CDR3β sequences of the selected optimal CTL epitopes (CTL1, CTL2, and CTL4) and those of other epitopes from the same or different pathogens/antigens. This analysis aimed to identify CDR3β sequences that potentially share epitope specificity by comparing them with curated CDR3β sequences available in the IEDB (Supplementary File S4; Table S1). TCRMatch performs sequence similarity analysis using a k-mer-based scoring algorithm to rank candidate CDR3β sequences based on their likelihood of identifying the same epitope [78]. Though a small TCR sequence change can drastically alter antigen-specificity, affinity, and other properties of a TCR [79]. However, identifying the specific epitopes targeted by different TCRs in humans would be valuable, as cross-reactive SARS-CoV-2 T cells and influenza virus-specific T cells shared similarities in TCR CDR3β sequences [80,81]. Therefore, sequence similarity revealed by TCRMatch (using the BLOSUM62 observed frequency matrix) between two TCRs (TCR β-chain CDR3 sequences) probably has the same epitope specificity. Currently, the recommended threshold for matches in the TCRMatch tool is 0.97, which yielded a precision of 0.699 and a recall of 0.078 in an independent test repertoire sequencing dataset published by 10x Genomics. Lower thresholds of 0.90 and 0.84 may provide unrelated CDR3b sequences [78]. For the CTL1 epitope, the CDR3β sequences showed high similarity scores ($\geq$0.97), or perfect matches to CDR3β sequences of epitopes IVTDFSVIK and AVFDRKSDAK (Epstein-Barr nuclear antigen 4, Epstein–Barr virus), CRVLCCYVL (regulatory protein IE1, Human cytomegalovirus), MGYINVFAFPFTIYSL (ORF10 protein, SARS-CoV-2), GLCTLVAML (transcriptional regulator IE63 homolog, Varicella-zoster virus), FLWLLWPVTLACFVLAAV, SELVIGAVIL, HLRIAGHHLGR, SYFIASFRLFA (membrane glycoprotein, SARS-CoV-2), FQPQNGQFI, LPRRSGAAGA, DATYQRTRALVR, LLLDRLNQL, AQFAPSASAFFGMSR (nucleoprotein, SARS-CoV-2), NLVPMVATV, TPRVTGGGAM (UL83/pp65, Human cytomegalovirus), VLAWLYAAV (nonstructural polyprotein pp1a, SARS-CoV-2), VMATRRNVL (uncharacterized protein Rv1518/MT1568, Mycobacterium tuberculosis), KLGGALQAK (55 kDa immediate-early protein 1, Human cytomegalovirus), MIELSLIDFYLCFLAFLLFLVLIML, IMLIIFWFSL (ORF7b protein, SARS-CoV-2), HYNYMCNSSCMGGMNRRPILTIITL (cellular tumor antigen p53, Homo sapiens), MEVTPSGTWL (nucleocapsid protein, SARS-CoV-2), RLDKVEAEV, FTISVTTEIL, VQPTESIVRFPNITNLCPF, KLPDDFTGCV, RSVASQSIIAYTMSL, GTHWFVTQR, YLQPRTFLL, YAWNRKRISNCVADYSVLYNSASFSTFKCYGVSPTKLNDLCFT, GYQPYRVVVLSF, YFPLQSYGF, VLPFNDGVYFASTEK (surface glycoprotein, SARS-CoV-2), RQLLFVVEV, FLNGSCGSV, VVYRGTTTY, APKEIIFLEGETL, TVLSFCAFAV, HTTDPSFLGRY, MMISAGFSL, VLWAHGFEL, FVDGVPFVV, LLLDDFVEII, VPHVGEIPVAYRKVLL, KLSYGIATV, YIFFASFYY (orf1ab polyprotein, SARS-CoV-2), KTFPPTEPK (nucleocapsid phosphoprotein, SARS-CoV-2), GILGFVFTL (matrix protein 1, Influenza A virus), YVLDHLIVV (replication and transcription activator, SARS-CoV), FVCNLLLLFVTVYSHLLLV, GLEAPFLYLYALVYFLQSINFVRIIMR (ORF3a protein, SARS-CoV-2), SPFHPLADNKFAL (ORF7a protein, SARS-CoV-2), CINGVCWTV (genome polyprotein, unspecified virus), ILLIIMRTFKVSIWNLDYII (ORF6 protein, SARS-CoV-2), VVLSWAPPV (fibronectin type III domain-containing protein 3B, Homo sapiens), SSLENFRAYV (polymerase basic protein 2, Influenza A virus), and YEDFLEYHDVRVVL (ORF8 protein, SARS-CoV-2). Additionally, the CTL2 epitope's CDR3β sequences show a high similarity score of 0.977 with those of the epitope KPFERDISTEIY (surface glycoprotein, SARS-CoV-2). The CTL4 epitope's CDR3β sequences have a high similarity score of more than 0.9, or even a perfect match with other CDR3β sequences of epitopes LLWNGPMAV (non-structural protein NS4b, Yellow fever virus 17D), KLGGALQAK (55 kDa immediate-early protein 1, Human herpesvirus 5), LPRRSGAAGA (nucleoprotein, Influenza A virus), TPRVTGGGAM

and NLVPMVATV (UL83, Human herpesvirus 5), STLPETAVVRR (precore/core protein, Hepatitis B virus), KTAYSHLSTSK (polymerase, Hepatitis B virus), LSPRWYFYYL (nucleocapsid phosphoprotein, SARS-CoV-2), RVRAYTYSK (replication and transcription activator, Epstein–Barr virus strain B95-8), NPLLYDANYFLCW and LLYDANYFL (ORF3a protein, SARS-CoV-2), TLLANVTAV (VP6 protein, Human rotavirus), AVFDRKSDAK (Epstein–Barr nuclear antigen 4, Epstein–Barr virus), MGYINVFAFPFTIYSL (ORF10 protein, SARS-CoV-2), KAYNVTQAF and NPANNASIV (nucleoprotein, SARS-CoV-2), VLAWLYAAV (non-structural polyprotein pp1a, SARS coronavirus Urbani), KMVAVFYTT (olfactory receptor 5M8, Homo sapiens), FLNGSCGSV, FVDGVPFVV, TTLPVNVAF, TLLANVTAV (VP6 protein, Human rotavirus strain WA), AVFDRKSDAK (Epstein–Barr nuclear antigen 4, Human herpesvirus 4), RVRAYTYSK (replication and transcription activator, Human herpesvirus 4 strain B95-8), VMTTVLATL (uncharacterized protein Rv1734c/MT1774.1, Mycobacterium tuberculosis), YEDFLEYHDVRVVL (ORF8 protein, SARS-CoV-2), YEGNSPFHPL, SYFIASFRLFA, FLWLLWPVTLACFVLAAV, WICLLQFAY (membrane glycoprotein, SARS-CoV-2), NEGVKAAW (regulatory protein IE2, Human herpesvirus 5), CALDPLSETK, FLPFFSNVTWFHAI, AYSNNSIAIPTNFTISV, VLPFNDGVYFASTEK, LEPLVDLPI (surface glycoprotein, SARS-CoV-2), KLSYGIATV, LLLDDFVEII, FLNGSCGSV, VLWAHGFEL, NEKQEILGTVSWNL, AELAKNVSLDNVL, QLMCQPILLL, SNEKQEILGTVSWNL, FVDGVPFVV, YIFFASFYY, APKEIIFLEGETL, TTLPVNVAF, HTTDPSFLGRY, FLPRVFSAV, TLVPQEHYV, IPRRNVATL (orf1ab polyprotein, SARS-CoV-2), MIELSLIDFYLCFLAFLLFLVLIML, VQELYSPIFLIV, YEGNSPFHPL (ORF7a protein, SARS-CoV-2), IMLIIFWFSL, MIELSLIDFYLCFLAFLLFLVLIML, TTLPVNVAF, and FVDGVPFVV (ORF7b protein, SARS-CoV-2) (Supplementary File S4; Table S2).

Utilizing the MAIT Match 1.0 tool, which assigns similarity scores ranging from 0 to 1 (with 1 indicating a perfect match), an analysis was conducted to compare SARS-CoV-2 TCR (CDR3β) sequences with known MAIT cell TCRs. The results revealed that most of the examined TCR sequences from CTL1 and CTL4 exhibited match scores greater than 0.84, indicating a high degree of similarity to known MAIT TCR sequences. For CTL1, the CDR3β sequence CASSEGYGYTF found the MAIT hit CAASKSGYSTLT with the greatest similarity score (0.8589), indicating the closest match. Another strong match was found between CASSEGLGELFF and CAEAQGGTALIF, with a similarity score of 0.8549. The CDR3β sequence CASSGDRAEKLFF matched with MAIT hit CVVSGSDGQKLLF, scoring 0.8531, while the CDR3β sequence CASSGGNGELFF matched with CAAGGQNFVF, showing a score of 0.8532. The higher similarity scores were observed for the CDR3β sequences of CTL4. For example, ASSLSGSTEAF matched with the MAIT hit CAASKSGYSTLT, yielding a score of 0.8801, indicating the nearest match. Another strong match was found between ASSISGSTEAF and CAASKSGYSTLT, with a match score of 0.878. The sequence ASSLAGSTEAF also aligned closely with CAASKSGYSTLT, showing a score of 0.8754 (Supplementary Materials Table S1).

3.3.5. Heterologous Shared Epitope Identification

Heterologous shared epitopes are peptide sequences conserved across different pathogens. Several studies have explored the potential of vaccine repurposing by leveraging heterologous immunity [11,82,83]. This approach relies on the immune system's capacity to recognize and respond to pathogens that share epitopes with those targeted by previously developed vaccines [84]. In this context, this study conducted a comprehensive analysis of fully conserved heterologous epitopes from screened optimal epitope sets (BL1–BL4, HTL1–HTL2, and CTL1–CTL4) across diverse viral proteins, highlighting their potential to promote immune cross-reactivity and guide the design of broad-spectrum vaccines. In Horseshoe bat sarbecovirus, shared epitopes included 81DDQIGYYRRATRRIR95, 165KEIT-

VATSRTLSYYK179, 51LVKPSFYVYSRVKNL65, and 41FYSKWYIRVGARKSA55 against the epitopes BL1, BL2, BL3, and BL4, respectively. Similarly, in the Rhinolophus thomasi bat coronavirus, epitope matches were found at 81DDQIGYYRRATRRIR95 (BL1), 165KEITVATSRTLSYYK179 (BL2), and 361KTFPPTEPK369 (CTL1). In Pangolin coronavirus, conserved regions included 81DDQIGYYRRATRRIR95, 166KEITVATSRTLSYYK180, 51LVKPSFYVYSRVKNL65, and 41FYSKWYIRVGARKSA55 against BL1 to BL4, and 86YYRRATRRIRGGDGK100, 176LSYYKLGASQRVAGD190, and 116QSINFVRIIMRLWLC130 against HTL1 to HTL3. Furthermore, shared CTL epitopes were identified in the Pangolin coronavirus at 359KTFPPTEPK367, 171ATSRTLSYY179, 19LFLAFVVFLL28, and 139LLYDANYFL147, corresponding to epitopes CTL1, CTL2, CTL3, and CTL4, respectively. Similarly, in *Rhinolophus siamensis* bat sarbecovirus, matched epitopes were 165KEITVATSRTLSYYK179 (BL2), 171ATSRTLSYY179 (CTL2), and 362KTFPPTEPK370 (CTL1). In Jingmen Rhinolophus sinicus betacoronavirus 1, shared peptides were found at 165KEITVATSRTLSYYK179 (BL2), 171ATSRTLSYY179 (CTL2), and 362KTFPPTEPK370 (CTL1), while *Sarbecovirus* species. revealed matches at 165KEITVATSRTLSYYK179 (BL2), 19LFLAFVVFLL28 (CTL3), and 171ATSRTLSYY179 (CTL2) (Supplementary File S4; Table S3). These shared, fully conserved epitopes across various *Sarbecoviruses* and hosts suggest significant potential for heterologous immunity and support the design of broadly protective, cross-reactive vaccines. As the selected epitopes used in the vaccine designs passed through the PepMatch tool (with zero mismatches) against the human reference proteome, they are unlikely to exhibit cross-reactivity with self-epitopes, thereby reducing the risk of autoimmunity.

3.4. Designing of Coiled-Coil Self-Assembling Peptide Vaccine (SANV) Constructs

Several research groups have reported the development of SAPN-based vaccine candidates designed to enhance immunogenicity. Examples include vaccines for HIV, FMP014, SARS nanoparticle, Tetra-M2e, SAPN-K, LFC4, NP-L/C, P6c, P6HRC1, P4c-Mal SAPN, Mono-M2e, PfCSP-KMY SAPN, MPER-SAPN, $GRA7_{(20–28)}$ SAPN, SAPN-Combo, and PfCSP-SAPN [40–49]. In this study, an innovative approach was employed to design multi-epitope vaccines using self-assembling coiled-coil peptide motifs, specifically pentameric and trimeric domains, which exhibit inherent self-adjuvant properties, are non-toxic, and effectively overcome the challenge of low immunogenicity [36,85]. There are two kinds of SANV constructs that were developed: SANVa (Figure 2A), which lacks adjuvant/TAT/PADRE sequences, and SANVb (Figure 2B), which incorporates them. A total of 12 constructs were designed for each category (SANVa1–12 and SANVb1–12), as detailed in Table 3.

In the SANVa1–12 constructs, trimeric and pentameric peptide motifs derived from various existing SAPN-based platforms such as PSAPN-K, LFC4, NP-L/C, P6c, P6HRC1, P4c-Mal SAPN, Mono-M2e, PfCSP-KMY SAPN, MPER-SAPN, $GRA7_{(20–28)}$ SAPN, SAPN-Combo, and PfCSP-SAPN were linked using GG linkers. CTL epitopes were joined via GGGS linkers, while HTL and BL epitopes were connected using GPGPG linkers. The use of GGGS and GPGPG linkers ensures structural integrity and improves the interaction between vaccine components and immune receptors by promoting proper protein folding, stability, and antigen presentation [86]. Glycine (G) enhances linker flexibility, whereas proline (P) imparts rigidity, supporting loop formation in the peptide chain [85]. In contrast, the SANVb1–12 constructs used a different combination of linkers, including GG, GGGS, KK, AAY, and GPGPG, to connect epitopes, adjuvants, Pan-HLA DR-binding elements (PADRE), and the TAT sequence. The CTL epitopes were linked using the AAY linker, which facilitates interaction with the TAP transporter and enhances epitope presentation. BL epitopes were connected using KK linkers, and HTL epitopes were joined with GPGPG

linkers to retain immunogenicity and enhance T-helper responses [67,87,88]. In addition, the pentamer and HTL epitope were linked by the GPGPG linker, whereas the pentamer and trimer domains were linked by the GG linker. To further improve immunogenicity, PADRE sequences were introduced at the N-terminal via the EAAAK linker to promote broad binding to mouse and human MHC class II molecules, thereby stimulating helper T-cell responses [87]. Following PADRE, a human β-defensin-3 sequence was incorporated as an adjuvant to activate innate immunity and attract naive T cells through the CCR6 chemokine receptor [89,90]. A TAT peptide was added to the C-terminal to enhance intracellular delivery of the vaccine construct [91].

3.5. 3D Structural Analysis, Refinement, and Validation of SANV Constructs

Prediction of protein tertiary structure methods are generally categorized into 2 main approaches: (i) template-based modeling (TBM), which includes homology modeling, threading, and fold recognition, and (ii) template-free modeling (TFM), also known as ab initio modeling. More recently, advanced hybrid approaches like AlphaFold2 have emerged, incorporating deep learning techniques, including convolutional neural networks, trained on Protein Data Bank (PDB) structures. These methods predict inter-residue distance distributions by leveraging multiple sequence alignment (MSA) features derived from diverse protein sequence databases. Additionally, AlphaFold2 identifies structurally related proteins to generate an initial illustration of the target sequence, referred to as the pair representation. Despite its remarkable performance, demonstrated by an RMSD of approximately 0.8 Å compared to ~2.8 Å achieved by the next best method in CASP14, AlphaFold2 has certain limitations. These include: (i) reduced accuracy in modeling intrinsically disordered regions and flexible surface-exposed loops, (ii) a tendency to overestimate secondary structure elements, particularly α-helices, within loop regions, and (iii) inconsistencies in predicting the positioning of transmembrane domains in membrane proteins [92]. Though the updated AlphaFold 3 model also showed significant limitations in accurately predicting the structures of terminal tags when placed in the context of a chimeric protein, as they disrupt the evolutionary signals that MSAs leverage [93,94], this study made the three-dimensional (3D) structures prediction for 24 monomeric vaccine constructs (SANVa1–12 and SANVb1–12), yielding weak prediction metrics of pTM values (0.21–0.29) (Table 4). Therefore, for screening of suitable monomers for self-assembly, the 3D structures of 24 SANV constructs were successfully predicted using the GalaxyTBM tool available on the GalaxyWEB platform. For each construct, five different models were generated. To evaluate the structural stability and quality of each model, three validation tools, ERRAT, Ramachandran plot, and ProSA-web, were employed (Supplementary File S4; Table S4). ERRAT analysis measures the quality factor based on non-bonded atomic interactions [95], while the Ramachandran plot determines the percentage of residues located within energetically favorable regions. A threshold of over 85% residues in the favored region was considered indicative of good structural quality [96]. The ProSA-web tool was used to compute Z-scores, which reflect the overall model quality by detecting potential errors in the 3D structure [54]. Based on these assessments, the top model for each SANV construct, those with the highest ERRAT score and more than 80% of residues in the favored region of the Ramachandran plot, was selected for structural refinement. Refinement was performed using the GalaxyRefine server, which provided multiple validation parameters, including Global Distance Test-High Accuracy (GDT-HA), root mean square deviation (RMSD), MolProbity score, clash score, percentage of poor rotamers, and Ramachandran-favored residue percentage (Supplementary File S4; Table S5). The GDT-HA and RMSD scores were specifically used to assess the global structural deviations from the primary models, focusing on the positioning accuracy of Cα atoms. Higher GDT-HA and lower

RMSD values were considered indicative of improved structural accuracy [97]. The local structural quality of both pre- and post-refined models was assessed using the MolProbity score, which measures their physical level of accuracy, particularly with respect to steric clashes, based on statistical data from high-resolution protein structures [98]. The most reliable refined model for each construct (SANVa and SANVb) was identified by the lowest MolProbity score and subsequently used for self-assembly analysis (Table 4). This systematic evaluation approach improved the overall accuracy and reliability of the modeled SANV structures.

3.6. Prediction and Analysis of SANV Constructs Through Homo-Oligomerization

The SANV platform was used by Vakili et al. [99] in prior work to create a nanovaccine comprising eight immunodominant Leishmania infantum epitopes, linked by pentameric and trimeric coiled-coil motifs and spacer sequences. Building upon that foundation, this study generated five possible homo-oligomeric models (restricted to 12-mers) for each of the 12 SANV constructs using the GalaxyHomomer tool (Supplementary File S4; Table S6). Among these, two models (model 5 of SANVa9 and model 3 of SANVb6) were selected for subsequent analyses based upon the interface area of the homo-oligomeric structures (Table 5). The interface area denotes the contact surface between interacting subunits within the oligomer, where a larger interface typically indicates stronger inter-subunit interactions, contributing to an enhanced, stable, and functional structure. GalaxyHomomer integrates template-based modeling (TBM) via GalaxyTBM, using ab initio docking when fewer than 5 homologous templates are available. This approach generally yields reliable predictions for homodimeric complexes, especially when high-quality templates are available [100]. However, its performance tends to decline for higher-order oligomers or when appropriate homologous templates for the complex are lacking. Moreover, the accuracy of ab initio docking predictions can be enhanced by integrating subunit and complex modeling and by separating intra- and inter-chain interactions [101]. Recent studies indicate that protein function is not only dictated by static three-dimensional structures, but is also largely influenced by dynamic transitions among multiple conformational states encoded within the amino acid sequence. While static models typically represent low-energy conformations, they fail to capture the complex, multiscale dynamics involved in self-assembly during multimer formation. Consequently, important conformational changes occurring during assembly may be overlooked. Therefore, combining a detailed examination of dynamic data with static structural models offers a deeper understanding of the role of proteins and provides deeper insights into hierarchical self-assembly processes, in which individual monomers first organize into uniform subunits, which subsequently assemble into larger nanoparticle structures. Therefore, in addition to GalaxyHomomer, the AlphaFold2-multimer model was used to capture different coevolutionary relationships among proteins and generate distinct predicted conformations. AlphaFold2-Multimer results yielded relatively low iPTM scores for the designed 24 SANV constructs, suggesting low confidence in the exact subunit orientations (Table 5). Thus, we compared the AlphaFold-Multimer predictions of the selected SANV constructs (SANVa9 and SANVb6) with two previously characterized SAPN vaccine constructs serving as respective positive controls, MPER-SAPN (C1) and P4c-Mal SAPN (C2). The MPER-SAPN model, consisting of 38 identical chains, and SANVa9, comprising 17 chains, showed predicted template modeling (pTM) scores of 0.29 and 0.28, respectively, with corresponding interface (ipTM) scores of 0.28 and 0.27. Similarly, P4c-Mal SAPN (42 chains) and SANVb6 (14 chains) yielded comparable pTM scores of 0.29 each, and ipTM scores of 0.29 and 0.28, respectively (Figure 4C–F). The ipTM measures the accuracy of the predicted relative positions of the subunits forming the protein-protein complex. Disordered regions within the subunit may negatively affect

the ipTM score even if the complex structure is correctly predicted [102,103]. Therefore, these results suggest that AlphaFold-Multimer is not up to the task of predicting large self-assembled nanoparticle structures [104,105]. Though it could be used in large-scale initial screenings for protein-protein interactions with ipTM thresholds as low as 0.3 [106]. Three-dimensional visualization of the SANVa9 and SANVb6 oligomers (Figure 4A,B) revealed dodecameric ring-like assemblies composed of 12 identical monomers. The SAPN design is based on a geometric framework in which monomeric protein chains self-assemble into a structurally defined, mechanically and chemically stable nanoparticle [107]. The monomeric chains, composed of asymmetric coiled-coil trimeric and pentameric domains connected by a diglycine linker, self-assemble into oligomeric scaffolds. This assembly occurs along the 3-fold and 5-fold symmetry axes of higher-order polyhedral structures, such as dodecahedra, icosahedra, or related quasi-equivalent forms [42,44]. Ideally, such SAPN of icosahedral symmetry resembles virus-like particles in their architecture [44]. Conveniently, epitopes can be fused either to the trimer and/or the pentamer domain, resulting in a repetitive arrangement of multiple types of epitopes located on or close to the SAPN surface that generates highly immunogenic responses [42,48]. However, the low ipTM scores of self-assembled nanostructures of SANVa9 and SANVb6 could affect the predicted epitope density on the SAPN surface.

The self-assembly using a coiled-coil trimeric and pentameric domain has an intrinsic property to form a self-assembling peptide nanostructure. As per the mechanism suggested by Raman et al. [41,107] in their wet-lab studies, it might be theoretically possible to design a monomer (asymmetric unit) of self-assembling peptide nanoparticles (SAPN) into regular polyhedral architectures (such as dodecahedral or icosahedral forms) by linking coiled-coil trimeric and pentameric domains using a short peptide linker. Self-assembly of these monomeric units initially produces intermediate assemblies determined by the least common multiple (LCM) of their oligomerization states, which is 15. The association of multiple such intermediate units ultimately leads to the formation of larger nanoparticle structures. For instance, the generation of a well-defined polyhedral geometry, such as a dodecahedron or icosahedron, requires at least four intermediate units, each comprising 15 monomers, resulting in a total of 60 monomers. The successful organization of these intermediate units into a regular polyhedral structure is influenced by several factors, including (1) the length of the linker region, (2) the interactions at the interfaces between neighboring oligomerization domains, and (3) the individual oligomerization domains' structural arrangement. Nevertheless, even units may not have regular geometry [108]. Importantly, antigenic epitopes can be strategically fused to either the trimeric and/or pentameric domains, enabling their repetitive presentation on or near the surface of the self-assembling protein nanoparticle (SAPN), thereby enhancing immunogenic potential [42,45,48].

Table 3. The sequences of amino acids of SANVa1 to SANVa12 and SANVb1 to SANVb12, as well as the specific design of self-assembling nanostructure vaccine (SANV) construct. Linkers (black), CTL epitope (brown), HTL epitope (purple), pentamers (green), trimer (sky blue), BL epitope (red), human β-defensin-3 (orange), Pan-HLA DR (pink), and TAT (blue) are all displayed in distinct colors.

Sr No	Name of Vaccine Construct	Name of Self-Assembling Platforms	Component of Monomeric Coiled-Coil Building Blocks with Amino Acid Sequences	Amino Acid Sequence of Vaccine Construct
1	SAPVa1	SAPN-K	Pentameric domain (COMP): DEMLREL QETNAALQDVRELLRQQVKQITFLRALLM Linker: GG Trimeric domain (de novo designed leucine zipper peptide): RLLAR LEELERRLEELERRLEEL ERAINTVDLELAALRRRLEELAR	KTFPPTEPKGGGSATSRTLSYYGGGSLFLAFVVFLLGGGSLLYDANYFLGPGPG YYRRATRRIRGGDGKGPGPGLSYYKLGASQRVAGDGPGPGQSINFVRIIMRL WLCGPGPGDEMLRELQETNAALQDVRELLRQQVKQITFLRALLMGGRLLAR LEELERRLEELERRLEELERAINTVDLELAALRRRLEELARGGSGDDQIGYYRRA TRRIRGPGPGKEITVATSRTLSYYKGPGPGLVKPSFYVYSRVKNL GPGPGFYSKWYIRVGARKSA
	SAPVb1			EAAAKAKFVAAWTLKAAAVEAAAK GIINTLQKYYCRVRGGRCAVLSCLPK EEQIGKCSTRGRKCCRRKKEAAAKAAYKTFPPTEPKAAYATSRTLSY YAAYLFLAFVVFLLAAYLLYDANYFLAAYYYRRATRRIRGGDGKGPGPGLSYYKL GASQRVAGDGPGPGQSINFVRIIMRLWLCGPGPGDEMLRELQETNAALQDVRELLRQQVK QITFLRALLMGGRLLARLEELERRLEELERRL EELERAINTVDLELAALRRRLEELARGGSGDDQIGYYRRATRRIRKKKEIT VATSRTLSYYKKKLVKPSFYVYSRVKNLKKFYSKWYIRVGARKSAKKTGALLA AGAAAKK
2	SAPVa2	LFC4	Pentameric domain (COMP): LAPLREL QETNAALQDVRELLRVKQITFLENTVMEC DACG Linker: GGSGSG Trimeric domain (Foldon-Laminin): QKYLEDKAQELVRLEGEVRSLLKDISEKVA VYSTGGGGGLVPRGSGYIPE APRDGQAYVRKDGENVLLSTFL	KTFPPTEPKGGGSATSRTLSYYGGGSLFLAFVVFLLGGGSLLYDANYFLGPGPGYYRRA TRRIRGGDGKGPGPGLSYYKLGASQRVAGDGPGPGQSINFVRIIMRLWLCGPGPGLAPLREL QETNAALQDVRELLRVKQITFLENTVMECDACGGGSGSGQKYLEDKAQELVRLEGEV RSLLKDISEKVAVYSTGGG GGLVPRGSGYIPEAPRDGQAYVRKDGENVLLSTFLGGSGDDQIGYYRRA TRRIRGPGPGKEITVATSRTLSYYKGPGPGLVKPSFYVYSRVKNLGPGPGFYS KWYIRVGARKSA
	SAPVb2			EAAAKAKFVAAWTLKAAAVEAAAKGIINTLQKYYCRVRGGRCAVLSCLPKEEQ IGKCSTRGRKCCRRKKEAAAKAAYKTFPPTEPKAAYATSRTLSYYAAYLFLAFVVFLL AAYLLYDANYFLAAYYYRRATRRIRGGDGKGPGPGLSYYKLGASQRVAGD GPGPGQSINFVRIIMRLWLCGPGPGLAPLRELQETNAALQDVRELLRVKQITFLENTVM ECDACGGGSGSG QKYLEDKAQELVRLEGEVRSLLKDISEKVAVYSTGGGGGLVPRGSGYIPEAPRDGQ AYVRKDGENVLLSTFLGGSGDDQIGYYRRATRRIRKKKEITVATSRTLSYYK KKLVKPSFYVYSRVKNLKKFYSKWYIRVGARKSAKKTGALLAAGAAAKK

Table 3. *Cont.*

Sr No	Name of Vaccine Construct	Name of Self-Assembling Platforms	Component of Monomeric Coiled-Coil Building Blocks with Amino Acid Sequences	Amino Acid Sequence of Vaccine Construct
3	SAPVa3	NP-L/C	Pentameric domain (derived from COMP): DEMLREQETNAALQDVRELLRQQV RQITFLCLM Linker: GG Trimeric domain (de novo designed): RLL CRLEELE RRLEELERRLEERAINTVDL ELAALRRRLE LAR	KTFPPTEPKGGGSATSRTLSYYGGGSLFLAFVVFLLGGGSLLYDANYFLGPGPG YYRRATRRIRGGDGKGPGPGLSYYKLGASQRVAGDGPGPGQSINFVRIIMRLWLC GPGPGDEMLREQETNAALQDVRELLRQQVRQITFLCLMGG RLLCRLEELERRLEELERRLEERAINTVDLELAALRRRLELARGGSG DDQIGYYRRATRRIRGPGPGKEITVATSRTLSYYKGPGPGLVKPSFYVYSRVKNL GPGPGFYSKWYIRVGARKSA
	SAPVb4			EAAAKAKFVAAWTLKAAAVEAAAK GIINTLQKYYCRVRGGRCAVLSCLPKEEQIGKC STRGRKCCRRKKEAAAKAAYKTFPPTEPKAAYATSRTLSY YAAYLFLAFVVFLLAAYLLYDANYFLAAYYYRRATRRIRGGDGKGPGPG LSYYKLGASQRVAGDGPGPGQSINFVRIIMRLWLCGPGPG DEMLREQETNAALQDVRELLRQQVRQITFLCLMGGRLLCRLEELE RRLEELERRLEERAINTVDLELAALRRRLELARGGSGDDQIGYYRRATRRIR KKKEITVATSRTLSYYKKKLVKPSFYVYSRVKNLKKFYSKWYIRVGA RKSAKKTGALLAAGAAAKK
4	SAPVa4	P6c	Pentameric domain (derived from COMP): DELREQETNAALQDVRELLRQQVRQ ITFLRCLLM Linker: GG Trimeric domain (de novo designed): RLLCRLEELERRLEELERRLEEL ERAINTVDLELAALRRRLEELAR	KTFPPTEPKGGGSATSRTLSYYGGGSLFLAFVVFLLGGGSLLYDANYFLGPGPG YYRRATRRIRGGDGKGPGPGLSYYKLGASQRVAGDGPGPGQSINFVRIIMRLWLCGPGPG DELREQETNAALQDVRELLRQQVRQITFLRCLLMGGRLL CRLEELE RRLEELERRLEELERAINTVDLELAALRRRLEELARGGSGDDQIGYYRRA TRRIRGPGPGKEITVATSRTLSYYKGPGPGLVKPSFYVYSRVKNLGPGPGFYSKWYIRVGARKSA
	SAPVb4			EAAAKAKFVAAWTLKAAAVEAAAK GIINTLQKYYCRVRGGRCAVLSCLPKEE QIGKCSTRGRKCCRRKKEAAAKAAYKTFPPTEPKAAYATSRTLSY YAAYLFLAFVVFLLAAYLLYDANYFLAAYYYRRATRRIRGGDGKGPGPG LSYYKLGASQRVAGDGPGPGQSINFVRIIMRLWLCGPGPG DELREQETNAALQDVRELLRQQVRQITFLRCLLMGGRLLCRLEELERRLEEL ERRLEELERAINTVDLELAALRRRLEELARGGSGDDQIGYYRRATRRIRKK KEITVA TSRTLSYYKKKLVKPSFYVYSRVKNLKKFYSKWYIRVGARKSAKKTGALLAAGAAAKK
5	SAPVa5	P6HRC1	Pentameric: COMP (DEMLRELQ ETNAALQDVRELLRQQVRQITFLRCLLM) Linker: GG Trimeric: RLLC RLEELERRLEELERRLEELE RAINTVDLELAALRRRLEELAR	KTFPPTEPKGGGSATSRTLSYYGGGSLFLAFVVFLLGGGSLLYDANYFLGPGPG YYRRATRRIRGGDGKGPGPGLSYYKLGASQRVAGDGPGPG QSINFVRIIMRLWLCGPGPGDEMLRELQETNAALQDVRELLRQQVRQITFLRCLLM GGRLLCRLEELERRLEELERRLEELERAINTVDLELAALRRRLEELAR GGSGDDQIGYYRRATRRIRGPGPGKEITVATSRTLSYYKGPGPG LVKPSFYVYSRVKNLGPGPGFYSKWYIRVGARKSA
	SAPVb5			EAAAKAKFVAAWTLKAAAVEAAAKGIINTLQKYYCRVRGGRCAVLSCLPKEEQIGKC STRGRKCCRRKKEAAAKAAYKTFPPTEPKAAYATSRTLSYYAAYLFLAFVVFLLAAYLLYDANYFLAAY YYRRATRRIRGGDGKGPGPGLSYYKLGASQRVAGDGPGPGQSINFVRIIMRLWLCGPGPG DEMLRELQETNAALQDVRELLRQQVRQITFLRCLLMGGRLLCRLEELERRL EELERRLEELERAINTVDLELAALRRRLEELARGGSG DDQIGYYRRATRRIRKKKEITVATSRTLSYYKKK LVKPSFYVYSRVKNLKKFYSKWYIRVGARKSAKKTGALLAAGAAAKK

Table 3. *Cont.*

Sr No	Name of Vaccine Construct	Name of Self-Assembling Platforms	Component of Monomeric Coiled-Coil Building Blocks with Amino Acid Sequences	Amino Acid Sequence of Vaccine Construct
6	SAPVa6	P4c-Mal SAPN	Pentameric domain: COMP (DEMLRELQ ETNAALQDVRELLRQQVRQITFLRCLLM), Linker: GG, Trimeric domain: de novo designed trimeric coiled coil (RLLCRLEELERRLEELERRLEELE RAINTVDLELAALRRRLEELAR)	KTFPPTEPKGGGSATSRTLSYYGGGSLFLAFVVFLLGGGSLLYDANYFLGPGPG YYRRATRRIRGGDGKGPGPGLSYYKLGASQRVAGDGPGPGQSINFVRIIMRLWLC GPGPGDEMLRELQETNAALQDVRELLRQQVRQITFLRCLLM GGRLLCRLEELERRLEELERRLEELERAINTVDLELAALRRRLEELAR GGSGDDQIGYYRRATRRIRGPGPGKEITVATSRTLSYYKGPGPG LVKPSFYVYSRVKNLGPGPGFYSKWYIRVGARKSA
	SAPVb6			EAAAKAKFVAAWTLKAAAVEAAAKGIINTLQKYYCRVRGGRCAVLSCL PKEEQIGKCSTRGRKCCRRKKEAAAKAAYKTFPPTEPKAAYATSRTLSYY AAYLFLAFVVFLLAAYLLYDANYFLAAYYYRRATRRIRGGDGKGPGPGLSYYKLGASQRVAGD GPGPGQSINFVRIIMRLWLCGPGPGDEMLRELQETNAALQDVR ELLRQQVRQITFLRCLLMGGRLLCRLEELERRLEELERRLEELERAINTVDLEL AALRRRLEELARGGSGDDQIGYYRRATRRIRKKKEITVATSRTLSYYK KKLVKPSFYVYSRVKNLKKFYSKWYIRVGARKSAKKTGALLAAGAAAKK
7	SAPVa7	Mono-M2e	Pentameric domain: COMP (DEMLRELQ ETNAALQDVRELLRQQVRQITFLRCLLM), Linker: GG, Trimeric domain: de novo designed trimeric coiled coil (RLLCRLEELERRLEELERRLEELE RAINTVDLELAALRRRLEELAR)	KTFPPTEPKGGGSATSRTLSYYGGGSLFLAFVVFLLGGGSLLYDANYFL GPGPGYYRRATRRIRGGDGKGPGPGLSYYKLGASQRVAGDGPGPGQSINFVR IIMRLWLCGPGPGDEMLRELQETNAALQDVRELLRQQVRQITFLRCLLMGG RLLCRLEELERRLEELERRLEELERAINTVDLELAALRRRLEELARGGSGDDQI GYYRRATRRIRGPGPGKEITVATSRTLSYYKGPGPG LVKPSFYVYSRVKNLGPGPGFYSKWYIRVGARKSA
	SAPVb7			EAAAKAKFVAAWTLKAAAVEAAAKGIINTLQKYYCRVRGGRCAVLSCLPKEE QIGKCSTRGRKCCRRKKEAAAKAAYKTFPPTEPKAAYATSRTLSY YAAYLFLAFVVFLLAAYLLYDANYFLAAYYYRRATRRIRGGDGKGPGPG LSYYKLGASQRVAGDGPGPGQSINFVRIIMRLWLCGPGPGDEMLREL QETNAALQDVRELLRQQVRQITFLRCLLMGGRLLCRLEELERRLEELERRLEEL ERAINTVDLELAALRRRLEELARGGSGDDQIGYYRRATRRIRKKKEITVATSRT LSYYKKKLVKPSFYVYSRVKNLKKFYSKWYIRVGARKSA KKTGALLAAGAAAKK
8	SAPVa8	PfCSP-KMY SAPN	Pentameric domain: Trp zipper (WQTWNAKWDQWSNDWN AWRSDWQAWKDDWARWRALWM), Linker: GG, Trimeric domain: (RLLLRLEELERRLEELAKFVAAW TLKAAAVDLELAALRRRLEELAR)	KTFPPTEPKGGGSATSRTLSYYGGGSLFLAFVVFLLGGGSLLYDANYFLGPGPG YYRRATRRIRGGDGKGPGPGLSYYKLGASQRVAGDGPGPGQSINFVRIIMRL WLCGPGPGWQTWNAKWDQWSNDWNAWRSDWQAWKDDWARWRALWM GGRLLLRLEELERRLEELAKFVAAWTLKAAAVDLELAALRRRLEELAR GGSGDDQIGYYRRATRRIRGPGPGKEITVATSRTLSYYKGPGPG LVKPSFYVYSRVKNLGPGPGFYSKWYIRVGARKSA
	SAPVb8			EAAAKGIINTLQKYYCRVRGGRCAVLSCLPKEEQIGKCSTRGRKCCRRKK EAAAKAAYKTFPPTEPKAAYATSRTLSYYAAYLFLAFVVFLLAAYLLYDANYFL AAYYYRRATRRIRGGDGKGPGPGLSYYKLGASQRVAGDGPGPGQSINFVRIIMRLWLC GPGPGWQTWNAKWDQWSNDWNAWRSDWQAWKDDWARWRALWM GGRLLLRLEELERRLEELAKFVAAWTLKAAAVDLELAALRRRLEELAR GGSGDDQIGYYRRATRRIRKKKEITVATSRTLSYYKKK LVKPSFYVYSRVKNLKKFYSKWYIRVGARKSAKKTGALLAAGAAAKK

Table 3. *Cont.*

Sr No	Name of Vaccine Construct	Name of Self-Assembling Platforms	Component of Monomeric Coiled-Coil Building Blocks with Amino Acid Sequences	Amino Acid Sequence of Vaccine Construct
9	SAPVa9	MPER-SAPN	Pentameric domain: Tryptophan zipper (RSWQTWNAKWDQWSNDWN AWRSDWQAWKDDWARWRALWMG), Linker: GG, Trimeric domain: Leucine zipper (RLLLRLEELERRLEELERRLEEL ERAINTVDLELAALRRRLEELAR)	KTFPPTEPKGGGSATSRTLSYYGGGSLFLAFVVFLLGGGSLLYDANYFLGPGPG YYRRATRRIRGGDGKGPGPGLSYYKLGASQRVAGDGPGPG QSINFVRIIMRLWLCGPGPGRSWQTWNAKWDQWSNDWNAWRSDWQAWK DDWARWRALWMGGGRLLLRLEELERRLEELERRLEERAINTVDLELAAL RRRLEELARGGSGDDQIGYYRRATRRIRGPGPGKEITVATSRTLSYYK GPGPGLVKPSFYVYSRVKNLGPGPGFYSKWYIRVGARKSA
	SAPVb9			EAAAKAKFVAAWTLKAAAVEAAAKGIINTLQKYYCRVRGGRCAVLSCLPKEE QIGKCSTRGRKCCRRKKEAAAKAAYKTFPPTEPKAAY ATSRTLSYYAAYLFLAFVVFLLAAYLLYDANYFLAAYYYRRATRRIR GGDGKGPGPGLSYYKLGASQRVAGDGPGPGQSINFVRIIMRLWLC GPGPGRSWQTWNAKWDQWSNDWNAWRSDWQAWKDDWARWR ALWMGGGRLLLRLEELERRLEELERRLEELERAINTVDLELAALRRR LEELARGGSGDDQIGYYRRATRRIRKKKEITVATSRTLSYYK KKLVKPSFYVYSRVKNLKKFYSKWYIRVGARKSAKKTGALLAAGAAAKK
10	SAPVa10	$GRA7_{(20–28)}$ SAPN	Pentameric domain: TGSWQTWNARWDQWSNDWN AWRSDWQAWRDDWARWRALW, Linker: GG, Trimeric Domain: GRLLLRLEELERRLEELERRLEELERFVA AWTLRVRALERRLEEL	KTFPPTEPKGGGSATSRTLSYYGGGSLFLAFVVFLLGGGSLLYDANYFLGPGPG YYRRATRRIRGGDGKGPGPGLSYYKLGASQRVAGDGPGPGQSINFVRII MRLWLCGPGPGTGSWQTWNARWDQWSNDWNAWRSDWQA WRDDWARWRALWGGGRLLLRLEELERRLEELERRLEELERFVAAW TLRVRALERRLEELGGSGDDQIGYYRRATRRIRGPGPGKEIT VATSRTLSYYKGPGPGLVKPSFYVYSRVKNLGPGPGFYSKWYIRVGARKSA
	SAPVb10			EAAAKAKFVAAWTLKAAAVEAAAK GIINTLQKYYCRVRGGRCAVLSCLP KEEQIGKCSTRGRKCCRRKKEAAAKAAYKTFPPTEPKAAYATSRTLSY YAAYLFLAFVVFLLAAYLLYDANYFLAAYYYRRATRRIRGGDGKGPGPGLSYYKL GASQRVAGDGPGPGQSINFVRIIMRLWLCGPGPGTGSWQTWNARWDQWSNDWN AWRSDWQAWRDDWARWRALWGGGRLLLRLEELERRLEELERRLEELERFVAAW TLRVRALERRLEELGGSGDDQIGYYRRATRRIRKKKEITVATSRTLSYYKKKLVKPSFYVYSRVKNLKK FYSKWYIRVGARKSAKKTGALLAAGAAAKK
11	SAPVa11	SAPN-Combo	Pentameric domain: W EEWNAKWDEWRNDQNDWRED WQAWRDDWAYWTLTWR Linker: YG Trimeric domain: ELYSRLARIERRVEELRRLLQLIRHEN RMVLQFVRALSMQARRLESKL	KTFPPTEPKGGGSATSRTLSYYGGGSLFLAFVVFLLGGGSLLYDANYFLGPGPG YYRRATRRIRGGDGKGPGPGLSYYKLGASQRVAGDGPGPGQSINFVRIIMRLWLCGPGPG WEEWNAKWDEWRNDQNDWREDWQAWRDDWAYWTLTWRYGELYSRLARI ERRVEELRRLLQLIRHERMVLQFVRALSMQARRLESKLGGSGDDQIGYYRRA TRRIRGPGPGKEITVATSRTLSYYKGPGPGLVKP SFYVYSRVKNLGPGPGFYSKWYIRVGARKSA
	SAPVb11			EAAAKAKFVAAWTLKAAAVEAAAK GIINTLQKYYCRVRGGRCAVLSCLP KEEQIGKCSTRGRKCCRRKKEAAAKAAYKTFPPTEPKAAYATSRTLSY YAAYLFLAFVVFLLAAYLLYDANYFLAAYYYRRATRRIRGGDGKGPGPGLSYYKL GASQRVAGDGPGPGQSINFVRIIMRLWLCGPGPGWEEWNAKWDEWRNDQNDWRED WQAWRDDWAYWTLTWRYGELYSRLARIERRVEELRRLLQLIRHENRMVLQFVRALS MQARRLESKLGGSGDDQIGYYRRATRRIRKKKEITVATSRTLSYYKKK LVKPSFYVYSRVKNLKKFYSKWYIRVGARKSAKKTGALLAAGAAAKK

Table 3. *Cont.*

Sr No	Name of Vaccine Construct	Name of Self-Assembling Platforms	Component of Monomeric Coiled-Coil Building Blocks with Amino Acid Sequences	Amino Acid Sequence of Vaccine Construct
12	SAPVa12	PfCSP -SAPN	Pentamer domain: Trp zipper (WKWDG GLVPRGSWQTWNAKWDQWSNDWN-AWRSDWQAWKDDWARWRALWM), Linker: GG, Trimeric domain: (RLLLRLEELERRLEELAK FVAAW-TLKAAAVDLELAALRRRLEELAR)	KTFPPTEPKGGGSATSRTLSYYGGGSLFLAFVVFLLGGGSLLYDANYFLGPGPG YYRRATRRIRGGDGKGPGPGLSYYKLGASQRVAGDGPGPGQSINFVRIIMRL WLCGPGPGWKWDGGLVPRGSWQTWNAKWDQWSNDWNAWRSDWQAW KDDWARWRALWMGGRLLLRLEELERRLEELAKFVAAWTLKAAAV DLELAALRRRLEELARGGSGDDQIGYYRRATRRIRGPGPGKEIT VATSRTLSYYKGPGPGLVKPSFYVYSRVKNLGPGPGFYSKWYIRVGARKSA
	SAPVb12			EAAAKGIINTLQKYYCRVRGGRCAVLSCLPKEEQIGKCSTRGRK CCRRKKEAAAKAAYKTFPPTEPKAAYATSRTLSYYAAYLFLAFVVFLLAAYL LYDANYFLAAYYYRRATRRIRGGDGKGPGPGLSYYKLGASQRVAGDGPGPGQSINFV RIIMRLWLCGPGPGWKWDGGLVPRGSWQTWNAKWDQWSNDWN AWRSDWQAWKDDWARWRALWMGGRLLLRLEELERRLEELAKFVAAW TLKAAAVDLELAALRRRLEELARGGSGDDQIGYYRRATRRIRKKKEITVATSRTLSYYK KKLVKPSFYVYSRVKNL KKFYSKWYIRVGARKSAKKTGALLAAGAAAKK

Table 4. Details of structural assessment parameters for SANV constructs (SANVa and SANVb) before and after refinement, based on models generated by GalaxyTBM and AlphaFold3. For each construct, the best-refined model was determined by the minimum MolProbity score.

Type of SANV Construct	Name of Vaccine Construct	Model Scores Prior to Structural Refinement			Scores of Models After Structural Refinement						Predicted TM-(pTM) Score of AlphaFold3 Model
		Model No.	ERRAT Score	Ramachandran Plot Favoured Regions (%)	Model No	GDT-HA	RMSD	MolProbity	Clash Score	Poor Rotamers	Rama Favoured (%)	
SANVa	SANVa1	MODEL 3	87.7953	84.70	MODEL 4	0.9883	0.304	2.042	11.7	0.5	92.7	0.26
	SANVa2	MODEL 4	84.1216	92.20	MODEL 2	0.9944	0.254	1.831	8.1	0.8	94.2	0.23
	SANVa3	MODEL 5	84.4358	97.10	MODEL 5	0.9926	0.252	1.79	11.6	0	96.7	0.26
	SANVa4	MODEL 2	90.6504	84.00%	MODEL 1	0.9873	0.271	1.942	10.7	0	94.1	0.24
	SANVa5	MODEL 3	76.2097	84.70	MODEL 4	0.9865	0.284	1.963	10.4	0	93.5	0.27
	SANVa6	MODEL 2	83.7838	81.40	MODEL 4	0.9847	0.285	1.996	9.7	0.5	92	0.26
	SANVa7	MODEL 2	83.004	86.00	MODEL 1	0.9919	0.276	1.997	12.4	0	94.2	0.26
	SANVa8	MODEL 3	94.8148	98.10	MODEL 5	0.991	0.281	1.43	7.1	0	97.8	0.28
	SANVa9	MODEL 3	91.6996	93.60	MODEL 2	0.9982	0.237	1.663	7.2	0	96.1	0.22
	SANVa10	MODEL 2	99.6296	98.10	MODEL 5	0.9973	0.227	1.428	5.9	0.9	97.5	0.28
	SANVa11	MODEL 5	88.7597	95.90	MODEL 4	0.991	0.242	1.649	8.2	0.9	96.8	0.29
	SANVa12	MODEL 2	89.8182	96.90	MODEL 5	0.9948	0.222	1.612	7	0.5	96.5	0.27

Table 4. *Cont.*

Type of SANV Construct	Name of Vaccine Construct	Model Scores Prior to Structural Refinement			Scores of Models After Structural Refinement						Predicted TM-(pTM) Score of AlphaFold3 Model
		Model No.	ERRAT Score	Ramachandran Plot Favoured Regions (%)	Model No	GDT-HA	RMSD	MolProbity	Clash Score	Poor Rotamers	Rama Favoured (%)	
SANVb	SANVb1	MODEL 4	84.4068	89.80	MODEL 4	0.9775	0.325	1.685	7.5	0.4	96	0.24
	SANVb2	MODEL 3	86.3095	91.80	MODEL 1	0.9897	0.265	1.524	7.5	0.7	97.4	0.21
	SANVb3	MODEL 5	94.822	95.10	MODEL 5	0.9936	0.263	1.287	5.3	0.7	98	0.22
	SANVb4	MODEL 5	88.1757	93.90	MODEL 3	0.988	0.283	1.696	8.2	0.7	96.3	0.23
	SANVb5	MODEL 2	91.7933	94.30	MODEL 2	0.9866	0.293	1.36	6.5	0.4	98.3	0.24
	SANVb6	MODEL 2	95.5696	95.50	MODEL 2	0.9887	0.279	1.252	4.8	0	98	0.22
	SANVb7	MODEL 5	94.3218	94.90	MODEL 1	0.9894	0.279	1.428	6.7	0.4	97.7	0.21
	SANVb8	MODEL 3	94.704	96.50	MODEL 1	0.9951	0.246	1.33	6	0	98.3	0.26
	SANVb9	MODEL 5	93.4169	92.10	MODEL 5	0.9798	0.331	1.442	4.6	1.1	96.9	0.24
	SANVb10	MODEL 1	92.1875	94.60	MODEL 4	0.9916	0.259	1.426	7.8	0.4	98.3	0.22
	SANVb11	MODEL 2	78.7692	88.70	MODEL 3	0.9791	0.316	1.983	11.8	0.7	94.1	0.22
	SANVb12	MODEL 1	94.6032	93.10	MODEL 5	0.9864	0.289	1.53	6.1	0.4	96.8	0.25

Table 5. Details of homo-oligomer modeled structures of SANVa and SANVb constructs predicted by GalaxyHomomer (12-mer) and AlphaFold3. The best models for each construct were selected based on superior interface area (model 5 of SANVa9 and model 3 of SANVb6).

Name of Vaccine Construct	GalaxyHomomer			AlphaFold3	
	Model No.	Interface Area	Docking Score	ipTM Score	Number of Multimers
SANVa1	MODEL 3	37,285.5	670.11	0.29	18 mer
SANVa2	MODEL 2	127,020.5	812.07	0.28	16 mer
SANVa3	MODEL 2	114,694.6	802.02	0.27	18 mer
SANVa4	MODEL 2	16,143.7	906.936	0.28	18 mer
SANVa5	MODEL 1	17,503.5	859.471	0.28	18 mer
SANVa6	MODEL 5	128,394.9	701.313	0.28	18 mer
SANVa7	MODEL 1	27,890.7	1188.802	0.28	18 mer

Table 5. *Cont.*

Name of Vaccine Construct	GalaxyHomomer			AlphaFold3	
	Model No.	Interface Area	Docking Score	ipTM Score	Number of Multimers
SANVa8	MODEL 1	27,743.2	1058.661	0.28	18 mer
SANVa9	MODEL 5	143,430	797.116	0.27	17 mer
SANVa10	MODEL 1	22,889.6	1124.27	0.28	18 mer
SANVa11	MODEL 2	17,113.3	834.327	0.28	17 mer
SANVa12	MODEL 2	136,391	1026.88	0.28	17 mer
SANVb1	MODEL 1	175,520.7	840.88	0.27	14 mer
SANVb2	MODEL 1	180,694.2	933.204	0.27	12 mer
SANVb3	MODEL 3	186,138.5	670.084	0.28	14 mer
SANVb4	MODEL 1	179,193.8	676.86	0.28	14 mer
SANVb5	MODEL 3	185,002.5	747.449	0.28	14 mer
SANVb6	MODEL 3	194,416.7	768.058	0.28	14 mer
SANVb7	MODEL 5	184,567	674.191	0.28	14 mer
SANVb8	MODEL 1	191,609	908.349	0.28	15 mer
SANVb9	MODEL 3	188,459	807.8	0.26	12 mer
SANVb10	MODEL 4	173,344	755.35	0.28	14 mer
SANVb11	MODEL 5	151,534	636.465	0.27	13 mer
SANVb12	MODEL 1	174,385	952.562	0.27	14 mer

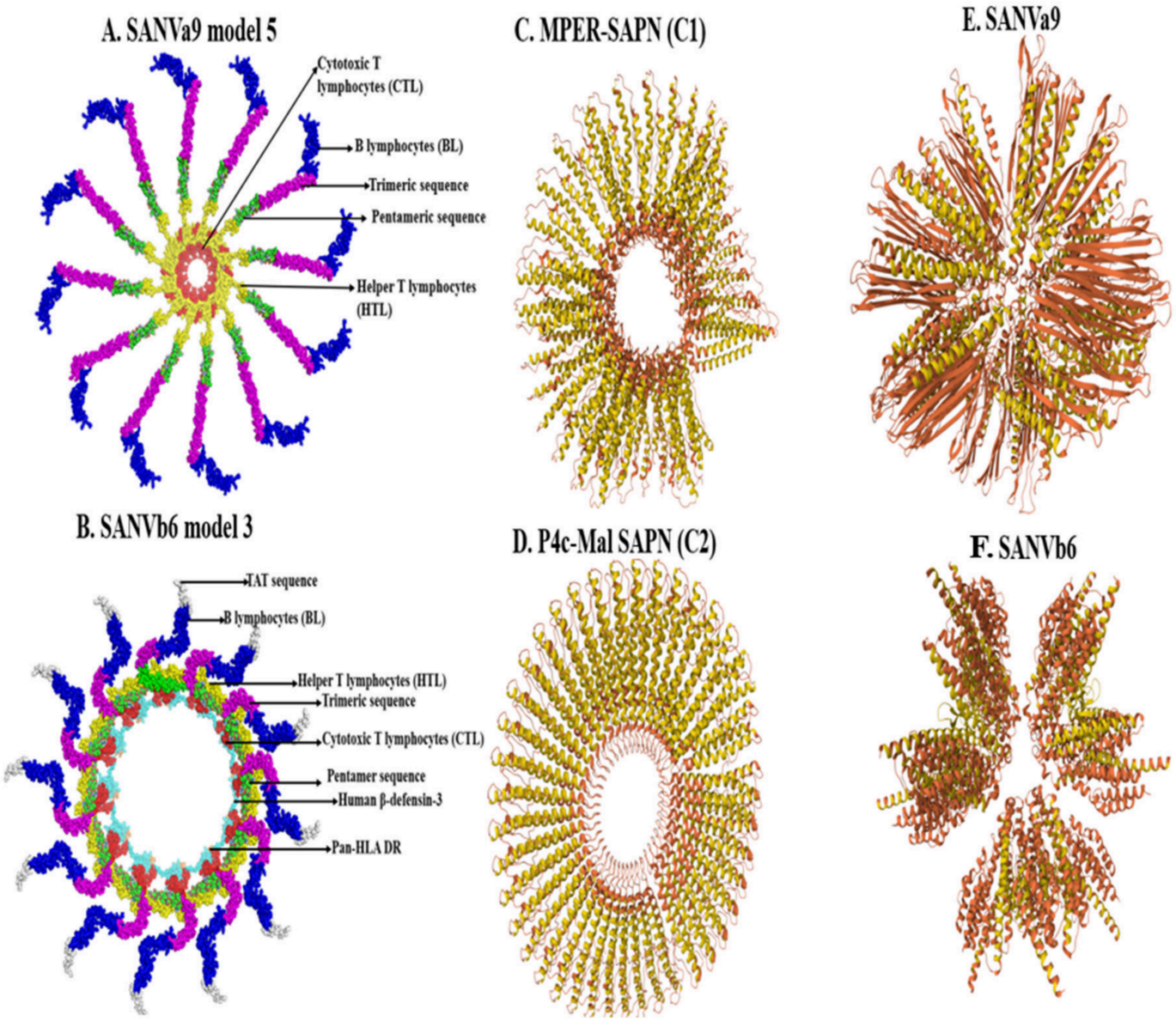


Figure 4. The predicted 3D structures show the formation of homo-oligomeric as well as multimeric assemblies in the selected SANV constructs. (**A**) Homo-oligomeric 12-mer assembly of SANVa9, displaying B-cell epitopes (blue), HTL epitopes (yellow), CTL epitopes (red), pentameric sequences (green), and trimeric sequences (pink). (**B**) Homo-oligomeric 12-mer assembly of SANVb6, showing B-cell epitopes (blue), HTL epitopes (yellow), CTL epitopes (red), pentameric sequences (green), trimeric sequences (pink), along with TAT sequence (white), PADRE (sky blue), and an adjuvant segment (orange). (**C**) Multimeric MPER-SAPN model comprising 38 identical chains. (**D**) P4c-Mal SAPN multimeric assembly made up of 42 chains. (**E**,**F**) indicate multimeric models of SANVa9 and SANVb6, consisting of 17 and 14 chains, respectively.

3.7. Characterization of SANVa9 and SANVb6 Construct Identified Through Screening

3.7.1. Analysis of Physicochemical Properties, Antigenicity, Allergenicity, Solubility, and Antioxidant Activity

Assessment of physicochemical properties is crucial to ensure the safety and effectiveness of vaccine candidates. In this study, various chemical and physical characteristics of SANVa9 and SANVb6 were analyzed using the ExPASy ProtParam tool. The molecular weights of SANVa9 and SANVb6 were found to be 31.56 kDa and 40.08 kDa, respectively. Their isoelectric points (pI) were 10.22 and 10.13, indicating that both constructs are positively charged, which may contribute to their stability and immunogenic potential.

Since vaccine candidates with molecular weights under 110 kDa are generally considered suitable [109], both constructs meet this criterion. The GRAVY (Grand Average of Hydropathicity) scores for SANVa9 (−0.603) and SANVb6 (−0.354) were negative, reflecting their hydrophilic nature, which favors solubility [110]. The aliphatic indices of 71.21 for SANVa9 and 87.01 for SANVb6 indicate good thermostability; thus, enhanced thermal resistance is generally correlated with higher aliphatic indices [111]. Additionally, the ESM-IF generative artificial intelligence model, recommended by Cagiada et al. [56] revealed thermodynamic stability (ΔG in kcal/mol) for the SANVa9 (7.11) and SANVb6 (8.67). The thermodynamic free energy of unfolding is reported by this model as ΔG positive values signify a stable protein, as in the benchmark dataset of experimental ΔG values for stable proteins, which range from 1 to 12. The predicted half-lives of both constructs were approximately 30 h in mammalian reticulocytes (in vitro), over 20 h in yeast (in vivo), and more than 10 h in *E. coli* (in vivo), suggesting that these constructs are stable in various in vivo systems. Antigenicity predictions showed that SANVa9 and SANVb6 are likely to elicit immune responses, with scores of VaxiJen v2.0 (0.7463 and 0.6668) and ANTIGENPro (0.724909 and 0.253995), respectively. The allergenicity evaluations using AllergenFP and AllerTOP indicated that both constructs are non-allergenic, suggesting a reduced risk of allergic reactions upon administration. Solubility predictions from the SOLpro server yielded high scores of 0.945926 for SANVa9 and 0.870418 for SANVb6, both exceeding the 0.5 threshold, indicating good solubility. Furthermore, antioxidant activity analysis using the AnOxPePred tool revealed that both constructs (SANVa9 and SANVb6) contain peptides with notable free radical scavenging (FRS) activity, scoring 0.6975 and 0.6941, respectively. These peptides could mitigate oxidative stress by neutralizing reactive oxygen species, a property beneficial for therapeutic applications [112]. Additionally, the absence of transmembrane domains in SANVa9 and SANVb6 suggests minimal complications for high-throughput production, while the lack of signal peptides suggests restricted protein secretion or localization [113].

3.7.2. Identification and Analysis of Conformational B-Cell Epitopes Within SANV Constructs

The DiscoTope predicts confirmational B-cell epitope residues on the surface of a protein's tertiary structure capable of inducing humoral immune responses [57]. Based on DiscoTope analysis, 183 conformational B-cell epitope residues were identified in SANVa9, corresponding to positions 1–9, 54, 63, 67–69, 79–81, 84–105, 106, 108–153, 155, 170–177, and 194–281 above a threshold score of −3.7. Similarly, 165 conformational B-cell epitope residues were predicted in SANVb6 at positions 73–86, 126–178, 180, 182–196, 197–198, 199–202, 204–205, 242–243, 246, 266–282, and 283–336, as illustrated in Figures 5 and S1. Moreover, selected linear BL epitopes (BL1: 81–95, BL2: 166–180, BL3: 51–65, BL4: 41–55) fall within or overlap with conformational epitope residues (54, 63, 79–81, 84–105, 170–177) of SANVa9 and residues (41–55) of SANVb6 created by protein fusion. Thus, antibodies produced against these conformational epitopes probably recognize the linear B cell epitopes. Additionally, the vaccine-elicited antibodies may bind to the original SARS-CoV-2 antigens, as they share conformational epitope residues in the N (79–82) and E (67–75) proteins, though the vaccine antigen is structurally dissimilar. Additionally, although ORF8 proteins are not present in intact virions, they are thought to be secreted from the infected host cell [114,115]. Moreover, antibodies against ORF8 are commonly detected in patients and are considered reliable markers of SARS-CoV-2 infection [116]. Thus, the vaccine-induced antibodies against BL4 epitopes of ORF8 are likely to recognize the secreted ORF8 antigen during SARS-CoV-2 infection.

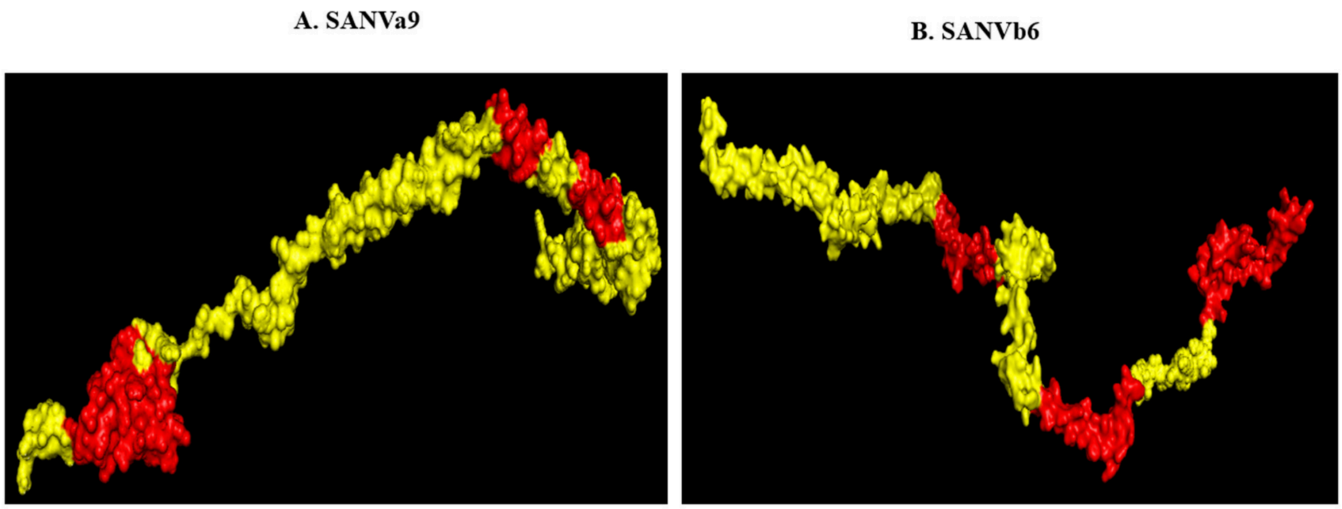


Figure 5. Three-dimensional structural depiction of SANVa9 (**A**) and SANVb6 (**B**) constructs. Discontinuous B-cell epitopes predicted by the DiscoTope tool are displayed, with the epitope residues' side chains indicated in yellow. Red color indicates non-discontinuous B-cell epitopes.

3.7.3. Molecular Docking Analysis of SANVa9 and SANVb6 Constructs with SARS-CoV-2 Antibodies

Antigen–antibody interactions have a vital role in the humoral immunological response, facilitating the effective clearance of pathogens. Over the past two decades, antibodies have been extensively applied in therapeutic settings due to their exceptional antigen-binding affinity and specificity [117,118]. Among notable sarbecovirus antibodies, 5817 exhibits broad neutralizing activity against various SARS-CoV-2 VOCs and related bat and pangolin coronaviruses. In vivo studies have demonstrated that monoclonal antibody 5817 provides strong protective effects against SARS-CoV infections in mice [58]. To evaluate the shape complementarity and binding interactions within the 5817 antibodies and the developed SANV constructs (SANVa9 and SANVb6), a global protein-protein docking method was used with the ClusPro web server. The energy scores for docking of SANVb6 (−398.7 kcal/mol) and SANVa9 (−339.7 kcal/mol) exhibited significantly stronger binding interactions/affinities compared to the positive control peptide C3 (−229.5 kcal/mol).

In addition to ClusPro, AlphaFold3 was used to predict Ab-Ag interaction using ipTM scores for the control C3 (0.44), SANVa9 (0.35), and SANVb6 (0.34) (Figure S3). However, ipTM < 0.6 indicates the docking interface is unreliable. AlphaFold3 might have remarkable accuracy in modeling general protein–protein interactions; its performance is comparatively reduced for antibody–antigen complexes, largely because these interactions lack strong co-evolutionary constraints [119,120]. A recent study by Hitawala et al. [121] reported only 10.2% success with antibodies and 13.3% with nanobodies in high-accuracy docking, underscoring the difficulty of modeling flexible complementarity-determining regions with AlphaFold3. Moreover, the widely used ClusPro server for protein-protein docking relies on physics-based scoring functions (van der Waals interactions, electrostatics, and desolvation energy) rather than evolutionary data and is reported as one of the top-performing servers for antibody–antigen docking [122]. It explores multiple binding poses and ranks them by energetic favorability to identify plausible docking solutions even in a highly flexible system. Moreover, the ClusPro AbEMap module enables epitope mapping directly from antibody sequence data, enhancing its relevance for therapeutic antibody discovery and design [123]. Thus, AlphaFold might provide an excellent starting point for generating high-confidence structural models of antibodies and antigens, and ClusPro complements it by simulating binding interactions between them more realistically [124]. Intra-protein interactions in macromolecular complexes are not the same as interactions among protein surfaces.

Within individual proteins, hydrogen bonds significantly contribute to structural stability, while salt bridges play a crucial role in maintaining the folding and stability of α-helical structures [125–127]. Protein–protein interactions are stabilized by both hydrogen bonds and ionic bonds, also called salt bridges. Salt bridges involve two types of intermolecular forces: hydrogen bonding and ionic interactions. Their stability is further improved when hydrogen bonds are complementary to the electrostatic (Coulombic) attraction between oppositely charged residues [128,129]. The PDBSum analysis of interacting residues in the antigen-antibody using ClusPro-generated docking complexes of the 5817 antibody (heavy and light chains) with C3, SANVa9, and SANVb6 is illustrated in Figure 6A–C and S2. Salt bridge analysis reveals that SANVb6 exhibits the most substantial interaction with the 5817 antibody, surpassing both SANVa9 and C3. Specifically, in the C3 complex, only two salt bridges are observed with the heavy chain, while no such interactions occur with the light chain. It further forms 13 hydrogen bonds, including 4 with the heavy chain and 9 with the light chain, as well as 38 and 49 non-bonded contacts with the heavy and light chains, respectively. In contrast, SANVa9 demonstrates a higher degree of interaction, establishing four salt bridges (one with the heavy chain and three with the light chain), 21 hydrogen bonds (6 involving the heavy chain and 15 with the light chain), and 35 and 119 non-bonded contacts with the heavy and light chains, respectively, reflecting stronger binding stability. For SANVb6, five salt bridges are detected exclusively with the heavy chain, accompanied by 14 hydrogen bonds (11 with the heavy chain and 3 with the light chain), as well as 108 and 40 non-bonded contacts with the heavy and light chains, respectively (Figure 6D–F).

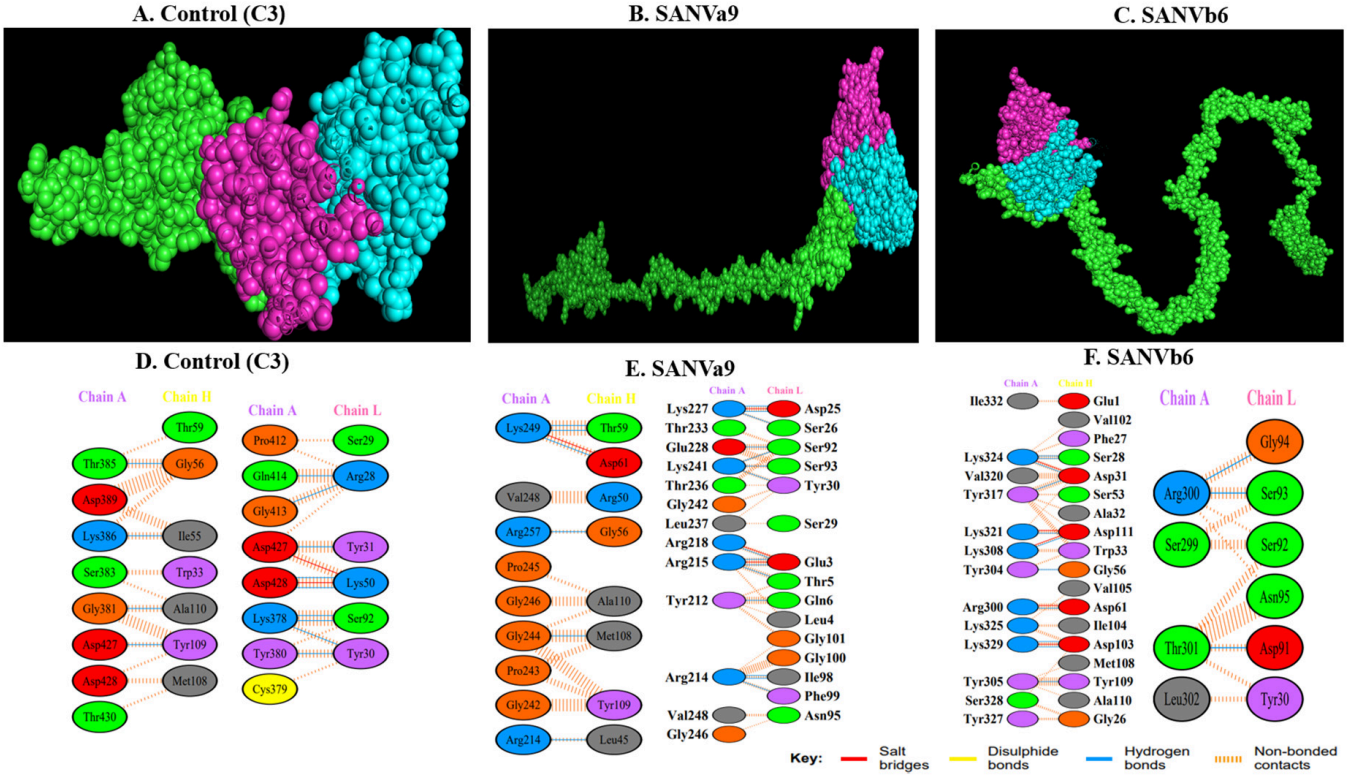


Figure 6. Three-dimensional depiction of docking models (**A**–**C**) along with residue-level interactions between the SANV constructs and the antibody (**D**–**F**). Docked complexes of the 5817 antibody with (**A**) Control (C3), (**B**) SANVa9, and (**C**) SANVb6. The control and SANV constructs are shown in green, while the antibody heavy chain (sky blue) and light chain (magenta) are distinctly represented. The interaction interface within chain A of C3 and the heavy and light chains of the 5817 antibody is shown in (**D**), while the residue-level interactions of chain A of SANVa9 with the antibody are presented in (**E**), and the residue-level interactions of chain A of SANVb6 with the antibody are illustrated in (**F**).

To verify whether the binding residues are associated with discontinuous B-cell epitopes, the PDBSum interaction data were cross-checked with the DiscoTope predictions for SANVa9 and SANVb6. In SANVa9 (chain A), the residues Arg214, Gly242, Pro243, Gly244, Pro245, Gly246, Val248, Lys249, and Arg251 were identified as discontinuous epitopes that also bind to the heavy chain of the 5817 antibody, confirming their role in binding. Furthermore, additional residues Lys227, Thr233, Glu228, Lys241, Thr236, Gly242, Leu237, Arg218, Arg215, Tyr212, Arg214, Val248, and Gly246 were found to bind to the light chain, reinforcing the strong binding interaction of SANVa9 (Figure 6E). Similarly, every discontinuous epitope residue from chain A of SANVb6, including Ile332, Lys324, Val320, Tyr317, Lys321, Lys308, Tyr304, Arg300, Lys325, Lys329, Tyr305, Ser328, and Tyr327, was found to interact with the heavy chain of the 5817 antibody. Additionally, residues Arg300, Ser299, Thr301, and Leu302 from chain A interacted with the light chain (Figure 6F). These observations indicate extensive interaction between epitopes of SANVa9 and SANVb6 with both chains of the 5817 antibody. Furthermore, binding affinity predictions of antigen–antibody complex using the AREA-AFFINITY tool yielded identical log(K) values of −8.5322 for SANVa9, SANVb6, and C3. Similarly, the experimental binding energies (ΔG) were estimated to be −11.637 kcal/mol for all three peptides. Despite equivalent log(K) and ΔG values, the substantially lower docking energies of SANVa9 and SANVb6 suggest stronger, more favorable binding interactions than those of the control. This observed inconsistency between the docking energy calculated from ClusPro and the binding affinity predicted by AREA-AFFINITY stems from the distinct computational principles underlying these methods. ClusPro is a rigid-body docking method that attempts to find the structure of the protein-protein complex at the minimum of the Gibbs free energy by sampling billions of conformations through the PIPER algorithm, which does not intend to estimate the true interaction energy. In contrast, AREA-AFFINITY considers the roles of interface and surface areas in predicting the binding affinity of protein-protein complexes by using areas classified by amino acid type and biophysical nature [59,130]. Moreover, lower energy in molecular docking is not always equivalent to higher binding affinity. Enthalpy (captured by the docking energy) and entropy both determine the Gibbs free energy. If the lower-energy pose rigidifies the binding site, the favorable energy drop might be offset by an entropic penalty, yielding the same net binding affinity [131]. Therefore, the ClusPro docking energy should not be considered as a measure of binding affinity [132]. These findings highlight the enhanced binding potential of SANVb6 and SANVa9, supporting their consideration in future antibody-based therapeutic/diagnostic strategies. Although molecular docking is a commonly used approach for predicting antibody–antigen interactions, it requires substantial computing resources and is time-consuming, particularly when dealing with flexible molecules such as antibodies [133]. To address this, the current study employed AbAgIntPre, a deep learning-based tool that enables rapid screening of antibodies capable of binding to target antigens. Using this method, interaction scores were determined between SANV constructs (SANVa9 and SANVb6) and several other SARS-CoV-2-specific antibodies. The respective interaction scores for SANVa9 and SANVb6 were as follows: 5817 (0.805, 0.785), K501SP6 (0.78, 0.78), CB6 (0.765, 0.78), CR3022 (0.785, 0.77), S309 (0.817, 0.817), 5–7 (0.745, 0.75), 76E1 (0.74, 0.735) and S2P6 (0.813, 0.802) LY-CoV555 (0.75, 0.795). The resulting data demonstrate that all evaluated antibodies exhibit binding affinity toward the designed SANV constructs.

3.8. Assessment of Docking Interactions Between TLR and SANVa9/SANVb6

To assess the binding specificity potential of the designed SANV constructs (SANVa9 and SANVb6) with TLR2, TLR3, and TLR7, molecular docking analyses were performed and benchmarked against respective control ligands. In most cases, docking

scores indicated comparatively stronger interactions between SANV constructs and the TLRs than those observed with the controls. SANVa9 and SANVb6 showed respective docking scores of −1256.6 kcal/mol and −1213.8 kcal/mol with TLR2, surpassing the control C4 (−1017.2 kcal/mol). For TLR3, SANVa9 (−1552.2 kcal/mol) exhibited a slightly stronger binding than the control C5 (−1542.1 kcal/mol), whereas SANVb6 (−1356.6 kcal/mol) showed a weaker interaction. Similarly, SANVa9 (−1516 kcal/mol) and SANVb6 (−1433.8 kcal/mol) demonstrated stronger binding with TLR7 than the control C6 (−1373.3 kcal/mol). Furthermore, the Gibbs free energy (ΔG) evaluations with the PRODIGY server are essential for assessing whether an interaction is likely to occur under specific cellular conditions. SANVb6 displayed the better binding affinity (lowest ΔG) with TLR2 (−13.6 kcal/mol) than C4 (−12.0 kcal/mol) and SANVa9 (−11.1 kcal/mol). For TLR3, SANVb6 again showed a stronger interaction (−16.6 kcal/mol) compared to SANVa9 (−12.0 kcal/mol) and the control (−12.0 kcal/mol). In the case of TLR7, SANVa9 exhibited the most favorable ΔG (−15.4 kcal/mol), followed by SANVb6 (−12.4 kcal/mol) and control C6 (−10.6 kcal/mol).

Moreover, to obtain deeper insights into the residue-level interactions between the docked SANV constructs, control molecules, and the TLR, the PDBSum database was employed. This tool provides detailed information on key interactions, including hydrogen bonds, hydrophobic contacts, and electrostatic forces between the TLR receptors and their ligands. The results of the docked complexes of TLR2 between C4, SANVa9, and SANVb6 are illustrated in Figure 7A–C, TLR3 with C5, SANVa9, and SANVb6 in Figure 8A–C and TLR7 with C6, SANVa9, and SANVb6 in Figure 9A–C. These interactions are crucial for determining each ligand's capacity to induce an immunological response by evaluating how well it binds to and stabilizes the TLR–ligand complex. For TLR2, SANVa9 formed the highest number of salt bridges (4), hydrogen bonds (12), and non-bonded contacts (189), indicating the most stable complex, followed by SANVb6 (2 salt bridges, 13 H-bonds, 222 contacts) and the control C4 (1 salt bridge, 7 H-bonds, 132 contacts) (Figure 7D–F). In contrast, for TLR3, the control C5 formed the strongest electrostatic interaction (3 salt bridges), although SANVb6 exhibited higher numbers of hydrogen bonds (13) and non-bonded contacts (234). SANVa9 showed weaker interaction (1 salt bridge, 4 H-bonds, 153 contacts) (Figure 8D–F). For TLR7, SANVa9 showed the most stable and extensive interaction profile, including 8 salt bridges, 17 H-bonds, 257 contacts, significantly surpassing SANVb6 and the control C6, which lacked any salt bridges (Figure 9D–F). These results highlight the high binding potential of SANVb6 with TLR2 and TLR3, and of SANVa9 with TLR7, suggesting their promising immunostimulatory capabilities for vaccine design. Moreover, the results of the AlphaFold3 webserver used for docking of different protein–protein interactions revealed the interface predicted template modeling (ipTM) score high for SANVb6-TLR2 (0.21) and SANVa9-TLR3 (0.16) (Table 6, Figure S4). The ipTM score assesses the interface reliability of the modeled molecular complexes and evaluates the correctness of inter-subunit orientations. The TLRs complexes with controls (C4, C5, and C6) showed moderate reliability of the docking interfaces, as indicated by ipTM scores near 0.8. However, unreliable docking interfaces were obtained for the vaccine constructs (SANVa9 and APVb6), with ipTM scores < 0.6, suggesting unreliable or failed interface prediction [93]. In this case, AlphaFold3 was found to exhibit significant limitations in accurately predicting the structures of terminal tags when placed in the context of chimeric or membrane-associated proteins, as these disrupt the evolutionary signals revealed by multiple sequence alignments [94,134]. Therefore, based on comparisons with the ClusPro docking scores, the molecular complexes SANVa9–TLR3 and SANVb6-TLR7, representing each type of the SANVa and SANVb constructs, were selected for further MD simulation studies (Table 6).

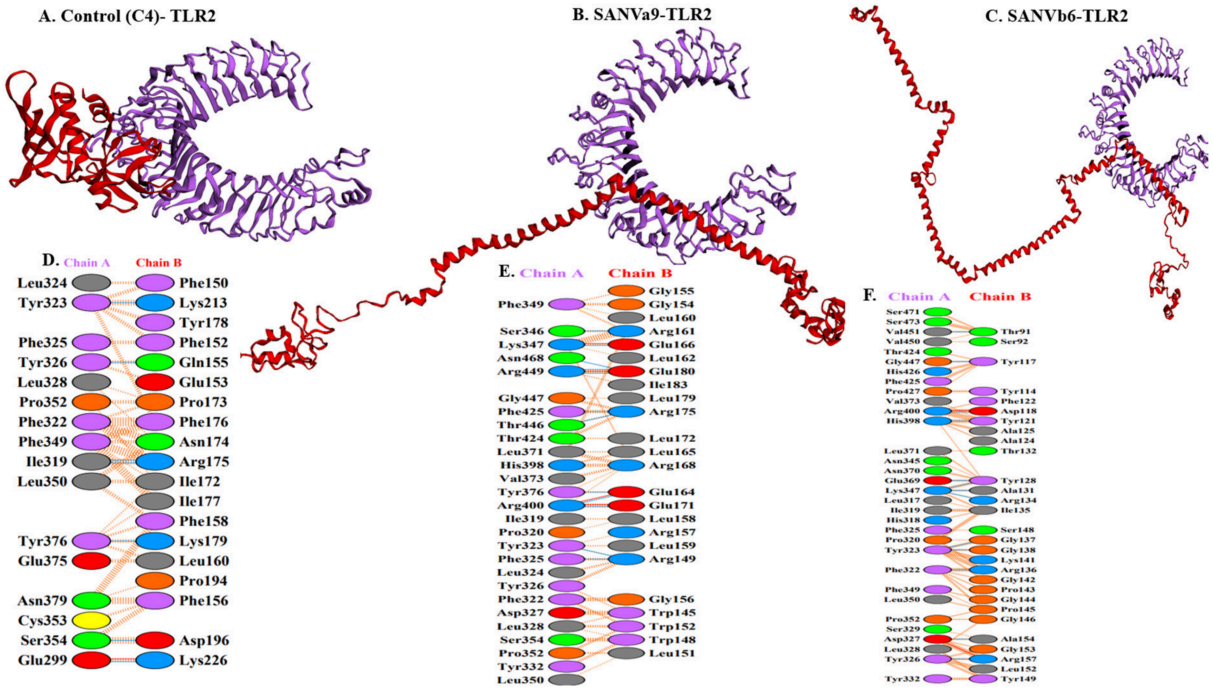


Figure 7. Schematic representation of PDBSum-based interactions between the human TLR2 receptor and the control (C4) as well as SANV constructs (SANVa9 and SANVb6). The docked complexes of TLR2 between C4, SANVa9, and SANVb6, respectively, are shown in cartoon format (**A**–**C**). Illustrate the residue-level interactions within chain A of TLR2 and chain B of C4, SANVa9, and SANVb6, respectively (**D**–**F**). Amino acid residues are color-coded based on their chemical properties: red for negatively charged, blue for positively charged, green for neutral, purple for aromatic, orange for proline and glycine, yellow for cysteine, and grey for aliphatic residues.

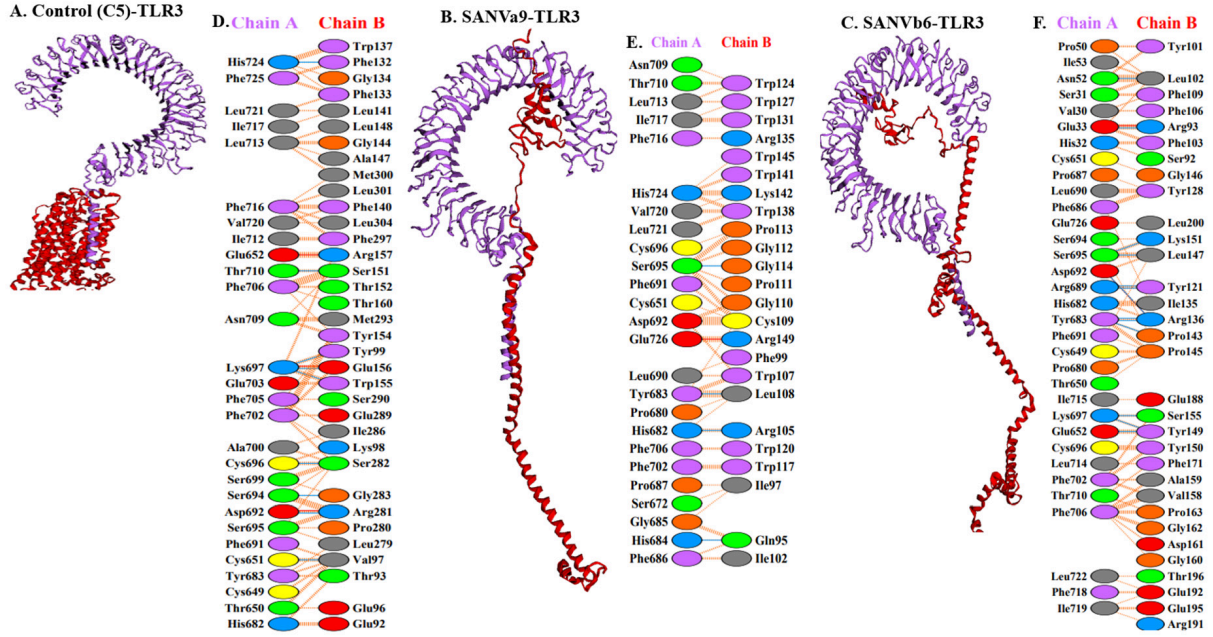


Figure 8. Schematic representation of PDBSum-based interactions between the human TLR3 receptor and the control (C5) as well as SANV constructs (SANVa9 and SANVb6). The docked complexes of TLR3 with C5, SANVa9, and SANVb6, respectively, are shown in cartoon format (**A**–**C**). Illustrating the residue-level interactions within chain A of TLR3 and chain B of C5, SANVa9, and SANVb6, respectively (**D**–**F**). Amino acid residues are color-coded based on their chemical properties: red for negatively charged, blue for positively charged, green for neutral, purple for aromatic, orange for proline and glycine, yellow for cysteine, and grey for aliphatic residues.

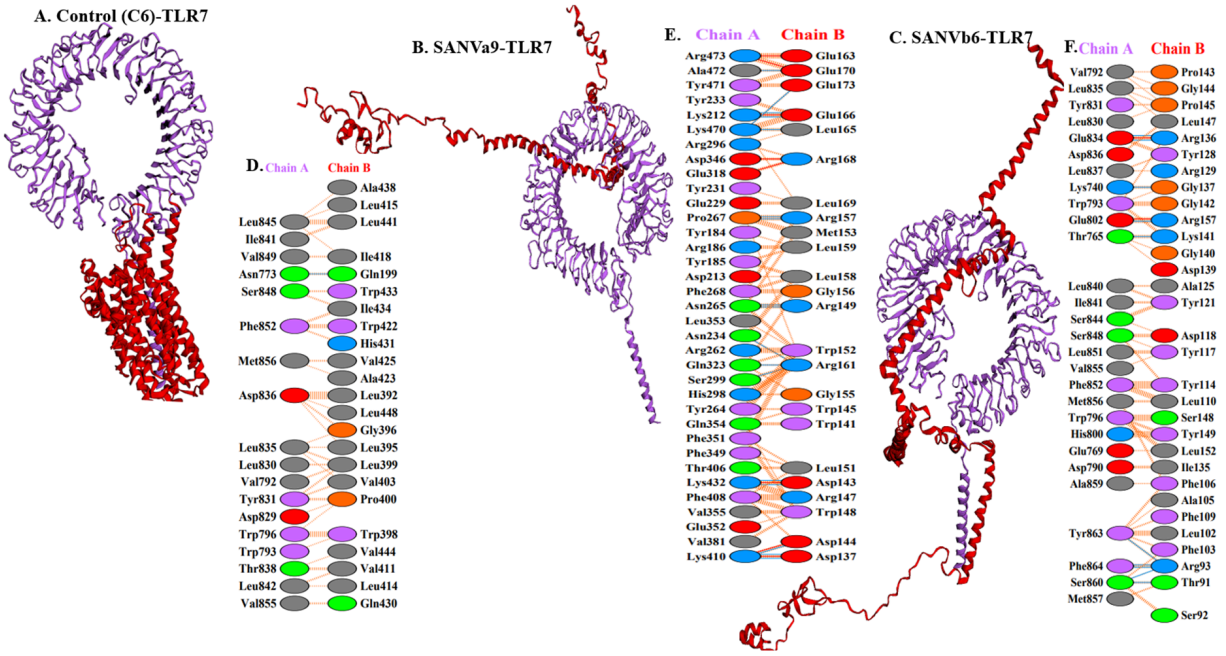


Figure 9. Schematic representation of PDBSum-based interactions between the human TLR7 receptor and the control (C6) as well as SANV constructs (SANVa9 and SANVb6). The docked complexes of TLR7 with C4, SANVa9, and SANVb6, respectively, are shown in cartoon format (**A**–**C**). Illustrating the residue-level interactions within chain A of TLR2 and chain B of C6, SANVa9, and SANVb6, respectively (**D**–**F**). Amino acid residues are color-coded based on their chemical properties: red for negatively charged, blue for positively charged, green for neutral, purple for aromatic, orange for proline and glycine, yellow for cysteine, and grey for aliphatic residues.

Table 6. Molecular docking energy scores of ligands (C4, C5, C6, SANVa9, and SANVb6) with receptors (TLR-2, TLR-3, and TLR-7) generated using the ClusPro and AlphaFold3 web servers.

S. No.	Molecular Complex	ClusPro Docking Score (kcal mol^{-1})	AlphaFold3 ipTM Scores
1	C4-TLR2	−1017.2	0.82
	SANVa9-TLR2	−1256.6	0.13
	SANVb6-TLR2	−1213.8	0.21
2	C5-TLR3	−1542.1	0.76
	SANVa9-TLR3	−1552.2	0.16
	SANVb6-TLR3	−1356.6	0.19
3	C6-TLR7	−1373.3	0.77
	SANVa9-TLR7	−1516	0.14
	SANVb6-TLR7	−1433.8	0.17

3.9. MD Simulation Analysis of Docked Molecular Complexes (SANVa9 with TLR3 and SANVa9 with TLR7)

MD simulation with GROMACS is a valuable tool for assessing protein stability under varying thermobaric conditions. It relies on fundamental physical theories of interatomic forces to forecast how atoms will move over time between proteins and other molecular systems [135]. While MD simulations offer detailed atomic-level insights into structural dynamics, not all such details are relevant to the macroscopic properties of interest. Therefore, in this study, MD simulations of SANVa9-TLR3 and SANVb6-TLR7 complexes were analyzed using key parameters, including RMSD, RMSF, Rg, SASA, and H-bond formation. RMSD is a key

parameter used to assess the conformational differences between protein structures over time. It measures the average distance between backbone atoms of the original protein structure and those of the aligned simulated structures [136]. A lower RMSD value indicates greater structural stability, whereas a higher RMSF value indicates greater protein flexibility. RMSF specifically evaluates the flexibility of the backbone atoms by measuring the extent of atomic movement into protein and peptide residues. Typically, intricate stability is considered acceptable when these fluctuations remain below 4 Å [137]. The overall compactness and flexibility of the complexes were evaluated by analyzing Rg profiles [138]. A lower value of Rg suggests a tighter, folded and stable structure of proteins, while higher values indicate a larger or less compact structure. The Rg value essentially reflects the protein's size and folding pattern. SASA analysis was conducted to determine the extent of the protein surface exposed to the surrounding solvent, distinguishing between hydrophilic and hydrophobic regions [136]. An increased SASA value indicates greater surface exposure and higher hydrophilicity, often associated with expanded or flexible protein regions [139]. The average SASA value reflects the degree of solvent exposure of the protein's surface throughout the simulation. Hydrogen bonds also play a vital role in stabilizing protein–ligand complexes, as these transient, non-covalent interactions significantly contribute to the structural integrity and stability of proteins. In this study, RMSD values were calculated over a 100 ns simulation for the SANVa9-TLR3 and SANVb6-TLR7 complexes, with the average RMSD values summarized in Table 7. These results reflect the relative stability of the protein complexes throughout the simulation, with both systems maintaining stable conformations over the 100 ns period (Figures 10A and 11A). Rg measures the overall compactness and folding of the protein structures at various time points. The Rg plots for both complexes, illustrated in Figures 10B and 11B, demonstrate consistent folding patterns throughout the simulation. The average Rg values for the SANVa9-TLR3 and SANVb6-TLR7 complexes were 3.25 ± 0.02 nm and 3.6 ± 0.02 nm, respectively, indicating stable, compact structures over time. RMSF analysis was conducted to identify the amino acid residues exhibiting higher flexibility, which can lead to local destabilization. RMSF values were also computed over the 0 –100 ns timescale, and the average values for both SANVa9-TLR3 and SANVb6-TLR7 complexes are presented in Table 7. As shown in Figures 10C and 11C, the RMSF analysis revealed no significant fluctuations, indicating that the proteins retained their structural integrity throughout the simulation. To assess the compactness of the hydrophobic core, SASA was analyzed. The changes in SASA for the SANVa9-TLR3 and SANVb6-TLR7 complexes are shown in Figures 10D and 11D, with the average SASA values reported in Table 7. The results suggest no significant structural alterations, further confirming the stability of the complexes throughout the simulation. H-bond analysis, which plays a crucial role in maintaining protein stability, was also performed. The presence and consistency of hydrogen bonds observed during the simulation confirmed the interactions predicted by molecular docking. The H-bond profiles for the SANVa9-TLR3 and SANVb6-TLR7 complexes are depicted in Figures 10E and 11E, respectively. Most functionally important structural changes in proteins occur on time scales of nanoseconds, microseconds, or longer. In practice, MD simulation time depends on achieving trajectory stability, as observed 100 ns in this work [140,141]. Moreover, longer trajectories (up to 200 ns) are needed to properly establish structural convergence or to observe slow conformational changes [142].

Table 7. MD simulation analysis of molecular complexes SANVa9-TLR3 and SANVb6-TLR7 conducted for 100 ns with their average values of RMSD, RMSF, Rg, H-bonds, and SASA.

S. No.	Molecular Complexes	Average RMSD (nm)	RMSF (nm)	Rg (nm)	Average SASA (nm^2)	H Bonds
1	SANVa9-TLR3	0.7 ± 0.01	0.25± 0.05	3.25 ± 0.02	365 ± 2.20	480
2	SANVb6-TLR7	3 ± 0.01	0.18 ± 0.05	3.6 ± 0.02	420 ± 2.20	525

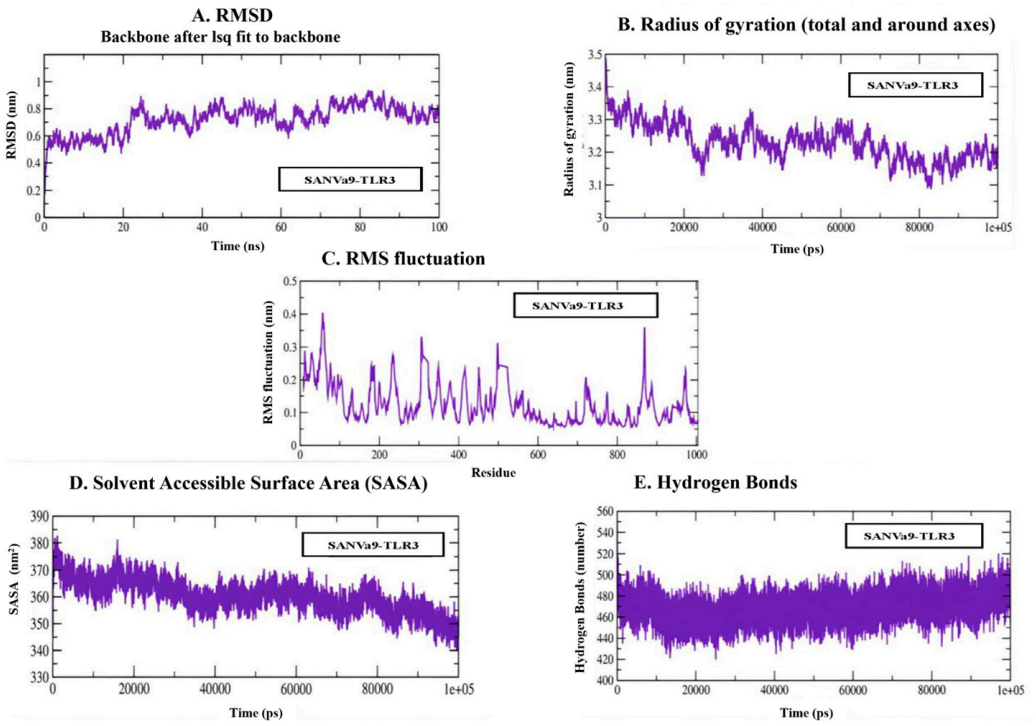


Figure 10. MD simulation analysis of SANVa9-TLR3 complex for 100 ns. RMSD plot (**A**), Rg (**B**), RMSF plots (**C**), SASA plot (**D**), and Hydrogen bond (**E**). The last x-axis value is displayed in exponential notation.

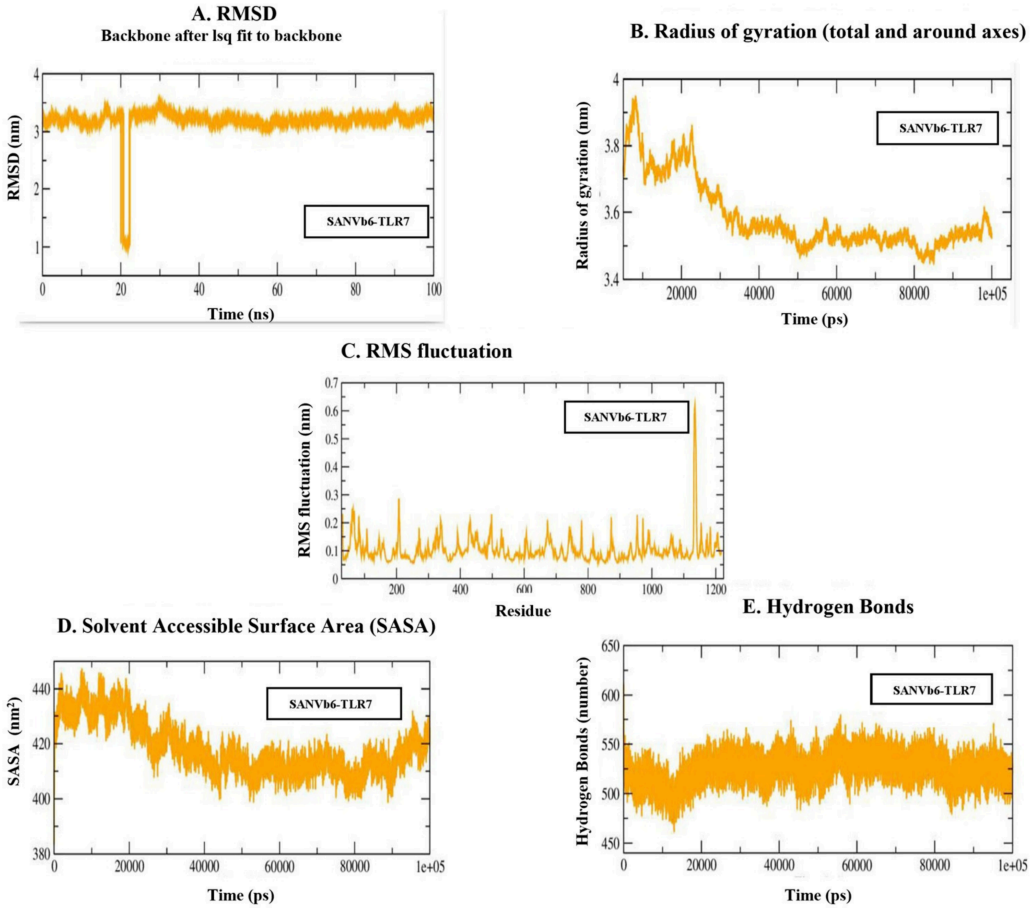


Figure 11. MD simulation analysis of SANVb6-TLR7 complexes for 100 ns. RMSD plot (**A**), Rg (**B**), RMSF plots (**C**), SASA plot (**D**), and Hydrogen bond (**E**). The last value on the x-axis is displayed in exponent notation. For example, 1e+05 represents 1×10^5, which is equivalent to 100,000.

3.10. Immune Simulation of the SANV Constructs (SANVa9 and SANVb6)

The C-IMMSIM simulation tool assesses immune system activation parameters, including total B-cell count (cells/mm^3), T-helper (Th) cell count (cells/mm^3), interferon-gamma (IFN-γ) levels (ng/mL), and the population of active cytotoxic T (Tc) lymphocytes (cells/mm^3). This study evaluated the immune responses of SANV constructs (SANVa9 and SANVb6) against SARS-CoV-2 using the C-IMMSIM simulation platform, with the rSMEV vaccine (C7) and UB-612 (C8) serving as positive controls. In prior experimental studies by Yu et al. [51] the C7 demonstrated strong immunogenicity, significantly enhancing antibody-secreting cell responses and elevating IL-4 and IFN-γ levels in mice, indicating its potential to stimulate both humoral and cell-mediated immunity. However, vaccination with UB-612 (C8) elicited robust neutralizing antibody responses and strong cellular immunity in all tested models and effectively neutralized the ancestral SARS-CoV-2 strain and multiple variants of concern, including Delta and Omicron, as reported by Wang et al. [63]. Moreover, the immune simulation results for the controls (C7 and C8) and the current vaccine constructs (SANVa9 and SANVb6) were comparable. In which antigen levels declined sharply, becoming undetectable by about the tenth day after administration (Figure 12A). A noticeable rise in IgM/(IgG1 + IgG2) antibody titers was recorded after the second dose for C7, SANVa9, SANVb6, and C8 (Figures 12A and S5A). The total B-cell population was comparable across all vaccine design groups, with the control C7 showing a marginally higher count (~440 cells/mm^3), followed by SANVa9, SANVb6, and the UB-612 vaccine (C8), which exhibited similar levels (~430) (Figures 12B and S5B). This indicates that all vaccine constructs, including UB-612, were similarly effective in maintaining B-cell populations, with no marked differences in B-cell expansion among the groups. In contrast, notable differences were observed in T helper (Th) cell responses. The control vaccine C7 induced the highest Th-cell population (~5300), followed by the UB-612 vaccine (C8) (~4200), SANVa9 (~4000), and SANVb6 (~3700) (Figures 12C and S5C). These findings suggest that C7 is the most potent inducer of Th-cell responses, while UB-612 also demonstrates strong Th-cell stimulation, exceeding that of both SANV constructs. Similarly, IFN-γ concentrations were highest and comparable in the C7, UB-612, and SANVa9 groups (~420,000 ng/mL), whereas slightly lower levels were observed for SANVb6 (~400,000) (Figures 12D and S5D). This indicates that SANVa9, UB-612, and C7 are more effective at promoting IFN-γ production than SANVb6. The active cytotoxic T lymphocyte (Tc) population was highest in the SANVa9 group (~1100), followed by SANVb6, C7, and C8, all of which showed comparable Tc levels (~900) (Figures 12E and S5E). This suggests that SANVa9 is particularly effective in inducing cytotoxic T-cell responses, compared to SANVb6, C7, and C8. Overall, SANVa9 appears to be the most potent construct among those evaluated, due to its robust induction of B cell, Th cell, active Tc, and IFN-γ responses, which makes it ideal for broad-spectrum antiviral activity and long-term immunity. While SANVb6 displayed slightly lower Th and IFN-γ responses, it maintained a strong Tc response. These findings suggest SANVa9 as a potent vaccine candidate for broad and long-lasting antiviral protection, whereas SANVb6 may be preferred when a stronger cytotoxic response is prioritized. The significantly superior immune response of SANVa9 compared to SANVb6 might be due to differences in the amino acid sequences of the vaccine designs: SANVa9 (281 amino acids) vs. SANVb6 (355 amino acids) with adjuvant human β-defensin-3, Pan-HLA-DR, and TAT. The prediction of immune responses by C-IMMSIM, calculates the overall immunogenicity of a protein sequence (SANVa9/SANVb6) by simultaneously simulating three anatomical regions in humans: the bone marrow, the thymus, and the lymph node including B-cell epitopes prediction through Parker-scale affinity estimation, HLA class I and II binding peptides prediction through position-specific scoring matrices based on motifs derived from known HLA epitopes, and TCR binding to HLA–peptide complexes on the basis of

Miyazawa and Jernigan protein potentials [143]. These events are executed independently by cells, represented by agents that populate a given simulated biological volume according to the predicted number of epitopes. During the simulation, cells undergo transitions between activation or differentiation states, influenced by stochastic events that rely on the compatibility of their binding sites and affinity [144,145].

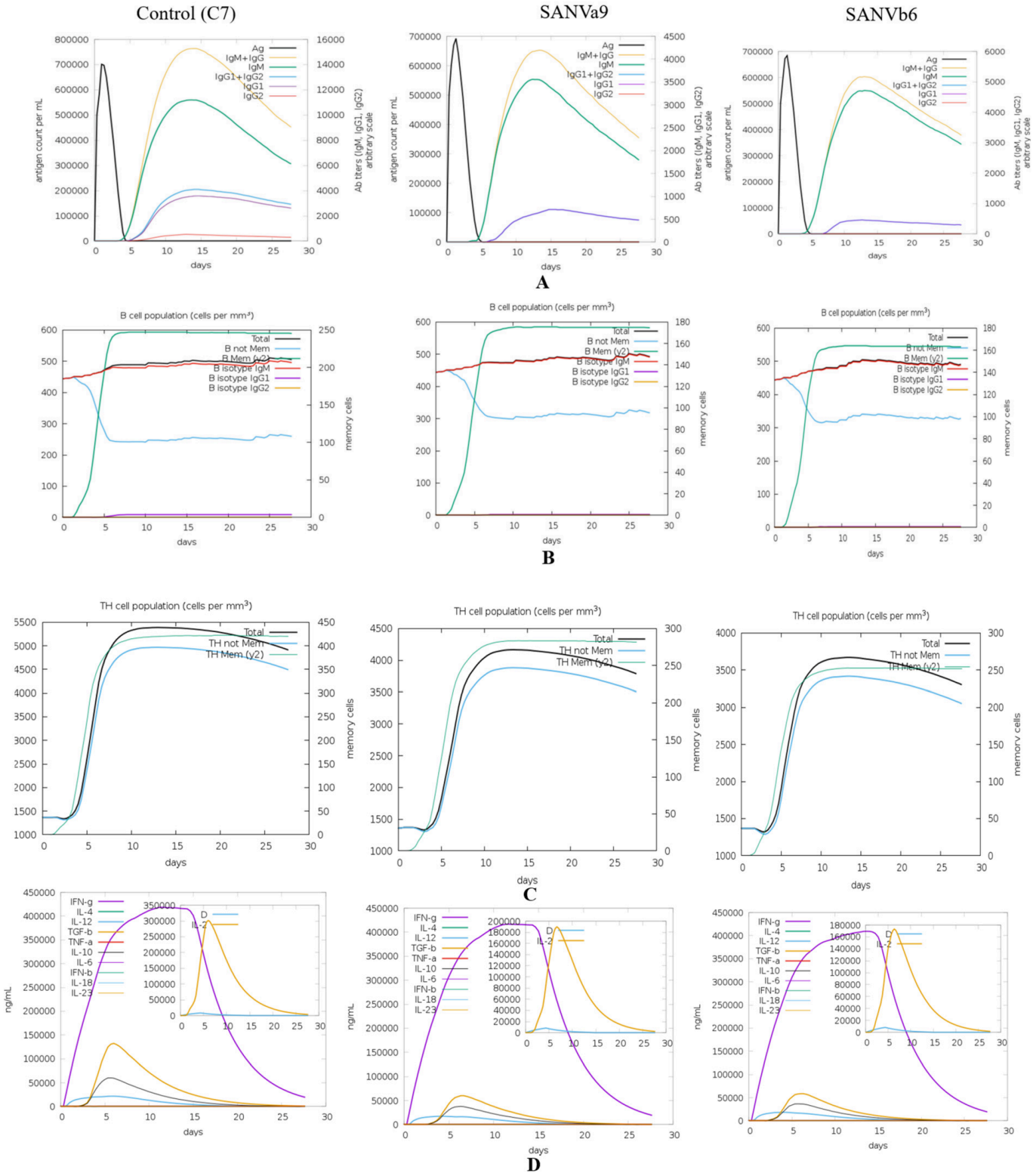


Figure 12. *Cont.*

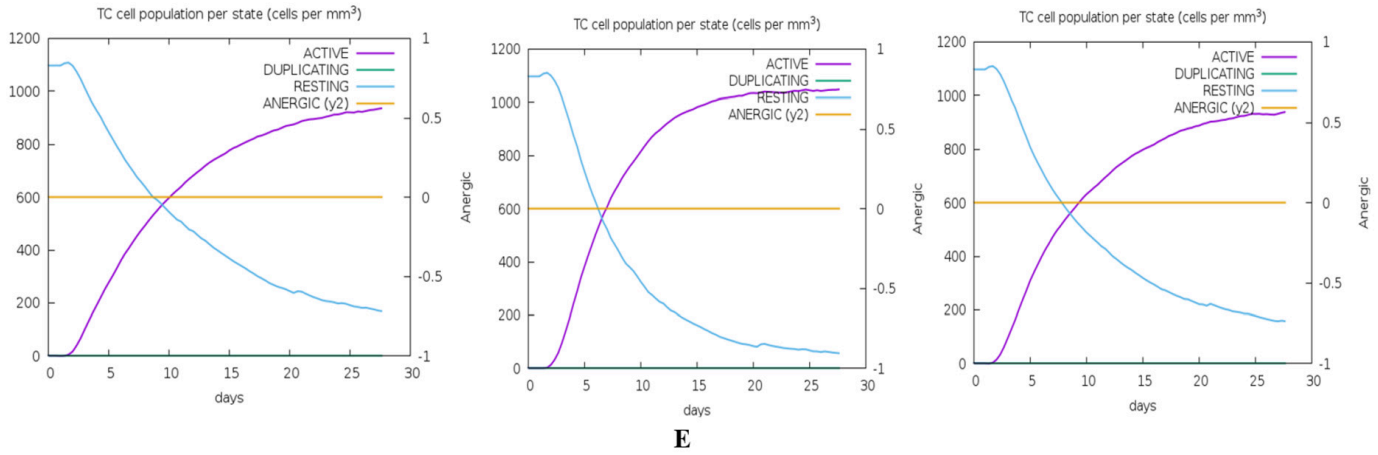


Figure 12. Immune simulation results generated utilizing the C-IMMSIM simulation system for the constructs SANVa9 and SANVb6, along with the rSMEV vaccine as positive control (C7). Levels of different immunoglobulin classes (**A**). Total B cell population (**B**). T-helper cell population per state (**C**). Cytokine response profile (**D**). Tc lymphocytes count per entity state. (**E**). Lanes 1, 2, and 3 correspond to C7 (positive control), SANVa9, and SANVb6, respectively.

3.11. Reverse Translation, Codon Optimization and In Silico Cloning of SANV Constructs

The total lengths of the codon-optimized cDNA sequences obtained for SANVa9 and SANVb6 were 843 bp and 1065 bp, correspondingly. The optimized sequences exhibited GC contents of 56.22% for SANVa9 and 51.73% for SANVb6, both of which fall into the recommended 30–70% range for efficient gene expression in *E. coli* expression hosts. Codon adaptation index (CAI) values of 0.985 and 0.974 were determined for SANVa9 and SANVb6, respectively, and both lie within the ideal range of 0.9–1.0. A reliable CAI value greater than 0.8 is considered indicative of high-level protein expression, while optimal GC content typically ranges between 3070% [66]. Collectively, the GC content and CAI values suggest that both constructs are highly suitable for efficient expression in *E. coli* strain K12. Furthermore, the recombinant DNA sizes generated by inserting the optimized cDNA sequences into the expression vector pET-28a(+) were determined to be 3399 bp for SANVb6 and 3621 bp for SANVa9. These recombinant constructs were successfully positioned between the ECO53KI and BstZ17I restriction sites, as illustrated in Figure 13 [146,147]. There are several reports indicating the feasibility of the *E. coli* system for the expression of complex fusion proteins [148–152] including the study of Yu et al. [51] who designed a recombinant multivalent epitope vaccine (containing CTL, HTL, and B-cell epitopes) against SARS-CoV-2.

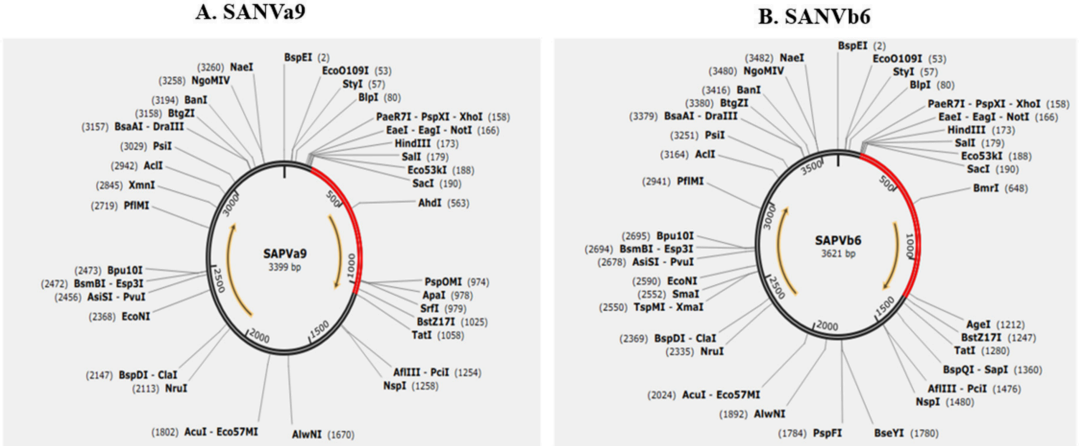


Figure 13. In silico restriction cloning of vaccine constructs SANVa9 (**A**) and SANVb6 (**B**) into the pET-28a(+) vector is illustrated, where the cloned sequences are highlighted in red.

4. Discussion

SARS-CoV-2 remains a significant threat, prompting global efforts to develop effective drugs and vaccines to combat the COVID-19 disease [153]. The field of multi-epitope vaccine (MEV) development is rapidly advancing and has shown promising outcomes not only in generating protective immunity in vivo [154] but also in progressing to phase I clinical trials [155–157]. MEV has emerged as a safer alternative to traditional vaccine platforms. Unlike conventional recombinant vaccines that rely on full-length proteins or the entire genome, this approach utilizes short immunogenic peptide sequences, thereby reducing the risk of antigen overload and minimizing allergenic reactions in the host [158]. MEV strategies involve the screening of the viral genome to identify multiple immunogenic epitopes, thereby inducing a highly specific immune response without contributing to viral pathogenicity [159]. MEVs offer several advantages over traditional vaccines due to their unique features: (i) They enable recognition by multiple MHC class I and II alleles and T cell receptors from diverse T cell subsets; (ii) overlapping/cross-reactive B cell, CTL and HTL epitopes allow simultaneous activation of both cellular and humoral immune responses; and (iii) the addition of adjuvants enhances immunogenicity and promotes a long-lasting immune response [155–160]. However, they are often limited by their inherently low immunogenicity and the variability of immunodominant regions across different viral serotypes/variants. Selecting conserved epitopes across the antigenic variants can help to overcome this hurdle and ensure a variant-proof vaccine. To address weak immunogenicity, this study employed a coiled-coil peptide-based SANV design strategy against SARS-CoV-2 [26]. Coiled-coil motifs have attracted considerable attention due to their structural stability and defined geometry. SANV has gained prominence in recent years due to its unique features, including biocompatibility, biodegradability, structural similarity to pathogens, intrinsic adjuvant properties, and repetitive architecture [36]. These alpha-helical coiled-coil motifs, are derived either from natural sequences or designed de novo.

For BL, HTL, and CTL epitope selection, both structural (N, M, E) and non-structural/accessory proteins (RPP1a, ORF3a, ORF6, ORF7a, ORF7b, ORF8, ORF10) viral proteins were chosen, excluding the S and orf1ab proteins, which were anticipated to generate a more potent and comprehensive immune response [20–22]. Amongst the retrieved epitopes from IEDB, a few epitopes were found to be cross-reactive with respect to the HLA binding profile. In which BL and HTL epitopes were filtered based on binding to HLA class II alleles, while CTL epitopes were assessed for HLA class I allele binding. The screened BL, HTL, and CTL epitopes were evaluated for sequence conservancy across 15 major SARS-CoV-2 variants (B.1.1.7, B.1.351, P.1, B.1.617.2, B.1.1.529, XBB.1, XBB.1.5, JN.1, KP.2, KP.3, KP.3.1.1, JN.1.18, LB.1, XEC, and LP.8.1). Furthermore, non-homology analysis of these conserved epitopes ensures minimal similarity with human proteins, reducing the risk of autoimmunity. Additionally, the minimum 50% population coverage analysis of individual epitopes ensures comprehensive coverage of the global human population. Finally, a minimal epitope set used in the SANV design constructs comprises 11 epitopes, including four BL epitopes (from N, M, E, and ORF8), three HTL epitopes (from N, M, and ORF3a), and four CTL epitopes (from N, M, E, and ORF3a). This optimized epitope set was fully conserved, immunologically relevant, broadly population-covering, and non-homologous to human proteins, making it suitable for peptide synthesis and ideal for downstream vaccine development efforts [24]. While commercial vaccines exhibited a gradual loss of T cell epitope conservation with the VOC over time, these epitopes remained conserved until the recent variant emerged. The addition of a new peptide to the vaccine design reestablished broad T-cell epitope coverage. Similar findings underscore the importance of identifying highly conserved T cell epitopes for vaccine designs that target rapidly mutating strains of emergent pathogens [25].

Cytokines have been widely applied in the treatment of various autoimmune disorders and cancers, including multiple myeloma [161], arthritis [162], psoriasis [163], and different malignancies [164]. Among these, interleukin-10 (IL-10) is well-recognized for its immunosuppressive properties [165], playing a vital role in mitigating inflammatory responses, alleviating autoimmune pathologies [166], and enhancing graft survival [167,168]. Initially categorized as a Th2-type cytokine, IL-10 is now understood to be broadly expressed across multiple immune cell types [169,170]. Similarly, interleukin-4 (IL-4), predominantly secreted by Th2 cells, has been extensively studied for its capacity to counteract the deleterious effects of Th1-mediated immune responses [171]. IL-4 also plays a crucial role in antibody isotype switching, notably stimulating IgE production. It contributes to the proliferation and differentiation of antigen-presenting cells, further demonstrating its diverse biological functions [172]. Th1 responses are primarily induced through cytokines such as IFN-γ and TNF-α, whereas Th2 responses are driven by cytokines including IL-13, IL-5, and IL-4 [173]. Moreover, the selected optimal set of epitopes, BL1, BL2, and HTL1, is predicted to induced both IFN-γ and IL-4, however not IL-10, demonstrating their potential to activate a balanced Th1 and Th2 immune response. This indicates that BL1, BL2, and HTL1 may facilitate both Th1 and Th2 immune responses, while also contributing to the regulation of mast cell–mediated pro-inflammatory cytokine reduce release [39,75]. In contrast, BL3 and BL4 epitopes were predicted to trigger IL-10, IL-4 without IFN-γ, thereby inducing Th2 responses that may help reduce inflammation and regulate immune activation, potentially modulating excessive immune responses [166], whereas HTL2 and HTL3 promoted IL-4 production, highlighting its selective involvement in Th2-mediated responses. Thus, an in silico assessment of the screened minimal epitope set further validated its utility in the design of SANV constructs.

T cells recognize pathogens through their distinct T cell receptors (TCRs), which bind to peptide fragments displayed by major histocompatibility complex (MHC) molecules. Vaccination introduces antigens to the immune system, triggering the activation and expansion of antigen-specific T cells and promoting the formation of memory T cells that can respond rapidly upon subsequent exposure to the same or similar pathogens. Therefore, in-depth analysis of the CDR3β sequences corresponding to CTL1, CTL2, and CTL4 revealed a notable overlap in T-cell receptor recognition across multiple viral epitopes. Specifically, epitopes such as AVFDRKSDAK (Epstein-Barr virus), LSPRWYFYYL (nucleocapsid phosphoprotein, SARS-CoV-2), KLGGALQAK (55 kDa immediate-early protein 1, Human cytomegalovirus), MIELSLIDFYLCFLAFLLFLVLIML (ORF7a protein, SARS-CoV-2), and VLAWLYAAV (non-structural polyprotein pp1a, SARS-CoV-2) were commonly recognized by CDR3β sequences from CTL1 and CTL4 (Supplementary Files S4; Table S2). This overlap suggests that certain viral epitopes possess conserved features that allow recognition by similar TCRs, thereby promoting cross-reactivity among T-cell responses. Importantly, this cross-reactivity was not limited to a single pathogen but extended to multiple viruses, including SARS-CoV-2, Epstein-Barr virus, Human cytomegalovirus, Influenza A virus, Hepatitis B virus, yellow fever virus, Human rotavirus strain WA, and Mycobacterium tuberculosis. This highlights the universal immune relevance of such epitopes and underscores their potential utility in the design of broad-spectrum vaccines and therapeutics [84]. Mucosal-associated invariant T (MAIT) cells represent a specialized subset of T lymphocytes characterized by semi-invariant T cell receptor alpha (TCRα) chains and the capacity to recognize microbial-derived small-molecule metabolites presented by the MHC class I-related protein MR1 [174,175]. These cells play an important immunoprotective role in mucosal tissues, particularly during respiratory infections, as demonstrated in murine models [176,177]. In this study, a comparative assessment using the MAIT Match 1.0 algorithm revealed that TCR sequences derived from SARS-CoV-2-specific CTL3 and CTL4 showed

similarity scores exceeding 0.84, suggesting possible similarity to the MAIT TCR. This considerable degree of similarity observed between SARS-CoV-2 TCR sequences and known MAIT cell TCRs suggests a potential role for MAIT cells in the immune response against SARS-CoV-2. This finding is significant for vaccine development, as harnessing MAIT cell activation may enhance immune protection, particularly in mucosal tissues such as the lungs and gastrointestinal tract, where these cells are predominantly located [178,179].

The identification of conserved epitopes across multiple bat- and pangolin-derived coronaviruses supports the concept of heterologous immunity, through which immunological response generated against single pathogen can confer partial protection against another [180,181]. In this study, several fully conserved peptide sequences corresponding to epitopes (BL1–BL4, HTL1–HTL3, and CTL1–CTL4) were identified across various *sarbecoviruses*, notably Horseshoe bat sarbecovirus, Rhinolophus thomasi bat coronavirus, and Pangolin coronavirus. This shared immunogenicity aligns well with the existing literature on heterologous immunity, which shows that prior exposures or vaccinations (e.g., BCG) confer non-specific immune benefits. For instance, BCG vaccination in infants has been associated with a reduction in mortality from unrelated infections, such as pneumonia and sepsis [82]. Although most studies attribute the non-specific protective effects of prior BCG exposures or vaccinations to innate immune activation and trained immunity [182]. Trained immunity occurs when innate cells, such as monocytes and natural killer (NK) cells, undergo long-lasting functional changes. However, some studies suggest that BCG can expand effector memory T cells that cross-react with other pathogens (e.g., influenza A virus) [183]. Additionally, a notable similar experimental study identified several BCG-derived peptides with sequence homology to SARS-CoV-2 NSP3 and NSP13 peptides and demonstrated that BCG peptide priming enhanced CD4+ and CD8+ T-cell responses to homologous SARS-CoV-2 peptides in vitro, supporting a mechanism of TCR-mediated heterologous immunity through conserved epitopes [184]. Furthermore, it has been implicated in modulating immune responses, thereby potentially reducing the likelihood of autoimmune and inflammatory disorders, such as type 1 diabetes and multiple sclerosis [83]. These examples underscore the importance of identifying conserved, cross-reactive epitopes for the development of broad-spectrum vaccines [30,31].

For SANV design, epitopes were joined using suitable linkers and fused with pentameric and trimeric oligomerization domains. A total of 24 SANV constructs were designed, comprising 12 constructs with adjuvant, TAT, and PADRE sequences and 12 without these elements (Table 3). The selection of appropriate linkers is critical in multi-epitope vaccine design, as they help maintain the structural and functional independence of each domain, thereby reducing potential interference. In addition, certain linkers enhance binding to TAP transporters and serve as helical connectors, thereby improving the overall immunogenicity of the construct. The choice of linker depends on the specific design goals and structural requirements of the vaccine [99,100]. Furthermore, the 3D structures of SANV constructs were modelled, refined, and validated to ensure structural accuracy and reliability. Based on the analysis, the most suitable SANVa and SANVb models were identified for further self-assembly studies [185]. The stability of a recombinant protein largely depends on its proper 3D folding, as correctly folded proteins generally exhibit greater stability and a longer shelf life [145]. Among the 24 SANV constructs analysed, SANVa9 and SANVb6 displayed the most favourable homo-oligomeric interfaces, as determined by GalaxyHomomer (Table 4). Homo-oligomers with small interface areas typically form through the association of pre-folded monomers, resulting in globular subunits with surface properties similar to those of monomeric proteins. In contrast, oligomers with large interface areas, such as SANVa9 and SANVb6, are likely to involve significant conformational changes during assembly, as isolated subunits in such systems tend to be unstable [186]. Therefore,

advanced structural prediction using AlphaFold-Multimer of SANVa9 and SANVb6 candidates, alongside known SAPN-based vaccine constructs (MPER-SAPN and P4c-Mal SAPN), revealed comparable pTM and ipTM scores across these models. The pTM score estimates how accurately the overall structure of the protein complex is modelled, while the ipTM score assesses the reliability of the predicted orientations between interacting subunits. It is important to note that these TM-based scoring metrics tend to be highly conservative for small proteins or peptide chains, often yielding very low pTM values, typically below 0.05, when the sequences contain fewer than 20 amino acid residues [187,188]. Bodenreider et al. [189] reported that the process of oligomer folding involves a combination of intramolecular interactions responsible for individual monomer folding and intermolecular interactions that drive the assembly of subunits into the final oligomeric structure. In the monomer sequence design, Luo et al. [190] reported that although the constructs P1-A and P1-B contained identical heterogeneous T-cell epitopes, using different insertion strategies led to notable differences in self-assembly behavior and structural stability, thereby influencing their physical and structural properties. This underscores the importance of molecular simulations, particularly for optimizing linker sequences and for employing fused-dimer techniques in chimeric protein formulation. Recently, Cao et al. [191] analyzed vaccine optimization strategies, including consensus sequence/structure-based antigen design, targeting conserved epitopes, and chimeric immunogen design for utilizing protein nanoparticle-based transport systems to induce broad immune responses. In a similar optimized nanovaccine design containing SARS-CoV-2 S and N antigens, long-lived systemic IgG antibody responses against wild-type SARS-CoV-2 and cross-reactivity to multiple SARS-CoV-2 variants (including B.1.1.529) were induced, along with antigen-specific CD4+ and CD8+ T cell responses [192]. Moreover, physicochemical analysis of SANVa9 and SANVb6 constructs revealed several favourable characteristics supporting their suitability as vaccine candidates [147] with respect to molecular weight [109], GRAVY values [193], aliphatic index [111,194], antigenicity [145,195], solubility [196], allergenicity [197].

Molecular docking studies assessed the binding affinity and interaction characteristics of SANV constructs (SANVa9 and SANVb6) and the control C3 with the SARS-CoV-2-specific 5817 antibody. The antibody 5817 has been identified as a broad-spectrum neutralizer effective against multiple SARS-CoV-2 variants of concern (VOCs) and targets a highly conserved epitope within the RBD, which is accessible only when the RBD is in its open conformation [58]. The docking results confirmed that the evaluated antibodies successfully interacted with the SANV constructs. Both SANVb6 and SANVa9 exhibit stronger binding affinity for the 5817-antibody than the control, indicating their potential as high-affinity antigenic constructs. Moreover, conformational B-cell epitopes mapping within the 3D structures of the SANV constructs (SANVa9 and SANVb6) revealed their strong potential to induce humoral immune responses [195,198]. In a similar finding, Shah et al. [199] highlight the implications of innovative vaccine strategies targeting immunodominant/immunoprevalent B-cell epitopes, as well as promiscuous T-cell epitopes, to initiate broad and robust humoral and cellular immune responses against a wide range of SARS-CoV-2 variants.

TLRs play a crucial role in the innate immune system's recognition of pathogen-associated molecular patterns (PAMPs) and virus-associated molecular patterns (VAMPs). Intracellular TLRs, such as TLR3 and TLR7, play a crucial role in sensing viral RNA and triggering immune responses, including the production of type I interferons and pro-inflammatory cytokines, which are essential for effective antiviral immunity [200–202]. TLR3, localized in endosomal membranes, specifically recognizes double-stranded RNA motifs typical of viral genomes and replication intermediates, triggering downstream signalling pathways through adaptor proteins such as TRIF [200,202]. The role of TLRs

in the immune response to SARS-CoV-2 has been identified, particularly in regulating inflammation and viral clearance [203]. TLR3, TLR7, TLR8, and TLR9 have been shown to bind to specific regions of the viral genome NSP10, E-protein, NSP8, and S2, respectively, thereby activating innate immune mechanisms [203]. Moreover, TLR7 has been implicated in regulating interferon production during coronavirus infections, and natural mutations in the TLR7 gene have been associated with increased disease severity in young patients with COVID-19 [204]. Likewise, studies have shown that TLR2 interacts with the SARS-CoV-2 E protein, triggering the pro-inflammatory cytokine release. Inhibition of TLR2 has been found to provide protective effects in animal models [205]. Therefore, targeting these receptors with agonists could serve as a therapeutic strategy to modulate immune responses during infections, such as COVID-19 [201]. However, to evaluate the immunostimulatory potential of the SANV constructs, molecular docking was performed with TLR2, TLR3, and TLR7. The docking and binding energy analyses revealed that SANVa9 and SANVb6 bind more strongly to these receptors compared to their known ligands (controls). SANVa9 appears to be more specialized in targeting TLR7, which plays a central role in type I interferon production during viral infections [206,207]. In this study, β-defensin was used as an adjuvant in the SANV constructs, primarily because it acts as a TLR3 agonist, thereby enhancing immune responsiveness. The inclusion of β-defensin likely enhances these interactions, particularly with TLR3, supporting its role as an effective adjuvant component. Collectively, the docking and interaction data reinforce the hypothesis that these SANV constructs can serve as potent immunomodulators. However, further stability validation through MD simulation studies is required. The SANVa9–TLR3 and SANVb6–TLR7 complexes demonstrated significant stability during MD simulations of 100 ns and yielded substantial values for RMSD, RMSF, Rg, SASA, and hydrogen bonds. RMSD, which measures the average atomic displacement over time, is commonly used to assess the structural stability and equilibration of ligand-bound proteins. A lower RMSD in the ligand-bound complex compared to the unbound protein indicates enhanced structural stabilization [208,209]. RMSF is a valuable parameter that measures the average positional deviation of amino acid residues during an MD simulation, helping to identify flexible and rigid regions within a protein structure. Typically, lower RMSF values indicate restricted movement and structural stability, whereas higher values suggest greater flexibility. RMSF analysis offers valuable insights into the behavior of amino acid residues upon ligand binding, thereby contributing to a deeper understanding of the overall stability of protein–ligand complexes [136]. However, the Rg indicates that both complexes maintained compact and stable structural conformations throughout the simulation. Analysing the Rg is crucial for understanding how ligand binding influences a protein's overall compactness and structural organization. It serves as an important parameter for evaluating the stability and flexibility of protein–ligand complexes during molecular dynamics simulations [139]. SASA is a critical parameter in evaluating protein stability and folding behavior. A solvent sphere with a hypothetical centre surrounds the van der Waals contact surface of a protein. Higher SASA values typically indicate greater solvent exposure, which can be associated with increased solubility [210]. Hydrogen bonding plays an important part in the formation and stabilization of protein structures [211].

Finally, this study evaluated the immune responses of SANV constructs (SANVa9 and SANVb6) towards SARS-CoV-2 evaluated through the C-IMMSIM simulation platform, in addition to the rSMEV vaccine design (C7). The SANV constructs (SANVa9 and SANVb6) demonstrated immune responses comparable to those of C7 in the C-IMMSIM simulation, with respect to effective antigen clearance, a significant rise in IgM and IgG antibody titers, B cell population, Th cell response, and IFN-γ levels. The progression of primary, secondary, and tertiary immune responses clearly indicates the successful elimination of the antigen

from the system (Figure 12). The immune system simulator (C-IMMSIM) is a versatile tool that integrates both modelling and simulation, and has been tailored to study various diseases, including Epstein–Barr virus [212], HIV [213], and cancer [214], as well as for adjuvant selection [215]. It has also been used to explore the activation of gene regulatory networks during Th1 and Th2 cell polarization [216] and the differentiation of helper T cells into Th17 and Treg subsets [217]. To ensure efficient expression in an *Escherichia coli* host, the designed SANV construct was codon-optimized, followed by reverse translation of the linear amino acid sequence into its corresponding cDNA. The optimized sequences (SANVa9 and SANVb6) exhibited GC contents of 56.22% and 51.73%, respectively, indicating their suitability for high-level expression in *E. coli*. Subsequently, in silico cloning of the optimized vaccine sequence was performed by inserting it into the pET-28a(+) expression vector, enabling expression within a bacterial system. A comparable codon optimization strategy prior to in vitro expression has also been reported by Foroutan et al. [147]. Several computational studies have reported on the design of SARS-CoV-2 vaccine candidates, in which the SANVa9 and SANVb6 constructs exhibit favourable attributes, such as optimal size, structural stability, and broad population coverage (Table 8).

Table 8. Comparative assessment of SANVa9 and SANVb6 constructs with existing computationally designed vaccine candidates.

Feature	Subunit Vaccine [21]	Multi-Epitope Vaccine [218]	MEV [219]	Multi-Epitope DNA Vaccines [220]	MESV [20]	SANVa9/SANVb6 (This Study)
Size (Molecular weight in kDa)	95.4	60.77	52.29	31,264.59	3157.01	31.56/40.08
Thermostable stability (aliphatic index)	79.29	73.02	89.34	Not available	95.07	71.21/87.01
Adjuvant inclusion	Human β-defensin-3	50S ribosomal protein L7/L12 (rpIL)	β-defensin-3	No adjuvant	Human β-defensin-3	Human β-defensin-3
World population coverage (%)	95	96.77	98.64	96.98	88.40	99.67

However, in experimental work, Yilmaz et al. [221] reported a vaccine candidate based on virus-like particles displaying the S, N, M, and E structural proteins, which closely mimic the morphology of SARS-CoV-2. In another study, Gao et al. [222] designed innovative glyconanoparticle-based vaccines by chemically linking the full-length recombinant N protein to multiple high-affinity dextran molecules. These formulations successfully elicited robust anti-N antibody responses in both mice and rabbits, resulting in strong, long-lasting N-specific cytotoxic T lymphocyte activity against cells infected with various SARS-CoV-2 variants. Furthermore, the designed computational SARS-CoV-2 vaccine constructs incorporated adjuvant components such as human β-defensins and the 50S ribosomal protein L7/L12 (rpIL) integrated with predicted CTL, HTL, and B-cell epitopes derived from the N, M, and E proteins, which were linked using GPGPG spacers [218–220]. In contrast, this study introduces a distinct design approach by using experimentally validated epitopes from the N, M, E, ORF3a, and ORF8 proteins, combined through self-assembling pentameric and trimeric coiled-coil domains, to construct innovative SANV prototypes. In contrast to conventional protein-based systems for self-assembling nanoparticles, that includes mosaic nanoparticles [223–226], this approach does not require external protein scaffolds or recombinant nanoparticle carriers. The structural integrity and physicochemical properties

of intact SAPN must be preserved throughout the formulation process [227]. Furthermore, epitope selection was unique in terms of experimentally demonstrated immune recognition, HLA-binding profiles, and TCR similarities. The chosen epitopes exhibit high conservation, promiscuous binding characteristics, and cross-reactivity across diverse SARS-CoV-2 variants. Specifically designed coiled-coil monomeric SANV constructs (SANVa9 and SANVb6), functionalized with multiple tags (e.g., epitopes, linkers, adjuvant, TAT sequence, and PADRE), are found to be stable and self-assemble into ordered supramolecular nanostructures. The formation of SAPN with various sizes and morphologies is driven by hydrophobic packing, hydrogen bonding, van der Waals forces, and electrostatic interactions [228–231]. Structural modifications of monomeric peptides, particularly linkers between epitopes, components (e.g., epitopes, adjuvants, TAT domain), and their positions within the monomer, often result in significant changes in magnitude and quality of the immune response [232–234]. This might have occurred due to component rearrangement, which can induce conformational changes in the antigenic peptide and influence the conjugate's ability to self-assemble into nanoparticles [235,236]. Fusing additional proteins to the coiled-coil motifs enabled the creation of nanoparticles with cargo segments displayed on their exterior surfaces [237,238]. The proximity and density of peptide antigens within a conjugate are important in DC maturation, antigen presentation, T cell proliferation, and the induction of CD8+ T cells [239]. The minimalist design promotes homo-oligomerization, allowing self-assembly of the antigen in the absence of requiring exterior scaffolds or carriers of recombinant nanoparticles, and considerably lowers production level of complexity. Although the application of modern organic chemistry may permit the conjugation of several different epitopes, adjuvants, and targeting moieties into a single polypeptide vaccine construct, a physical mixture of peptides can be combined with an appropriate formulation to ensure the co-delivery of vaccine components [240,241]. Moreover, the manufacturing of nanovaccines for commercialization presents numerous challenges: the total synthesis of polypeptides, which might be too expensive, too labor-intensive to produce, and difficult to scale up [242], including technology transfer, batch-to-batch variability in size, and the development of controllable, reproducible [243]. Therefore, to effectively address the challenges inherent to scaling up nanovaccine production, precision nanotechnologies, continuous manufacturing platforms, and microfluidic-based synthesis technologies and strategies such as 'quality-by-design' and 'formulation-by-design' may provide a rational and scientific framework for optimizing formulations, thereby improving their clinical translation potential [244–246].

5. Conclusions

Vaccination remains a crucial strategy for ending pandemics, including the COVID-19 pandemic caused by the SARS-CoV-2 virus. Traditional vaccine development methods present several limitations, making them less practical in urgent scenarios. This study introduces an improved structural design approach that incorporates experimentally validated promiscuous and T- and B-cell epitopes with potential cross-reactivity derived from the N, M, E, ORF3a, and ORF8 proteins. These epitopes cover approximately 99% of the global population, eliciting a strong immune response in simulation, and are conserved across multiple SARS-CoV-2 strains. Remarkably, the chosen epitopes were homologous to those of Bat SARS-like Coronavirus, Horseshoe Bat Sarbecovirus, and Rotavirus A, suggesting a strong potential for cross-reactive immunity. The rational arrangement of epitopes, combined with the inclusion of a suitable adjuvant component, TAT sequence, linkers, and self-assembling coiled-coil domains forming pentamers and trimers, enabled the construction of SANV candidates that can form stable, higher-order nanostructures. These nanoparticle-based vaccine constructs offer enhanced epitope density and multivalent antigen presentation,

providing advantages in manufacturing efficiency and ultimately facilitating easier production and scalability. However, further validation through experimental and clinical testing is recommended to confirm its efficacy.

Supplementary Materials: The following supporting information can be downloaded at https://www.mdpi.com/article/10.3390/biophysica6040055/s1: Figure S1: The ribbon diagram representations of the tertiary structures of SAPV constructs; Figure S2:The ribbon diagram representations of docked complexes between the 5817 antibody and (A) Control (C3), (B) SANVa9, and (C) SANVb6; Figure S3: Structural visualization of docking models; Figure S4: Schematic representation of interactions between the human TLR2, TLR3, and TLR7 receptors and the controls (C4, C5, C6) as well as SANV constructs; Figure S5: The result of C-IMMSIM-based immune simulation for UB-612 vaccine (C8) positive control; Table S1: Comparison of SARS-CoV-2 TCR Sequences with MAIT Cell TCRs. The data (Supplemental File S1–S4) that support the findings of this study are openly available in Mendeley Data at https://data.mendeley.com/datasets/7tgpwvghhk/1 (accessed on 5 December 2025) reference number https://doi.org/10.17632/7tgpwvghhk.1.

Author Contributions: P.J.: Formal analysis, Investigation, Writing—original draft, Writing—review and editing, Validation, Methodology, Data curation, Conceptualization. S.P.S.: Writing—review and editing, Methodology, Investigation, Supervision, Conceptualization. All authors have read and agreed to the published version of the manuscript.

Funding: This research received no external funding.

Institutional Review Board Statement: Not applicable.

Informed Consent Statement: Not applicable.

Data Availability Statement: The data (Supplemental File S1–S4) that support the findings of this study are openly available in Mendeley Data at https://data.mendeley.com/datasets/7tgpwvghhk/1 (accessed on 5 December 2025) reference number https://doi.org/10.17632/7tgpwvghhk.1.

Acknowledgments: The authors are thankful to Mahatma Gandhi Central University, Motihari, for supporting PJ with a PhD studentship.

Conflicts of Interest: The authors declare no conflicts of interest.

References

1. Huang, C.; Wang, Y.; Li, X.; Ren, L.; Zhao, J.; Hu, Y.; Zhang, L.; Fan, G.; Xu, J.; Gu, X.; et al. Clinical features of patients infected with 2019 novel coronavirus in Wuhan, China. *Lancet* **2020**, *395*, 497–506. Erratum in *Lancet* **2020**, *395*, 496. https://doi.org/10.1016/S0140-6736(20)30252-X. [CrossRef] [PubMed]
2. Lu, H.; Stratton, C.W.; Tang, Y.W. Outbreak of pneumonia of unknown etiology in Wuhan, China: The mystery and the miracle. *J. Med. Virol.* **2020**, *92*, 401–402. [CrossRef] [PubMed]
3. Khailany, R.A.; Safdar, M.; Ozaslan, M. Genomic characterization of a novel SARS-CoV-2. *Gene Rep.* **2020**, *19*, 100682. [CrossRef] [PubMed]
4. Zhang, G.; Zhang, J.; Wang, B.; Zhu, X.; Wang, Q.; Qiu, S. Analysis of clinical characteristics and laboratory findings of 95 cases of 2019 novel coronavirus pneumonia in Wuhan, China: A retrospective analysis. *Respir. Res.* **2020**, *21*, 74. [CrossRef] [PubMed]
5. Ungarala, R.; Munikumar, M.; Sinha, S.N.; Kumar, D.; Sunder, R.S.; Challa, S. Assessment of Antioxidant, Immunomodulatory Activity of Oxidised Epigallocatechin-3-Gallate (Green Tea Polyphenol) and Its Action on the Main Protease of SARS-CoV-2—An In Vitro and In Silico Approach. *Antioxidants* **2022**, *11*, 294. [CrossRef] [PubMed]
6. Manne, M.; Goudar, G.; Varikasuvu, S.R.; Khetagoudar, M.C.; Kanipakam, H.; Natarajan, P.; Ummiti, M.D.; Yenagi, V.A.; Chinthakindi, S.; Dharani, P.; et al. Cordifolioside: Potent inhibitor against Mpro of SARS-CoV-2 and immunomodulatory through human TGF-β and TNF-α. *3 Biotech* **2021**, *11*, 136. [CrossRef] [PubMed]
7. Ram, T.S.; Munikumar, M.; Raju, V.N.; Devaraj, P.; Boiroju, N.K.; Hemalatha, R.; Prasad, P.V.V.; Gundeti, M.; Sisodia, B.S.; Pawar, S.; et al. In silico evaluation of the compounds of the ayurvedic drug, AYUSH-64, for the action against the SARS-CoV-2 main protease. *J. Ayurveda Integr. Med.* **2022**, *13*, 100413. [CrossRef] [PubMed]
8. Naik, V.R.; Munikumar, M.; Ramakrishna, U.; Srujana, M.; Goudar, G.; Naresh, P.; Kumar, B.N.; Hemalatha, R. Remdesivir (GS-5734) as a therapeutic option of 2019-nCOV main protease—In silico approach. *J. Biomol. Struct. Dyn.* **2021**, *39*, 4701–4714. [CrossRef] [PubMed]

9. Varikasuvu, S.R.; Thangappazham, B.; Vykunta, A.; Duggina, P.; Manne, M.; Raj, H.; Aloori, S. COVID-19 and vitamin D (Co-VIVID study): A systematic review and meta-analysis of randomized controlled trials. *Expert Rev. Anti-Infect. Ther.* **2022**, *20*, 907–913. [CrossRef] [PubMed]
10. Hardt, K.; Vandebosch, A.; Sadoff, J.; Le Gars, M.; Truyers, C.; Lowson, D.; Van Dromme, I.; Vingerhoets, J.; Kamphuis, T.; Scheper, G.; et al. ENSEMBLE2 study group Efficacy, safety, and immunogenicity of a booster regimen of Ad26.COV2.S vaccine against COVID-19 (ENSEMBLE2): Results of a randomised, double-blind, placebo-controlled, phase 3 trial. *Lancet. Infect. Dis.* **2022**, *22*, 1703–1715. Erratum in *Lancet Infect. Dis.* **2023**, *23*, e1. https://doi.org/10.1016/S1473-3099(22)00739-3. [CrossRef] [PubMed]
11. Jaishwal, P.; Jha, K.; Singh, S.P. Revisiting the dimensions of universal vaccine with special focus on COVID-19: Efficacy versus methods of designing. *Int. J. Biol. Macromol.* **2024**, *277*, 134012. [CrossRef] [PubMed]
12. Kim, J.H.; Marks, F.; Clemens, J.D. Looking beyond COVID-19 vaccine phase 3 trials. *Nat. Med.* **2021**, *27*, 205–211. [CrossRef] [PubMed]
13. Mahase, E. COVID-19: Novavax vaccine efficacy is 86% against UK variant and 60% against South African variant. *BMJ* **2021**, *372*, n296. [CrossRef] [PubMed]
14. Cromer, D.; Steain, M.; Reynaldi, A.; Schlub, T.E.; Khan, S.R.; Sasson, S.C.; Kent, S.J.; Khoury, D.S.; Davenport, M.P. Predicting vaccine effectiveness against severe COVID-19 over time and against variants: A meta-analysis. *Nat. Commun.* **2023**, *14*, 1633. [CrossRef] [PubMed]
15. Burton, D.R.; Topol, E.J. Variant-proof vaccines—Invest now for the next pandemic. *Nature* **2021**, *590*, 386–388. [CrossRef] [PubMed]
16. Chukwudozie, O.S.; Gray, C.M.; Fagbayi, T.A.; Chukwuanukwu, R.C.; Oyebanji, V.O.; Bankole, T.T.; Adewole, R.A.; Daniel, E.M. Immuno-informatics design of a multimeric epitope peptide-based vaccine targeting SARS-CoV-2 spike glycoprotein. *PLoS ONE* **2021**, *16*, e0248061. [CrossRef] [PubMed]
17. Ayyagari, V.S.; Venkateswarulu, T.C.; Abraham, P.K.; Srirama, K. Design of a multi-epitope-based vaccine targeting M-protein of SARS-CoV-2: An immunoinformatics approach. *J. Biomol. Struct. Dyn.* **2020**, *40*, 2963–2977. [PubMed]
18. Kumar, J.; Qureshi, R.; Sagurthi, S.R.; Qureshi, I.A. Designing of nucleocapsid protein based novel multi-epitope vaccine against SARS-CoV-2 using immunoinformatics approach. *Int. J. Pept. Res. Ther.* **2021**, *27*, 941–956. [PubMed]
19. Mahapatra, S.R.; Sahoo, S.; Dehury, B.; Raina, V.; Patro, S.; Misra, N.; Suar, M. Designing an efficient multi-epitope vaccine displaying interactions with diverse HLA molecules for an efficient humoral and cellular immune response to prevent COVID-19 infection. *Expert Rev. Vaccines* **2020**, *19*, 871–885. [CrossRef] [PubMed]
20. Tahir ul Qamar, M.; Rehman, A.; Tusleem, K.; Ashfaq, U.A.; Qasim, M.; Zhu, X.; Fatima, I.; Shahid, F.; Chen, L.-L. Designing of a next generation multiepitope-based vaccine (MEV) against SARS-CoV-2: Immunoinformatics and in silico approaches. *PLoS ONE* **2020**, *15*, e0244176. [CrossRef] [PubMed]
21. Dong, R.; Chu, Z.; Yu, F.; Zha, Y. Contriving multi-epitope subunit vaccine for COVID-19: Immunoinformatics approaches. *Front. Immunol.* **2020**, *11*, 1784. [PubMed]
22. Singh, A.; Thakur, M.; Sharma, L.K.; Chandra, K. Designing a multi-epitope peptide-based vaccine against SARS-CoV-2. *Sci. Rep.* **2020**, *10*, 16219. [CrossRef]
23. Prakash, S.; Dhanushkodi, N.R.; Zayou, L.; Ibraim, I.C.; Quadiri, A.; Coulon, P.G.; Tifrea, D.F.; Suzer, B.; Shaik, A.M.; Chilukuri, A.; et al. Cross-protection induced by highly conserved human B, CD4+, and CD8+ T-cell epitopes-based vaccine against severe infection, disease, and death caused by multiple SARS-CoV-2 variants of concern. *Front. Immunol.* **2024**, *15*, 1328905. [PubMed]
24. Vahed, H.; Prakash, S.; Quadiri, A.; Ibraim, I.C.; Omorogieva, E.; Patel, S.; Tadros, J.; Liao, E.J.; Lau, L.; Chentoufi, A.A.; et al. A pan-beta-coronavirus vaccine bearing conserved and asymptomatic B- and T-cell epitopes protects against highly pathogenic Delta and highly transmissible Omicron SARS-CoV-2 variants. *Hum. Vaccines Immunother.* **2025**, *21*, 2527438. [CrossRef] [PubMed]
25. Haltaufderhyde, K.; Gutiérrez, A.H.; McAllister, M.; Boyle, C.M.; Moise, L.; Martin, W.; De Groot, A.S. T-cell responses to highly conserved SARS-CoV-2 epitopes in Hispanic Americans receiving an mRNA COVID-19 vaccine. *Hum. Vaccin. Immunother.* **2025**, *21*, 2501844. [CrossRef] [PubMed]
26. Yang, K.; Zeng, Y.; Wu, X.; Li, J.; Guo, J. Strategies for developing self-assembled nanoparticle vaccines against SARS-CoV-2 infection. *Front. Immunol.* **2024**, *15*, 1392898. [CrossRef] [PubMed]
27. Wang, C.Y.; Peng, W.J.; Kuo, B.S.; Ho, Y.H.; Wang, M.S.; Yang, Y.T.; Chang, P.Y.; Shen, Y.H.; Hwang, K.P. Toward a pan-SARS-CoV-2 vaccine targeting conserved epitopes on spike and non-spike proteins for potent, broad and durable immune responses. *PLoS Pathog.* **2023**, *19*, e1010870. [CrossRef] [PubMed]
28. Swadling, L.; Maini, M.K. T cells in COVID-19—United in diversity. *Nat. Immunol.* **2020**, *21*, 1307–1308. [CrossRef] [PubMed]
29. Peng, Y.; Mentzer, A.J.; Liu, G.; Yao, X.; Yin, Z.; Dong, D.; Dejnirattisai, W.; Rostron, T.; Supasa, P.; Liu, C.; et al. Broad and strong memory CD4+ and CD8+ T cells induced by SARS-CoV-2 in UK convalescent individuals following COVID-19. *Nat. Immunol.* **2020**, *21*, 1336–1345. [CrossRef] [PubMed]
30. Deng, H.; Li, Y.; Wang, G.; Li, R. Comprehensive analysis of the immune response to SARS-CoV-2 epitopes: Unveiling potential targets for vaccine development. *Biology* **2025**, *14*, 67. [CrossRef] [PubMed]

31. He, Q.; Zhang, Y.; Fu, Z.; Ma, X.; Liang, Z. Broad-spectrum coronavirus vaccines: Integrated strategies to combat viral diversity. *Expert Rev. Vaccines* **2025**, *24*, 726–737. [CrossRef] [PubMed]
32. Parihar, A.; Malviya, S.; Khan, R. Immunoinformatics and reverse vaccinomic approaches for effective design. In *Computational Approaches for Novel Therapeutic and Diagnostic Designing to Mitigate SARS-CoV-2*; Springer: Berlin/Heidelberg, Germany, 2022; pp. 357–378. [CrossRef]
33. Weijzen, S.; Meredith, S.C.; Velders, M.P.; Elmishad, A.G.; Schreiber, H.; Kast, W.M. Pharmacokinetic differences between a T cell-tolerizing and a T cell-activating peptide. *J. Immunol.* **2001**, *166*, 7151–7157. [CrossRef] [PubMed]
34. Mehta, N.K.; Moynihan, K.D.; Irvine, D.J. Engineering New Approaches to Cancer Vaccines. *Cancer Immunol. Res.* **2015**, *3*, 836–843. [CrossRef] [PubMed]
35. Chen, W.; Huang, L. Induction of cytotoxic T-lymphocytes and antitumor activity by a liposomal lipopeptide vaccine. *Mol. Pharm.* **2008**, *5*, 464–471. [CrossRef] [PubMed]
36. Negahdaripour, M.; Golkar, N.; Hajighahramani, N.; Kianpour, S.; Nezafat, N.; Ghasemi, Y. Harnessing self-assembled peptide nanoparticles in epitope vaccine design. *Biotechnol. Adv.* **2017**, *35*, 575–596. [CrossRef] [PubMed]
37. Jaishwal, P.; Singh, S.P. Computational Design of Next-Generation Universal Nanovaccine for COVID-19: A Self-Assembling Coiled-Coil Platform Approach. *Pept. Sci.* **2026**, *118*, e70026. [CrossRef]
38. Dhanda, S.K.; Vir, P.; Raghava, G.P.S. Designing of interferon-gamma inducing MHC class-II binders. *Biol. Direct* **2013**, *8*, 30. [CrossRef] [PubMed]
39. Nagpal, G.; Usmani, S.S.; Dhanda, S.K.; Kaur, H.; Singh, S.; Sharma, M.; Raghava, G.P. Computer-aided designing of immunosuppressive peptides based on IL-10 inducing potential. *Sci. Rep.* **2017**, *7*, 42851. [CrossRef] [PubMed]
40. Indelicato, G.; Wahome, N.; Ringler, P.; Müller, S.A.; Nieh, M.P.; Burkhard, P.; Twarock, R. Principles Governing the Self-Assembly of Coiled-Coil Protein Nanoparticles. *Biophys. J.* **2016**, *110*, 646–660. [CrossRef] [PubMed]
41. Raman, S.K.; Machaidze, G.; Lustig, A.; Olivieri, V.; Aebi, U.; Burkhard, P. Design of peptide nanoparticles using simple protein oligomerization domains. *Open Nanomed. J.* **2009**, *2*, 15–26. [CrossRef]
42. Schroeder, U.; Graff, A.; Buchmeier, S.; Rigler, P.; Silvan, U.; Tropel, D.; Jockusch, B.M.; Aebi, U.; Burkhard, P.; Schoenenberger, C.A. Peptide nanoparticles serve as a powerful platform for the immunogenic display of poorly antigenic actin determinants. *J. Mol. Biol.* **2009**, *386*, 1368–1381. [CrossRef] [PubMed]
43. Yang, Y.; Ringler, P.; Müller, S.A.; Burkhard, P. Optimizing the refolding conditions of self-assembling polypeptide nanoparticles that serve as repetitive antigen display systems. *J. Struct. Biol.* **2012**, *177*, 168–176. [CrossRef] [PubMed]
44. Pimentel, T.A.; Yan, Z.; Jeffers, S.A.; Holmes, K.V.; Hodges, R.S.; Burkhard, P. Peptide nanoparticles as novel immunogens: Design and analysis of a prototypic severe acute respiratory syndrome vaccine. *Chem. Biol. Drug Des.* **2009**, *73*, 53–61. [CrossRef] [PubMed]
45. Kaba, S.A.; Brando, C.; Guo, Q.; Mittelholzer, C.; Raman, S.; Tropel, D.; Aebi, U.; Burkhard, P.; Lanar, D.E. A nonadjuvanted polypeptide nanoparticle vaccine confers long-lasting protection against rodent malaria. *J. Immunol.* **2009**, *183*, 7268–7277. [CrossRef] [PubMed]
46. Babapoor, S.; Neef, T.; Mittelholzer, C.; Girshick, T.; Garmendia, A.; Shang, H.; Khan, M.I.; Burkhard, P. A Novel Vaccine Using Nanoparticle Platform to Present Immunogenic M2e against Avian Influenza Infection. *Influenza Res. Treat.* **2011**, *2011*, 126794. [CrossRef] [PubMed]
47. Kaba, S.A.; McCoy, M.E.; Doll, T.A.; Brando, C.; Guo, Q.; Dasgupta, D.; Yang, Y.; Mittelholzer, C.; Spaccapelo, R.; Crisanti, A.; et al. Protective antibody and CD8+ T-cell responses to the *Plasmodium falciparum* circumsporozoite protein induced by a nanoparticle vaccine. *PLoS ONE* **2012**, *7*, e48304. [CrossRef] [PubMed]
48. Wahome, N.; Pfeiffer, T.; Ambiel, I.; Yang, Y.; Keppler, O.T.; Bosch, V.; Burkhard, P. Conformation-specific display of 4E10 and 2F5 epitopes on self-assembling protein nanoparticles as a potential HIV vaccine. *Chem. Biol. Drug Des.* **2012**, *80*, 349–357. [CrossRef] [PubMed]
49. El Bissati, K.; Zhou, Y.; Dasgupta, D.; Cobb, D.; Dubey, J.P.; Burkhard, P.; Lanar, D.E.; McLeod, R. Effectiveness of a novel immunogenic nanoparticle platform for *Toxoplasma* peptide vaccine in HLA transgenic mice. *Vaccine* **2014**, *32*, 3243–3248. [CrossRef] [PubMed]
50. Karch, C.P.; Doll, T.A.P.F.; Paulillo, S.M.; Nebie, I.; Lanar, D.E.; Corradin, G.; Burkhard, P. The use of a *P. falciparum* specific coiled-coil domain to construct a self-assembling protein nanoparticle vaccine to prevent malaria. *J. Nanobiotechnol.* **2017**, *15*, 62. [CrossRef] [PubMed]
51. Yu, M.; Zhu, Y.; Li, Y.; Chen, Z.; Li, Z.; Wang, J.; Li, Z.; Zhang, F.; Ding, J. Design of a Recombinant Multivalent Epitope Vaccine Based on SARS-CoV-2 and Its Variants in Immunoinformatics Approaches. *Front. Immunol.* **2022**, *13*, 884433. [CrossRef] [PubMed]
52. Ko, J.; Park, H.; Seok, C. GalaxyTBM: Template-based modeling by building a reliable core and refining unreliable local regions. *BMC Bioinform.* **2012**, *13*, 198. [CrossRef] [PubMed]
53. Lee, G.R.; Won, J.; Heo, L.; Seok, C. GalaxyRefine2: Simultaneous refinement of inaccurate local regions and overall protein structure. *Nucleic Acids Res.* **2019**, *47*, W451–W455. [CrossRef] [PubMed]

54. Wiederstein, M.; Sippl, M.J. ProSA-web: Interactive web service for the recognition of errors in three-dimensional structures of proteins. *Nucleic Acids Res.* **2007**, *35*, W407–W410. [CrossRef] [PubMed]
55. Baek, M.; Park, T.; Heo, L.; Park, C.; Seok, C. GalaxyHomomer: A web server for protein homo-oligomer structure prediction from a monomer sequence or structure. *Nucleic Acids Res.* **2017**, *45*, W320–W324. [CrossRef] [PubMed]
56. Cagiada, M.; Ovchinnikov, S.; Lindorff-Larsen, K. Predicting absolute protein folding stability using generative models. *Protein Sci.* **2025**, *34*, e5233. [CrossRef] [PubMed]
57. Kringelum, J.V.; Lundegaard, C.; Lund, O.; Nielsen, M. Reliable B cell epitope predictions: Impacts of method development and improved benchmarking. *PLoS Comput. Biol.* **2012**, *8*, e1002829. [CrossRef] [PubMed]
58. Wang, Y.; Zhang, Z.; Yang, M.; Xiong, X.; Yan, Q.; Cao, L.; Wei, P.; Zhang, Y.; Zhang, L.; Lv, K.; et al. Identification of a broad sarbecovirus neutralizing antibody targeting a conserved epitope on the receptor-binding domain. *Cell Rep.* **2024**, *43*, 113653. [CrossRef] [PubMed]
59. Yang, Y.X.; Huang, J.Y.; Wang, P.; Zhu, B.T. AREA-AFFINITY: An academic free web server for machine learning-based prediction of protein–protein and antibody–protein antigen binding affinities. *J. Chem. Inf. Model.* **2023**, *63*, 3230–3237. [CrossRef] [PubMed]
60. Walker, M.R.; Underwood, A.; Björnsson, K.H.; Raghavan, S.S.R.; Bassi, M.R.; Binderup, A.; Pham, L.V.; Ramirez, S.; Pinholt, M.; Dagil, R.; et al. Broadly potent spike-specific human monoclonal antibodies inhibit SARS-CoV-2 Omicron sub-lineages. *Commun. Biol.* **2024**, *7*, 1239. [CrossRef] [PubMed]
61. Chen, Y.; Zhao, X.; Zhou, H.; Zhu, H.; Jiang, S.; Wang, P. Broadly neutralizing antibodies to SARS-CoV-2 and other human coronaviruses. *Nat. Rev. Immunol.* **2023**, *23*, 189–199. [CrossRef] [PubMed]
62. Huang, Y.; Zhang, Z.; Zhou, Y. AbAgIntPre: A deep learning method for predicting antibody-antigen interactions based on sequence information. *Front. Immunol.* **2022**, *13*, 1053617. [CrossRef] [PubMed]
63. Wang, S.; Wang, C.Y.; Kuo, H.-K.; Peng, W.-J.; Huang, J.-H.; Kuo, B.-S.; Lin, F.; Liu, Y.-J.; Liu, Z.; Wu, H.-T.; et al. A novel RBD-protein/peptide vaccine elicits broadly neutralizing antibodies and protects mice and macaques against SARS-CoV-2. *Emerg. Microbes Infect.* **2022**, *11*, 2724–2734. [CrossRef] [PubMed]
64. Nain, Z.; Abdullah, F.; Rahman, M.M.; Karim, M.M.; Khan, S.A.; Bin Sayed, S.; Mahmud, S.; Rahman, S.M.R.; Sheam, M.; Haque, Z.; et al. Proteome-wide screening for designing a multi-epitope vaccine against emerging pathogen *Elizabethkingia anophelis* using immunoinformatic approaches. *J. Biomol. Struct. Dyn.* **2020**, *38*, 4850–4867. [CrossRef] [PubMed]
65. Bhatnager, R.; Bhasin, M.; Arora, J.; Dang, A.S. Epitope-based peptide vaccine against SARS-CoV-2: An immune-informatics approach. *J. Biomol. Struct. Dyn.* **2021**, *39*, 5690–5705. [CrossRef] [PubMed]
66. Grote, A.; Hiller, K.; Scheer, M.; Münch, R.; Nörtemann, B.; Hempel, D.C.; Jahn, D. JCat: A novel tool to adapt codon usage of a target gene to its potential expression host. *Nucleic Acids Res.* **2005**, *33*, W526–W531. [CrossRef] [PubMed]
67. Pandey, R.K.; Ojha, R.; Aathmanathan, V.S.; Krishnan, M.; Prajapati, V.K. Immunoinformatics approaches to design a novel multiepitope subunit vaccine against HIV infection. *Vaccine* **2018**, *36*, 2262–2272. [CrossRef] [PubMed]
68. Marrama, D.; Chronister, W.D.; Westernberg, L.; Vita, R.; Koşaloğlu-Yalçın, Z.; Sette, A.; Nielsen, M.; Greenbaum, J.A.; Peters, B. PEPMatch: A tool to identify short peptide sequence matches in large sets of proteins. *BMC Bioinform.* **2023**, *24*, 485. [CrossRef] [PubMed]
69. Bui, H.H.; Sidney, J.; Dinh, K.; Southwood, S.; Newman, M.J.; Sette, A. Predicting population coverage of T-cell epitope-based diagnostics and vaccines. *BMC Bioinform.* **2006**, *7*, 153. [CrossRef] [PubMed]
70. Pritam, M.; Singh, G.; Swaroop, S.; Singh, A.K.; Singh, S.P. Exploitation of reverse vaccinology and immunoinformatics as promising platform for genome-wide screening of new effective vaccine candidates against *Plasmodium falciparum*. *BMC Bioinform.* **2019**, *19*, 468. [CrossRef] [PubMed]
71. Gutman, I.; Gutman, R.; Sidney, J.; Chihab, L.; Mishto, M.; Liepe, J.; Chiem, A.; Greenbaum, J.; Yan, Z.; Sette, A.; et al. Predicting the Success of Fmoc-Based Peptide Synthesis. *ACS Omega* **2022**, *7*, 23771–23781. [CrossRef] [PubMed]
72. Dos Santos Alves, R.P.; Timis, J.; Miller, R.; Valentine, K.; Pinto, P.B.A.; Gonzalez, A.; Regla-Nava, J.A.; Maule, E.; Nguyen, M.N.; Shafee, N.; et al. Human coronavirus OC43-elicited CD4+ T cells protect against SARS-CoV-2 in HLA transgenic mice. *Nat. Commun.* **2024**, *15*, 787. [CrossRef] [PubMed]
73. Fleri, W.; Paul, S.; Dhanda, S.K.; Mahajan, S.; Xu, X.; Peters, B.; Sette, A. The Immune Epitope Database and Analysis Resource in epitope discovery and synthetic vaccine design. *Front. Immunol.* **2017**, *8*, 278. [CrossRef] [PubMed]
74. Wei, Y.; Qiu, T.; Ai, Y.; Zhang, Y.; Xie, J.; Zhang, D.; Luo, X.; Sun, X.; Wang, X.; Qiu, J. Advances of computational methods enhance the development of multi-epitope vaccines. *Brief. Bioinform.* **2024**, *26*, bbaf055. [CrossRef] [PubMed]
75. Tau, G.; Rothman, P. Biologic functions of the IFN-gamma receptors. *Allergy* **1999**, *54*, 1233–1251. [CrossRef] [PubMed]
76. Calis, J.J.; Maybeno, M.; Greenbaum, J.A.; Weiskopf, D.; De Silva, A.D.; Sette, A.; Keşmir, C.; Peters, B. Properties of MHC class I presented peptides that enhance immunogenicity. *PLoS Comput. Biol.* **2013**, *9*, e1003266. [CrossRef] [PubMed]
77. Dhanda, S.K.; Karosiene, E.; Edwards, L.; Grifoni, A.; Paul, S.; Andreatta, M.; Weiskopf, D.; Sidney, J.; Nielsen, M.; Peters, B.; et al. Predicting HLA CD4 immunogenicity in human populations. *Front. Immunol.* **2018**, *9*, 1369. [CrossRef] [PubMed]

78. Chronister, W.D.; Crinklaw, A.; Mahajan, S.; Vita, R.; Koşaloğlu-Yalçın, Z.; Yan, Z.; Greenbaum, J.A.; Jessen, L.E.; Nielsen, M.; Christley, S.; et al. TCRMatch: Predicting T-cell receptor specificity based on sequence similarity to previously characterized receptors. *Front. Immunol.* **2021**, *12*, 640725. [CrossRef] [PubMed]
79. Udyavar, A.; Alli, R.; Nguyen, P.; Baker, L.; Geiger, T.L. Subtle affinity-enhancing mutations in a myelin oligodendrocyte glycoprotein-specific TCR alter specificity and generate new self-reactivity. *J. Immunol.* **2009**, *182*, 4439–4447. [CrossRef] [PubMed]
80. Chaisawangwong, W.; Wang, H.; Kouo, T.; Salathe, S.F.; Isser, A.; Bieler, J.G.; Zhang, M.L.; Livingston, N.K.; Li, S.; Horowitz, J.J.; et al. Cross-reactivity of SARS-CoV-2- and influenza A-specific T cells in individuals exposed to SARS-CoV-2. *JCI Insight* **2022**, *7*, e158308. [CrossRef] [PubMed]
81. Zhou, D.; Luo, Y.; Ma, Q.; Xu, Y.; Yao, X. The characteristics of TCR CDR3 repertoire in COVID-19 patients and SARS-CoV-2 vaccine recipients. *Virulence* **2024**, *15*, 2421987. [CrossRef] [PubMed]
82. Higgins, J.P.; Soares-Weiser, K.; López-López, J.A.; Kakourou, A.; Chaplin, K.; Christensen, H.; Martin, N.K.; Sterne, J.A.; Reingold, A.L. Association of BCG, DTP, and measles containing vaccines with childhood mortality: Systematic review. *BMJ* **2016**, *355*, i5170. Erratum in *BMJ* **2017**, *356*, j1171. https://doi.org/10.1136/bmj.j1171. [CrossRef] [PubMed]
83. Ristori, G.; Faustman, D.; Matarese, G.; Romano, S.; Salvetti, M. Bridging the gap between vaccination with Bacille Calmette-Guérin (BCG) and immunological tolerance: The cases of type 1 diabetes and multiple sclerosis. *Curr. Opin. Immunol.* **2018**, *55*, 89–96. [CrossRef] [PubMed]
84. Cankat, S.; Demael, M.U.; Swadling, L. In search of a pan-coronavirus vaccine: Next-generation vaccine design and immune mechanisms. *Cell. Mol. Immunol.* **2024**, *21*, 103–118. [CrossRef] [PubMed]
85. Singh, G.; Pritam, M.; Banerjee, M.; Singh, A.K.; Singh, S.P. Designing of precise vaccine construct against visceral leishmaniasis through predicted epitope ensemble: A contemporary approach. *Comput. Biol. Chem.* **2020**, *86*, 107259. [CrossRef] [PubMed]
86. Yu, K.; Liu, C.; Kim, B.G.; Lee, D.Y. Synthetic fusion protein design and applications. *Biotechnol. Adv.* **2015**, *33*, 155–164. [CrossRef] [PubMed]
87. Nezafat, N.; Ghasemi, Y.; Javadi, G.; Khoshnoud, M.J.; Omidinia, E. A novel multi-epitope peptide vaccine against cancer: An in silico approach. *Theor. Biol. Med. Model.* **2014**, *349*, 121–134. [CrossRef] [PubMed]
88. Jespersen, M.C.; Peters, B.; Nielsen, M.; Marcatili, P. BepiPred-2.0: Improving sequence-based B-cell epitope prediction using conformational epitopes. *Nucleic Acids Res.* **2017**, *45*, W24–W29. [CrossRef] [PubMed]
89. Barh, D.; Misra, A.N.; Kumar, A.; Azevedo, V. A novel strategy of epitope design in *Neisseria gonorrhoeae*. *Bioinformation* **2010**, *5*, 77–82. [CrossRef] [PubMed]
90. Mohan, T.; Sharma, C.; Bhat, A.A.; Rao, D.N. Modulation of HIV peptide antigen specific cellular immune response by synthetic α-and β-defensin peptides. *Vaccine* **2013**, *31*, 1707–1716. [CrossRef] [PubMed]
91. Frankel, A.D.; Pabo, C.O. Cellular uptake of the tat protein from human immunodeficiency virus. *Cell* **1988**, *55*, 1189–1193. [CrossRef] [PubMed]
92. Bertoline, L.M.F.; Lima, A.N.; Krieger, J.E.; Teixeira, S.K. Before and after AlphaFold2: An overview of protein structure prediction. *Front. Bioinform.* **2023**, *3*, 1120370. [CrossRef] [PubMed]
93. Abramson, J.; Adler, J.; Dunger, J.; Evans, R.; Green, T.; Pritzel, A.; Ronneberger, O.; Willmore, L.; Ballard, A.J.; Bambrick, J.; et al. Accurate structure prediction of biomolecular interactions with AlphaFold 3. *Nature* **2024**, *630*, 493–500. [CrossRef] [PubMed]
94. Vedula, S.; Bronstein, A.M.; Marx, A. Improving prediction accuracy in chimeric proteins with windowed multiple sequence alignment. *Comput. Struct. Biotechnol. J.* **2025**, *27*, 3292–3298. [CrossRef] [PubMed]
95. Colovos, C.; Yeates, T.O. Verification of protein structures: Patterns of nonbonded atomic interactions. *Protein Sci. A Publ. Protein Soc.* **1993**, *2*, 1511–1519. [CrossRef] [PubMed]
96. Heo, L.; Park, H.; Seok, C. GalaxyRefine: Protein structure refinement driven by side-chain repacking. *Nucleic Acids Res.* **2013**, *41*, W384–W388. [CrossRef] [PubMed]
97. Zemla, A. LGA: A method for finding 3D similarities in protein structures. *Nucleic Acids Res.* **2003**, *31*, 3370–3374. [CrossRef] [PubMed]
98. Chen, V.B.; Arendall, W.B.; Headd, J.J.; Keedy, D.A.; Immormino, R.M.; Kapral, G.J.; Murray, L.W.; Richardson, J.S.; Richardson, D.C. MolProbity: All-atom structure validation for macromolecular crystallography. *Acta Crystallogr. Sect. D Biol. Crystallogr.* **2010**, *66*, 12–21. [CrossRef] [PubMed]
99. Vakili, B.; Nezafat, N.; Negahdaripour, M.; Ghasemi, Y. A structural vaccinology approach for in silico designing of a potential self-assembled nanovaccine against Leishmania infantum. *Exp. Parasitol.* **2022**, *239*, 108295. [CrossRef] [PubMed]
100. Dorosti, H.; Eslami, M.; Nezafat, N.; Fadaei, F.; Ghasemi, Y. Designing self-assembled peptide nanovaccine against Streptococcus pneumoniae: An in silico strategy. *Mol. Cell. Probes* **2019**, *48*, 101446. [CrossRef] [PubMed]
101. Gaber, A.; Pavšič, M. Modeling and structure determination of homo-oligomeric proteins: An overview of challenges and current approaches. *Int. J. Mol. Sci.* **2021**, *22*, 9081. [CrossRef] [PubMed]

102. Omidi, A.; Bui, J.M.; Gsponer, J. Predicting protein interfaces in the age of AlphaFold: Why dynamics and disorder remain a challenge. *Cell Syst.* **2026**, *17*, 101508. [CrossRef] [PubMed]
103. Omidi, A.; Møller, M.H.; Malhis, N.; Bui, J.M.; Gsponer, J. AlphaFold-Multimer accurately captures interactions and dynamics of intrinsically disordered protein regions. *Proc. Natl. Acad. Sci. USA* **2024**, *121*, e2406407121. [CrossRef] [PubMed]
104. Zhu, W.; Shenoy, A.; Kundrotas, P.; Elofsson, A. Evaluation of AlphaFold-Multimer prediction on multi-chain protein complexes. *Bioinformatics* **2023**, *39*, btad424. [CrossRef] [PubMed]
105. Lu, D.; Yu, S.; Huang, Y.; Gong, X. Multimeric protein interaction and complex prediction: Structure, dynamics and function. *Comput. Struct. Biotechnol. J.* **2025**, *27*, 1975–1997. [CrossRef] [PubMed]
106. Weeratunga, S.; Gormal, R.S.; Liu, M.; Eldershaw, D.; Livingstone, E.K.; Malapaka, A.; Wallis, T.P.; Bademosi, A.T.; Jiang, A.; Healy, M.D.; et al. Interrogation and validation of the interactome of neuronal Munc18-interacting Mint proteins with AlphaFold2. *J. Biol. Chem.* **2024**, *300*, 105541. [CrossRef] [PubMed]
107. Raman, S.; Machaidze, G.; Lustig, A.; Aebi, U.; Burkhard, P. Structure-based design of peptides that self-assemble into regular polyhedral nanoparticles. *Nanomed. Nanotechnol. Biol. Med.* **2006**, *2*, 95–102. [CrossRef] [PubMed]
108. Doll, T.A.P.F.; Raman, S.; Dey, R.; Burkhard, P. Optimizing the design of protein nanoparticles as carriers for vaccine applications. *Nanomedicine* **2015**, *11*, 1705–1713. [CrossRef] [PubMed]
109. Sanchez-Trincado, J.L.; Gomez-Perosanz, M.; Reche, P.A. Fundamentals and Methods for T- and B-Cell Epitope Prediction. *J. Immunol. Res.* **2017**, *2017*, 2680160. [CrossRef] [PubMed]
110. Khatoon, N.; Pandey, R.K.; Prajapati, V.K. Exploring Leishmania secretory proteins to design B and T cell multi-epitope subunit vaccine using immunoinformatics approach. *Sci. Rep.* **2017**, *7*, 8285. [CrossRef] [PubMed]
111. Walker, J.M. *The Proteomics Protocols Handbook*; Springer: New York, NY, USA, 2005.
112. Nwachukwu, I.D.; Aluko, R.E. Structural and functional properties of food protein-derived antioxidant peptides. *J. Food Biochem.* **2019**, *43*, e12761. [CrossRef] [PubMed]
113. Kar, T.; Narsaria, U.; Basak, S.; Deb, D.; Castiglione, F.; Mueller, D.M.; Srivastava, A.P. A candidate multi-epitope vaccine against SARS-CoV-2. *Sci. Rep.* **2020**, *10*, 10895. [CrossRef] [PubMed]
114. Arduini, A.; Laprise, F.; Liang, C. SARS-CoV-2 ORF8: A rapidly evolving immune and viral modulator in COVID-19. *Viruses* **2023**, *15*, 871. [CrossRef] [PubMed]
115. Wang, X.; Lam, J.Y.; Wong, W.M.; Yuen, C.K.; Cai, J.P.; Au, S.W.; Chan, J.F.; To, K.K.W.; Kok, K.H.; Yuen, K.Y. Accurate diagnosis of COVID-19 by a novel immunogenic secreted SARS-CoV-2 ORF8 protein. *mBio* **2020**, *11*, e02431–20. [CrossRef] [PubMed]
116. Hachim, A.; Kavian, N.; Cohen, C.A.; Chin, A.W.H.; Chu, D.K.W.; Mok, C.K.P.; Tsang, O.T.Y.; Yeung, Y.C.; Perera, R.A.P.M.; Poon, L.L.M.; et al. ORF8 and ORF3b antibodies are accurate serological markers of early and late SARS-CoV-2 infection. *Nat. Immunol.* **2020**, *21*, 1293–1301. Erratum in *Nat. Immunol.* **2020**, *21*, 1302. https://doi.org/10.1038/s41590-020-0788-0. [CrossRef] [PubMed]
117. Sela-Culang, I.; Kunik, V.; Ofran, Y. The structural basis of antibody-antigen recognition. *Front. Immunol.* **2013**, *4*, 302. [CrossRef] [PubMed]
118. Peng, H.P.; Lee, K.H.; Jian, J.W.; Yang, A.S. Origins of specificity and affinity in antibody-protein interactions. *Proc. Natl. Acad. Sci. USA* **2014**, *111*, E2656–E2665. [CrossRef] [PubMed]
119. Yin, R.; Feng, B.Y.; Varshney, A.; Pierce, B.G. Benchmarking AlphaFold for protein complex modeling reveals accuracy determinants. *Protein Sci.* **2022**, *31*, e4379. [CrossRef] [PubMed]
120. Li, M.Q.C.; Wang, S.; Lin, S.-R.; Ting, L.E.N.; Wan, Z.-H.; Xie, G.; Zhang, J. Advantages and limitations of AlphaFold in structural biology: Insights from recent studies. *Protein J.* **2025**. [CrossRef] [PubMed]
121. Hitawala, F.N.; Gray, J.J. What does AlphaFold3 learn about antibody and nanobody docking, and what remains unsolved? *mAbs* **2025**, *17*, 2545601. [CrossRef] [PubMed]
122. Guest, J.D.; Vreven, T.; Zhou, J.; Moal, I.; Jeliazkov, J.R.; Gray, J.J.; Weng, Z.; Pierce, B.G. An expanded benchmark for antibody–antigen docking and affinity prediction reveals insights into antibody recognition determinants. *Structure* **2021**, *29*, 606–621.e5. [CrossRef] [PubMed]
123. Desta, I.T.; Kotelnikov, S.; Jones, G.; Ghani, U.; Abyzov, M.; Kholodov, Y.; Standley, D.M.; Beglov, D.; Vajda, S.; Kozakov, D. The ClusPro AbEMap web server for the prediction of antibody epitopes. *Nat. Protoc.* **2023**, *18*, 1814–1840. [CrossRef] [PubMed]
124. McCoy, K.M.; Ackerman, M.E.; Grigoryan, G. A comparison of antibody–antigen complex sequence-to-structure prediction methods and their systematic biases. *Protein Sci.* **2024**, *33*, e5127. [CrossRef] [PubMed]
125. Ghosh, T.; Garde, S.; García, A.E. Role of backbone hydration and salt-bridge formation in stability of α-helix in solution. *Biophys. J.* **2003**, *85*, 3187–3193. [CrossRef] [PubMed]
126. Donald, J.E.; Kulp, D.W.; DeGrado, W.F. Salt bridges: Geometrically specific, designable interactions. *Proteins Struct. Funct. Bioinform.* **2010**, *79*, 898–915. [CrossRef] [PubMed]
127. Meuzelaar, H.; Vreede, J.; Woutersen, S. Influence of Glu/Arg, Asp/Arg, and Glu/Lys salt bridges on α-helical stability and folding kinetics. *Biophys. J.* **2016**, *110*, 2328–2341. [CrossRef] [PubMed]

128. Khudozhitkov, E.; Neumann, J.; Niemann, T.; Zaitsau, D.; Stange, P.; Paschek, D.; Stepanov, A.G.; Kolokolov, D.I.; Ludwig, R. Hydrogen Bonding Between Ions of Like Charge in Ionic Liquids Characterized by NMR Deuteron Quadrupole Coupling Constants—Comparison with Salt Bridges and Molecular Systems. *Angew. Chem. Int. Ed.* **2019**, *58*, 17863–17871. [CrossRef] [PubMed]
129. Xu, D.; Tsai, C.J.; Nussinov, R. Hydrogen bonds and salt bridges across protein-protein interfaces. *Protein Eng.* **1997**, *10*, 999–1012. [CrossRef] [PubMed]
130. Yang, Y.X.; Wang, P.; Zhu, B.T. Binding affinity prediction for antibody–protein antigen complexes: A machine learning analysis based on interface and surface areas. *J. Mol. Graph. Model.* **2023**, *118*, 108364. [CrossRef] [PubMed]
131. Zothantluanga, J.H.; Chetia, D. A beginner's guide to molecular docking. *Sci. Phytochem.* **2022**, *1*, 37–40. [CrossRef]
132. Kozakov, D.; Hall, D.R.; Xia, B.; Porter, K.A.; Padhorny, D.; Yueh, C.; Beglov, D.; Vajda, S. The ClusPro web server for protein–protein docking. *Nat. Protoc.* **2017**, *12*, 255–278. [CrossRef] [PubMed]
133. Dauzhenka, T.; Kundrotas, P.J.; Vakser, I.A. Computational Feasibility of an Exhaustive Search of Side-Chain Conformations in Protein-Protein Docking. *J. Comput. Chem.* **2018**, *39*, 2012–2021. [CrossRef] [PubMed]
134. Chakravarty, D.; Lee, M.; Porter, L.L. Proteins with alternative folds reveal blind spots in AlphaFold-based protein structure prediction. *Curr. Opin. Struct. Biol.* **2025**, *90*, 102973. [CrossRef] [PubMed]
135. Karplus, M.; McCammon, J.A. Molecular dynamics simulations of biomolecules. *Nat. Struct. Biol.* **2002**, *9*, 646–652. Erratum in *Nat. Struct. Biol.* **2002**, *9*, 738. https://doi.org/10.1038/nsb1002-738b. [CrossRef] [PubMed]
136. Kalimuthu, A.K.; Panneerselvam, T.; Pavadai, P.; Pandian, S.R.K.; Sundar, K.; Murugesan, S.; Ammunje, D.N.; Kumar, S.; Arunachalam, S.; Kunjiappan, S. Pharmacoinformatics-based investigation of bioactive compounds of Rasam (South Indian recipe) against human cancer. *Sci. Rep.* **2021**, *11*, 21488. [CrossRef] [PubMed]
137. Rantam, F.A.; Kharisma, V.D.; Sumartono, C.; Nugraha, J.; Wijaya, A.Y.; Susilowati, H.; Kuncorojakti, S.; Nugraha, A.P. Molecular docking and dynamic simulation of conserved B cell epitope of SARS-CoV-2 glycoprotein Indonesian isolates: An immunoinformatic approach. *F1000Research* **2021**, *10*, 813. [CrossRef] [PubMed]
138. Sami, S.A.; Marma, K.K.S.; Mahmud, S.; Khan, A.N.; Albogami, S.; El-Shehawi, A.M.; Rakib, A.; Chakraborty, A.; Mohiuddin, M.; Dhama, K.; et al. Designing of a multi-epitope vaccine against the structural proteins of Marburg virus exploiting the immunoinformatics approach. *ACS Omega* **2021**, *6*, 32043–32071. [CrossRef] [PubMed]
139. Gorai, S.; Junghare, V.; Kundu, K.; Gharui, S.; Kumar, M.; Patro, B.S.; Nayak, S.K.; Hazra, S.; Mula, S. Synthesis of dihydrobenzo furo [3, 2-b] chromenes as potential 3CLpro inhibitors of SARS-CoV-2: A molecular docking and molecular dynamics study. *ChemMedChem* **2022**, *17*, e202100782. [CrossRef] [PubMed]
140. Paul, S.K.; Saddam, M.; Rahaman, K.A.; Choi, J.G.; Lee, S.S.; Hasan, M. Molecular modeling, molecular dynamics simulation, and essential dynamics analysis of grancalcin: An upregulated biomarker in experimental autoimmune encephalomyelitis mice. *Heliyon* **2022**, *8*, e11232. [CrossRef] [PubMed]
141. Sahil, M.; Sarkar, S.; Mondal, J. Long-time-step molecular dynamics can retard simulation of protein–ligand recognition process. *Biophys. J.* **2023**, *122*, 802–816. [CrossRef] [PubMed]
142. Hollingsworth, S.A.; Dror, R.O. Molecular dynamics simulation for all. *Neuron* **2018**, *99*, 1129–1143. [CrossRef] [PubMed]
143. Rapin, N.; Lund, O.; Castiglione, F. Immune system simulation online. *Bioinformatics* **2011**, *27*, 2013–2014. [CrossRef] [PubMed]
144. Stolfi, P.; Castiglione, F.; Mastrostefano, E.; Di Biase, I.; Di Biase, S.; Palmieri, G.; Prisco, A. In-silico evaluation of adenoviral COVID-19 vaccination protocols: Assessment of immunological memory up to 6 months after the third dose. *Front. Immunol.* **2022**, *13*, 998262. [CrossRef] [PubMed]
145. Sanami, S.; Nazarian, S.; Ahmad, S.; Raeisi, E.; Tahir Ul Qamar, M.; Tahmasebian, S.; Pazoki-Toroudi, H.; Fazeli, M.; Ghatreh Samani, M. In silico design and immunoinformatics analysis of a universal multi-epitope vaccine against monkeypox virus. *PLoS ONE* **2023**, *18*, e0286224. [CrossRef] [PubMed]
146. Urrutia-Baca, V.H.; Gomez-Flores, R.; De La Garza-Ramos, M.A.; Tamez-Guerra, P.; Lucio-Sauceda, D.G.; Rodríguez-Padilla, M.C. Immunoinformatics approach to design a novel epitope-based oral vaccine against *Helicobacter pylori*. *J. Comput. Biol.* **2019**, *26*, 1177–1190. [CrossRef] [PubMed]
147. Foroutan, M.; Ghaffarifar, F.; Sharifi, Z.; Dalimi, A. Vaccination with a novel multi-epitope ROP8 DNA vaccine against acute Toxoplasma gondii infection induces strong B and T cell responses in mice. *Comp. Immunol. Microbiol. Infect. Dis.* **2020**, *69*, 101413. [CrossRef] [PubMed]
148. Hajissa, K.; Zakaria, R.; Suppian, R.; Mohamed, Z. Design and evaluation of a recombinant multi-epitope antigen for serodiagnosis of *Toxoplasma gondii* infection in humans. *Parasites Vectors* **2015**, *8*, 315. [CrossRef] [PubMed]
149. Liu, Q.; Li, J.; Li, R.L.; Ma, Y.T.; Zhou, P.L.; Gao, W.W.; Ma, H.L. Expression and immunoreactivity of a recombinant multi-epitope antigen designed based on four major structural proteins of avian infectious bronchitis virus. *3 Biotech* **2020**, *10*, 86. [CrossRef] [PubMed]

150. Zhang, H.; Yuan, X.; He, Y.; Chen, Y.; Hu, C.; Chen, J.; Zhang, L.; Chen, X.; Guo, A. A novel multiepitope fusion antigen as a vaccine candidate for the prevention of enterotoxigenic *Escherichia coli*-induced calf diarrhea. *Vaccines* **2024**, *12*, 457. [CrossRef] [PubMed]
151. Gonçalves, A.A.M.; Ribeiro, A.J.; Resende, C.A.A.; Couto, C.A.P.; Gandra, I.B.; Dos Santos Barcelos, I.C.; da Silva, J.O.; Machado, J.M.; Silva, K.A.; Silva, L.S.; et al. Recombinant multiepitope proteins expressed in *Escherichia coli* cells and their potential for immunodiagnosis. *Microb. Cell Fact.* **2024**, *23*, 145. [CrossRef] [PubMed]
152. Wang, G.; Qi, X.; Zhao, S.; Pei, Q.; Chen, Y.; Yin, D.; Zhan, T. Preparation of a Brucella multiepitope fusion protein based on bioinformatics and its application in serological diagnosis of human brucellosis. *Sci. Rep.* **2025**, *15*, 19106. [CrossRef] [PubMed]
153. Morse, J.S.; Lalonde, T.; Xu, S.; Liu, W.R. Learning from the Past: Possible Urgent Prevention and Treatment Options for Severe Acute Respiratory Infections Caused by 2019-nCoV. *Chembiochem A Eur. J. Chem. Biol.* **2020**, *21*, 730–738. [CrossRef] [PubMed]
154. Cao, Y.; Li, D.; Fu, Y.; Bai, Q.; Chen, Y.; Bai, X.; Jing, Z.; Sun, P.; Bao, H.; Li, P.; et al. Rational design and efficacy of a multi-epitope recombinant protein vaccine against foot-and-mouth disease virus serotype A in pigs. *Antivir. Res.* **2017**, *140*, 133–141. [CrossRef] [PubMed]
155. Jiang, P.; Cai, Y.; Chen, J.; Ye, X.; Mao, S.; Zhu, S.; Xue, X.; Chen, S.; Zhang, L. Evaluation of tandem Chlamydia trachomatis MOMP multi-epitopes vaccine in BALB/c mice model. *Vaccine* **2017**, *35*, 3096–3103. [CrossRef] [PubMed]
156. Slingluff, C.L., Jr.; Lee, S.; Zhao, F.; Chianese-Bullock, K.A.; Olson, W.C.; Butterfield, L.H.; Whiteside, T.L.; Leming, P.D.; Kirkwood, J.M. A randomized phase II trial of multiepitope vaccination with melanoma peptides for cytotoxic T cells and helper T cells for patients with metastatic melanoma (E1602). *Clin. Cancer Res. Off. J. Am. Assoc. Cancer Res.* **2013**, *19*, 4228–4238. [CrossRef] [PubMed]
157. Toledo, H.; Baly, A.; Castro, O.; Resik, S.; Laferté, J.; Rolo, F.; Navea, L.; Lobaina, L.; Cruz, O.; Míguez, J.; et al. A phase I clinical trial of a multi-epitope polypeptide TAB9 combined with Montanide ISA 720 adjuvant in non-HIV-1 infected human volunteers. *Vaccine* **2001**, *19*, 4328–4336. [CrossRef] [PubMed]
158. Chauhan, V.; Rungta, T.; Goyal, K.; Singh, M.P. Designing a multi-epitope-based vaccine to combat Kaposi Sarcoma utilizing immunoinformatics approach. *Sci. Rep.* **2019**, *9*, 2517. [CrossRef] [PubMed]
159. Zhang, L. Multi-epitope vaccines: A promising strategy against tumors and viral infections. *Cell. Mol. Immunol.* **2018**, *15*, 182–184. [CrossRef] [PubMed]
160. He, R.; Yang, X.; Liu, C.; Chen, X.; Wang, L.; Xiao, M.; Ye, J.; Wu, Y.; Ye, L. Efficient control of chronic LCMV infection by a CD4 T cell epitope-based heterologous prime-boost vaccination in a murine model. *Cell. Mol. Immunol.* **2018**, *15*, 815–826. [CrossRef] [PubMed]
161. Röcken, M.; Racke, M.; Shevach, E.M. IL-4-induced immune deviation as antigen-specific therapy for inflammatory autoimmune disease. *Immunol. Today* **1996**, *17*, 225–231. [PubMed]
162. Lubberts, E.; Joosten, L.A.B.; Chabaud, M.; Oppers, B.; Richards, C.D.; Miossec, P.; Van Den Berg, W.B. IL-4 gene therapy for collagen arthritis suppresses synovial IL-17 and osteoprotegerin ligand and prevents bone erosion. *J. Clin. Investig.* **2000**, *105*, 1697–1710. [CrossRef] [PubMed]
163. Ghoreschi, K.; Thomas, P.; Breit, S.; Dugas, M.; Mailhammer, R.; van Eden, W.; van der Zee, R.; Biedermann, T.; Prinz, J.; Mack, M.; et al. Interleukin-4 therapy of psoriasis induces Th2 responses and improves human autoimmune disease. *Nat. Med.* **2003**, *9*, 40–46. [CrossRef] [PubMed]
164. Kajiwara, A.; Doi, H.; Eguchi, J.; Ishii, S.; Hiraide-Sasagawa, A.; Sakaki, M.; Omori, R.; Hiroishi, K.; Imawari, M. Interleukin-4 and CpG oligonucleotide therapy suppress the outgrowth of tumors by activating tumor-specific Th1-type immune responses. *Oncol. Rep.* **2012**, *27*, 1765–1771. [PubMed]
165. Akdis, C.A.; Blaser, K. Mechanisms of interleukin-10-mediated immune suppression. *Immunology* **2001**, *103*, 131–136. [CrossRef] [PubMed]
166. Hawrylowicz, C.M.; O'Garra, A. Potential role of interleukin-10-secreting regulatory T cells in allergy and asthma. *Nat. Rev. Immunol.* **2005**, *5*, 271–283. [CrossRef] [PubMed]
167. Bromberg, J.S. IL-10 immunosuppression in transplantation. *Curr. Opin. Immunol.* **1995**, *7*, 639–643. [CrossRef] [PubMed]
168. Shinozaki, K.; Yahata, H.; Tanji, H.; Sakaguchi, T.; Ito, H.; Dohi, K. Allograft transduction of IL-10 prolongs survival following orthotopic liver transplantation. *Gene Ther.* **1999**, *6*, 816–822. [CrossRef] [PubMed]
169. Fiorentino, D.F.; Bond, M.W.; Mosmann, T.R. Two types of mouse T helper cell. IV. Th2 clones secrete a factor that inhibits cytokine production by Th1 clones. *J. Exp. Med.* **1989**, *170*, 2081–2095. [CrossRef] [PubMed]
170. Roncarolo, M.G.; Gregori, S.; Battaglia, M.; Bacchetta, R.; Fleischhauer, K.; Levings, M.K. Interleukin-10-secreting type 1 regulatory T cells in rodents and humans. *Immunol. Rev.* **2006**, *212*, 28–50. [CrossRef] [PubMed]
171. Biedermann, T.; Zimmermann, S.; Himmelrich, H.; Gumy, A.; Egeter, O.; Sakrauski, A.K.; Seegmüller, I.; Voigt, H.; Launois, P.; Levine, A.D.; et al. IL-4 instructs Th1 responses and resistance to *Leishmania major* in susceptible BALB/c mice. *Nat. Immunol.* **2001**, *2*, 1054–1060. [CrossRef] [PubMed]
172. Brown, M.A.; Hural, J. Functions of IL-4 and control of its expression. *Crit. Rev. Immunol.* **1997**, *17*, 1–32. [CrossRef] [PubMed]

173. Swain, S.L.; Weinberg, A.D.; English, M.; Huston, G. IL-4 directs the development of Th2-like helper effectors. *J. Immunol.* **1990**, *145*, 3796–3806. [CrossRef] [PubMed]
174. Porcelli, S.; Yockey, C.E.; Brenner, M.B.; Balk, S.P. Analysis of T cell antigen receptor (TCR) expression by human peripheral blood CD4-8- alpha/beta T cells demonstrates preferential use of several V beta genes and an invariant TCR alpha chain. *J. Exp. Med.* **1993**, *178*, 1–16. [CrossRef] [PubMed]
175. Kjer-Nielsen, L.; Patel, O.; Corbett, A.J.; Le Nours, J.; Meehan, B.; Liu, L.; Bhati, M.; Chen, Z.; Kostenko, L.; Reantragoon, R.; et al. MR1 presents microbial vitamin B metabolites to MAIT cells. *Nature* **2012**, *491*, 717–723. [CrossRef] [PubMed]
176. Georgel, P.; Radosavljevic, M.; Macquin, C.; Bahram, S. The non-conventional MHC class I MR1 molecule controls infection by *Klebsiella pneumoniae* in mice. *Mol. Immunol.* **2011**, *48*, 769–775. [CrossRef] [PubMed]
177. Meierovics, A.; Yankelevich, W.J.; Cowley, S.C. MAIT cells are critical for optimal mucosal immune responses during in vivo pulmonary bacterial infection. *Proc. Natl. Acad. Sci. USA* **2013**, *110*, E3119–E3128. [CrossRef] [PubMed]
178. Le Bourhis, L.; Dusseaux, M.; Bohineust, A.; Bessoles, S.; Martin, E.; Premel, V.; Coré, M.; Sleurs, D.; Serriari, N.-E.; Treiner, E.; et al. MAIT cells detect and efficiently lyse bacterially-infected epithelial cells. *PLoS Pathog.* **2013**, *9*, e1003681. [CrossRef] [PubMed]
179. Kurioka, A.; Ussher, J.E.; Cosgrove, C.; Clough, C.; Fergusson, J.R.; Smith, K.; Kang, Y.H.; Walker, L.J.; Hansen, T.H.; Willberg, C.B.; et al. MAIT cells are licensed through granzyme exchange to kill bacterially sensitized targets. *Mucosal Immunol.* **2015**, *8*, 429–440. [CrossRef] [PubMed]
180. Grifoni, A.; Sidney, J.; Zhang, Y.; Scheuermann, R.H.; Peters, B.; Sette, A. A Sequence Homology and Bioinformatic Approach Can Predict Candidate Targets for Immune Responses to SARS-CoV-2. *Cell Host Microbe* **2020**, *27*, 671–680.e2. [CrossRef] [PubMed]
181. Liu, W.J.; Zhao, M.; Liu, K.; Xu, K.; Wong, G.; Tan, W.; Gao, G.F. T-cell immunity of SARS-CoV: Implications for vaccine development against MERS-CoV. *Antivir. Res.* **2017**, *137*, 82–92. [CrossRef] [PubMed]
182. Torracinta, L.; Gogichadze, N.; Tanner, R. Immune mechanisms mediating the heterologous effects of BCG vaccination: A systematic review. *Front. Immunol.* **2025**, *16*, 1567111. [CrossRef] [PubMed]
183. Tran, K.A.; Pernet, E.; Sadeghi, M.; Downey, J.; Chronopoulos, J.; Lapshina, E.; Tsai, O.; Kaufmann, E.; Ding, J.; Divangahi, M. BCG immunization induces CX3CR1hi effector memory T cells to provide cross-protection via IFN-γ-mediated trained immunity. *Nat. Immunol.* **2024**, *25*, 418–431. Erratum in *Nat. Immunol.* **2024**, *25*, 723. https://doi.org/10.1038/s41590-024-01804-y. [CrossRef] [PubMed]
184. Eggenhuizen, P.J.; Ng, B.H.; Chang, J.; Fell, A.L.; Cheong, R.M.Y.; Wong, W.Y.; Gan, P.-Y.; Holdsworth, S.R.; Ooi, J.D. BCG vaccine derived peptides induce SARS-CoV-2 T cell cross-reactivity. *Front. Immunol.* **2021**, *12*, 692729. [CrossRef] [PubMed]
185. Bhattacharya, D.; Cheng, J. 3Drefine: Consistent protein structure refinement by optimizing hydrogen bonding network and atomic-level energy minimization. *Proteins* **2013**, *81*, 119–131. [CrossRef] [PubMed]
186. Janin, J.; Miller, S.; Chothia, C. Surface, subunit interfaces and interior of oligomeric proteins. *J. Mol. Biol.* **1988**, *204*, 155–164. [CrossRef] [PubMed]
187. Zhang, Y.; Skolnick, J. Scoring function for automated assessment of protein structure template quality. *Proteins Struct. Funct. Bioinform.* **2004**, *57*, 702–710. Erratum in *Proteins Struct. Funct. Bioinform.* **2005**, *58*, 505. https://doi.org/10.1002/prot.20359. [CrossRef] [PubMed]
188. Xu, J.; Zhang, Y. How significant is a protein structure similarity with TM-score = 0.5? *Bioinformatics* **2010**, *26*, 889–895. [CrossRef] [PubMed]
189. Bodenreider, C.; Kellershohn, N.; Goldberg, M.E.; Méjean, A. Kinetic analysis of R67 dihydrofolate reductase folding: From the unfolded monomer to the native tetramer. *Biochemistry* **2002**, *41*, 14988–14999. [CrossRef] [PubMed]
190. Luo, H.; Ma, Y.; Bi, J.; Li, Z.; Wang, Y.; Su, Z.; Gerstweiler, L.; Ren, Y.; Zhang, S. Experimental and molecular dynamics simulation studies on the physical properties of three HBc-VLP derivatives as nanoparticle protein vaccine candidates. *Vaccine* **2024**, *42*, 125992. [CrossRef] [PubMed]
191. Cao, M.; Li, Y.; Song, X.; Lu, Z.; Zhai, H.; Qiu, H.; Sun, Y. Broad-spectrum vaccines against various and evolving viruses: From antigen design to nanoparticle delivery. *J. Virol.* **2025**, *99*, e00997-25. [CrossRef] [PubMed]
192. Ross, K.A.; Kelly, S.; Phadke, K.S.; Peroutka-Bigus, N.; Fasina, O.; Siddoway, A.; Mallapragada, S.K.; Wannemuehler, M.J.; Bellaire, B.H.; Narasimhan, B. Next-generation nanovaccine induces durable immunity and protects against SARS-CoV-2. *Acta Biomater.* **2024**, *183*, 318–329. [CrossRef] [PubMed]
193. Kyte, J.; Doolittle, R.F. A simple method for displaying the hydropathic character of a protein. *J. Mol. Biol.* **1982**, *157*, 105–132. [CrossRef] [PubMed]
194. Ikai, A. Thermostability and aliphatic index of globular proteins. *J. Biochem.* **1980**, *88*, 1895–1898. [CrossRef] [PubMed]
195. Imon, R.R.; Samad, A.; Alam, R.; Alsaiari, A.A.; Talukder, M.E.K.; Almehmadi, M.; Ahammad, F.; Mohammad, F. Computational formulation of a multiepitope vaccine unveils an exceptional prophylactic candidate against Merkel cell polyomavirus. *Front. Immunol.* **2023**, *14*, 1160260. [CrossRef] [PubMed]
196. Magnan, C.N.; Baldi, P. SSpro/ACCpro 5: Almost perfect prediction of protein secondary structure and relative solvent accessibility using profiles, machine learning and structural similarity. *Bioinformatics* **2014**, *30*, 2592–2597. [CrossRef] [PubMed]

197. Martinelli, D. In silico vaccine design: A tutorial in immunoinformatics. *Healthc. Anal.* **2022**, *2*, 100044. [CrossRef]
198. Ullah, N.; Anwer, F.; Ishaq, Z.; Siddique, A.; Shah, M.A.; Rahman, M.; Rahman, A.; Mao, X.; Jiang, T.; Lee, B.L.; et al. In silico designed Staphylococcus aureus B-cell multi-epitope vaccine did not elicit antibodies against target antigens suggesting multi-domain approach. *J. Immunol. Methods* **2022**, *504*, 113264. [CrossRef] [PubMed]
199. Shah, M.; Moon, S.U.; Shin, J.-Y.; Choi, J.-H.; Kim, D.; Woo, H.G. Pan-variant SARS-CoV-2 vaccines induce protective immunity by targeting conserved epitopes. *Adv. Sci.* **2025**, *12*, 2409919. [CrossRef] [PubMed]
200. Sen, G.C.; Sarkar, S.N. Transcriptional signaling by double-stranded RNA: Role of TLR3. *Cytokine Growth Factor Rev.* **2005**, *16*, 1–14. [CrossRef] [PubMed]
201. Patra, R.; Das, N.C.; Mukherjee, S. Targeting human TLRs to combat COVID-19: A solution? *J. Med. Virol.* **2020**, *93*, 615–617. [CrossRef] [PubMed]
202. Petes, C.; Odoardi, N.; Gee, K. The Toll for trafficking: Toll-like receptor 7 delivery to the endosome. *Front. Immunol.* **2017**, *8*, 1075. [CrossRef] [PubMed]
203. Choudhury, A.; Das, N.C.; Patra, R.; Mukherjee, S. In silico analyses on the comparative sensing of SARS-CoV-2 mRNA by the intracellular TLRs of humans. *J. Med. Virol.* **2021**, *93*, 2476–2486. [CrossRef] [PubMed]
204. Solanich, X.; Vargas-Parra, G.; van der Made, C.I.; Simons, A.; Schuurs-Hoeijmakers, J.; Antolí, A.; del Valle, J.; Rocamora-Blanch, G.; Setién, F.; Esteller, M.; et al. Genetic screening for TLR7 variants in young and previously healthy men with severe COVID-19. *Front. Immunol.* **2021**, *12*, 719115. [CrossRef] [PubMed]
205. Zheng, M.; Karki, R.; Williams, E.P.; Yang, D.; Fitzpatrick, E.; Vogel, P.; Jonsson, C.B.; Kanneganti, T.-D. TLR2 senses the SARS-CoV-2 envelope protein to produce inflammatory cytokines. *Nat. Immunol.* **2021**, *22*, 829–838. [CrossRef] [PubMed]
206. Scheuplein, V.A.; Seifried, J.; Malczyk, A.H.; Miller, L.; Höcker, L.; Vergara-Alert, J.; Dolnik, O.; Zielecki, F.; Becker, B.; Spreitzer, I.; et al. High secretion of interferons by human plasmacytoid dendritic cells upon recognition of Middle East respiratory syndrome coronavirus. *J. Virol.* **2015**, *89*, 3859–3869. [CrossRef] [PubMed]
207. Bortolotti, D.; Gentili, V.; Rizzo, S.; Schiuma, G.; Beltrami, S.; Strazzabosco, G.; Fernandez, M.; Caccuri, F.; Caruso, A.; Rizzo, R. TLR3 and TLR7 RNA Sensor Activation during SARS-CoV-2 Infection. *Microorganisms* **2021**, *9*, 1820. [CrossRef] [PubMed]
208. Cardoso, W.B.; Mendanha, S.A. Molecular dynamics simulation of docking structures of SARS-CoV-2 main protease and HIV protease inhibitors. *J. Mol. Struct.* **2021**, *1225*, 129143. [CrossRef] [PubMed]
209. Sarkar, I.; Sen, A. In silico screening predicts common cold drug Dextromethorphan along with Prednisolone and Dexamethasone can be effective against novel Coronavirus disease (COVID-19). *J. Biomol. Struct. Dyn.* **2022**, *40*, 3706–3710. [CrossRef] [PubMed]
210. Ali, S.A.; Hassan, M.I.; Islam, A.; Ahmad, F. A review of methods available to estimate solvent-accessible surface areas of soluble proteins in the folded and unfolded states. *Curr. Protein Pept. Sci.* **2014**, *15*, 456–476. [CrossRef] [PubMed]
211. Chikalov, I.; Yao, P.; Moshkov, M.; Latombe, J.C. Learning probabilistic models of hydrogen bond stability from molecular dynamics simulation trajectories. *BMC Bioinform.* **2011**, *12*, S34. [CrossRef] [PubMed]
212. Castiglione, F.; Duca, K.; Jarrah, A.; Laubenbacher, R.; Hochberg, D.; Thorley-Lawson, D. Simulating Epstein-Barr virus infection with c-ImmSim. *Bioinformatics* **2007**, *23*, 1371–1377. [CrossRef] [PubMed]
213. Mancini, E.; Quax, R.; De Luca, A.; Fidler, S.; Stohr, W.; Sloot, P.M.A. A study on the dynamics of temporary HIV treatment to assess the controversial outcomes of clinical trials: An in-silico approach. *PLoS ONE* **2018**, *13*, e0200892. [CrossRef] [PubMed]
214. von Eichborn, J.; Woelke, A.L.; Castiglione, F.; Preissner, R. VaccImm: Simulating peptide vaccination in cancer therapy. *BMC Bioinform.* **2013**, *14*, 127. [CrossRef] [PubMed]
215. Pappalardo, F.; Fichera, E.; Paparone, N.; Lombardo, A.; Pennisi, M.; Russo, G.; Leotta, M.; Pappalardo, F.; Pedretti, A.; De Fiore, F.; et al. A computational model to predict the immune system activation by citrus-derived vaccine adjuvants. *Bioinformatics* **2016**, *32*, 2672–2680. [CrossRef] [PubMed]
216. Santoni, D.; Pedicini, M.; Castiglione, F. Implementation of a regulatory gene network to simulate the TH1/2 differentiation in an agent-based model of hypersensitivity reactions. *Bioinformatics* **2008**, *24*, 1374–1380. [CrossRef] [PubMed]
217. Tieri, P.; Prana, V.; Colombo, T.; Santoni, D.; Castiglione, F. Multi-scale simulation of T helper lymphocyte differentiation. In *Advances in Bioinformatics and Computational Biology*; Springer International Publishing: Berlin/Heidelberg, Germany, 2014; pp. 123–134. [CrossRef]
218. Sarvmeili, J.; Baghban Kohnehrouz, B.; Gholizadeh, A.; Shanehbandi, D.; Ofoghi, H. Immunoinformatics design of a structural proteins driven multi-epitope candidate vaccine against different SARS-CoV-2 variants based on fynomer. *Sci. Rep.* **2024**, *14*, 10297. Erratum in *Sci. Rep.* **2024**, *14*, 30524. https://doi.org/10.1038/s41598-024-82829-2. [CrossRef] [PubMed]
219. Khan, M.T.; Islam, M.J.; Parihar, A.; Islam, R.; Jerin, T.J.; Dhote, R.; Ali, M.A.; Laura, F.K.; Halim, M.A. Immunoinformatics and molecular modeling approach to design universal multi-epitope vaccine for SARS-CoV-2. *Inform. Med. Unlocked* **2021**, *24*, 100578. [CrossRef] [PubMed]
220. Invenção, M.d.C.V.; de Macêdo, L.S.; de Moura, I.A.; Santos, L.A.B.d.O.; Espinoza, B.C.F.; de Pinho, S.S.; Leal, L.R.S.; dos Santos, D.L.; Marcos, B.d.F.S.; Elsztein, C.; et al. Design and Immune Profile of Multi-Epitope Synthetic Antigen Vaccine Against SARS-CoV-2: An In Silico and In Vivo Approach. *Vaccines* **2025**, *13*, 149. [CrossRef] [PubMed]

221. Yilmaz, I.C.; Ipekoglu, E.M.; Bulbul, A.; Turay, N.; Yildirim, M.; Evcili, I.; Yilmaz, N.S.; Guvencli, N.; Aydin, Y.; Gungor, B.; et al. Development and preclinical evaluation of virus-like particle vaccine against COVID-19 infection. *Allergy* **2022**, *77*, 258–270. [CrossRef] [PubMed]
222. Gao, Y.; Wang, W.; Yang, Y.; Zhao, Q.; Yang, C.; Jia, X.; Liu, Y.; Zhou, M.; Zeng, W.; Huang, X.; et al. Developing next-generation protein-based vaccines using high-affinity glycan ligand-decorated glyconanoparticles. *Adv. Sci.* **2023**, *10*, e2204598. [CrossRef] [PubMed]
223. He, L.; Lin, X.; Wang, Y.; Abraham, C.; Sou, C.; Ngo, T.; Zhang, Y.; Wilson, I.A.; Zhu, J. Single-component, self-assembling protein nanoparticles presenting the receptor-binding domain and stabilized spike as SARS-CoV-2 vaccine candidates. *Sci. Adv.* **2021**, *7*, eabf1591. [CrossRef] [PubMed]
224. Cohen, A.A.; Keeffe, J.R.; Schiepers, A.; Dross, S.E.; Greaney, A.J.; Rorick, A.V.; Gao, H.; Gnanapragasam, P.N.; Fan, C.; West, A.P.; et al. Mosaic sarbecovirus nanoparticles elicit cross-reactive responses in pre-vaccinated animals. *Cell* **2024**, *187*, 5554–5571.e19. [CrossRef] [PubMed]
225. Cohen, A.A.; van Doremalen, N.; Greaney, A.J.; Andersen, H.; Sharma, A.; Starr, T.N.; Keeffe, J.R.; Fan, C.; Schulz, J.E.; Gnanapragasam, P.N.P.; et al. Mosaic RBD nanoparticles protect against challenge by diverse sarbecoviruses in animal models. *Science* **2022**, *377*, eabq0839. [CrossRef] [PubMed]
226. Wang, E.; Cohen, A.A.; Caldera, L.F.; Keeffe, J.R.; Rorick, A.V.; Adia, Y.M.; Gnanapragasam, P.N.P.; Bjorkman, P.J.; Chakraborty, A.K. Designed mosaic nanoparticles enhance cross-reactive immune responses in mice. *Cell* **2025**, *188*, 1036–1050.e11. [CrossRef] [PubMed]
227. Desai, N. Challenges in development of nanoparticle-based therapeutics. *AAPS J.* **2012**, *14*, 282–295. [CrossRef] [PubMed]
228. Abdullah, T.; Bhatt, K.; Eggermont, L.J.; O'Hare, N.; Memic, A.; Bencherif, S.A. Supramolecular self-assembled peptide-based vaccines: Current state and future perspectives. *Front. Chem.* **2020**, *8*, 598160. [CrossRef] [PubMed]
229. Aggeli, A.; Bell, M.; Carrick, L.M.; Fishwick, C.W.; Harding, R.; Mawer, P.J.; Radford, S.E.; Strong, A.E.; Boden, N. pH as a trigger of peptide beta-sheet self-assembly and reversible switching between nematic and isotropic phases. *J. Am. Chem. Soc.* **2003**, *125*, 9619–9628. [CrossRef] [PubMed]
230. Kaur, H.; Sharma, P.; Patel, N.; Pal, V.K.; Roy, S. Accessing highly tunable nanostructured hydrogels in a short ionic complementary peptide sequence via pH trigger. *Langmuir* **2020**, *36*, 12107–12120. [CrossRef] [PubMed]
231. O'Neill, C.L.; Shrimali, P.C.; Clapacs, Z.E.; Files, M.A.; Rudra, J.S. Peptide-based supramolecular vaccine systems. *Acta Biomater.* **2021**, *133*, 153–167. [CrossRef] [PubMed]
232. Salaikumaran, M.R.; Kasamuthu, P.S.; Aathmanathan, V.S.; Burra, V.L.S.P. An in silico approach to study the role of epitope order in the multi-epitope-based peptide (MEBP) vaccine design. *Sci. Rep.* **2022**, *12*, 12584. [CrossRef] [PubMed]
233. Nezafat, N.; Sadraeian, M.; Rahbar, M.R.; Khoshnoud, M.J.; Mohkam, M.; Gholami, A.; Banihashemi, M.; Ghasemi, Y. Production of a novel multi-epitope peptide vaccine for cancer immunotherapy in TC-1 tumor-bearing mice. *Biologicals* **2015**, *43*, 11–17. [CrossRef] [PubMed]
234. Alharbi, N.; Skwarczynski, M.; Toth, I. The influence of component structural arrangement on peptide vaccine immunogenicity. *Biotechnol. Adv.* **2022**, *60*, 108029. [CrossRef] [PubMed]
235. Eskandari, S.; Pattinson, D.J.; Stephenson, R.J.; Groves, P.L.; Apte, S.H.; Sedaghat, B.; Chandurudu, S.; Doolan, D.L.; Toth, I. Influence of physicochemical properties of lipopeptide adjuvants on the immune response: A rationale for engineering a potent vaccine. *Chem.—A Eur. J.* **2018**, *24*, 9892–9902. [CrossRef] [PubMed]
236. Eskandari, S.; Stephenson, R.J.; Fuaad, A.A.; Apte, S.H.; Doolan, D.L.; Toth, I. Synthesis and characterisation of self-assembled and self-adjuvanting asymmetric multi-epitope lipopeptides of ovalbumin. *Chem.—A Eur. J.* **2015**, *21*, 1251–1261. [CrossRef] [PubMed]
237. Ang, J.; Ma, D.; Jung, B.T.; Keten, S.; Xu, T. Sub-20 nm stable micelles based on a mixture of coiled-coils: A platform for controlled ligand presentation. *Biomacromolecules* **2017**, *18*, 3572–3580. [CrossRef] [PubMed]
238. Raymond, D.M.; Nilsson, B.L. Multicomponent peptide assemblies. *Chem. Soc. Rev.* **2018**, *47*, 3659–3720. [CrossRef] [PubMed]
239. Kapadia, C.H.; Tian, S.; Perry, J.L.; Luft, J.C.; DeSimone, J.M. Role of linker length and antigen density in nanoparticle peptide vaccine. *ACS Omega* **2019**, *4*, 5547–5555. [CrossRef] [PubMed]
240. Skwarczynski, M.; Toth, I. Peptide-based synthetic vaccines. *Chem. Sci.* **2016**, *7*, 842–854. [CrossRef] [PubMed]
241. Shah, M.; Rafiq, S.; Woo, H.G. Challenges and considerations in multi-epitope vaccine design surrounding toll-like receptors. *Trends Pharmacol. Sci.* **2024**, *45*, 1104–1118. [CrossRef] [PubMed]
242. Hussein, W.M.; Xu, J.; Simerska, P.; Toth, I. Synthesis of multicomponent peptide-based vaccine candidates against Group A Streptococcus. *Aust. J. Chem.* **2017**, *70*, 184–190. [CrossRef]
243. Rossino, G.; Marchese, E.; Galli, G.; Verde, F.; Finizio, M.; Serra, M.; Linciano, P.; Collina, S. Peptides as therapeutic agents: Challenges and opportunities in the green transition era. *Molecules* **2023**, *28*, 7165. [CrossRef] [PubMed]
244. Antonelli, A.; Palma, F. Nanocarrier-based delivery systems for natural compounds across research stages. *Materials* **2025**, *18*, 4960. [CrossRef] [PubMed]

245. Liu, M.; Svirskis, D.; Proft, T.; Loh, J.; Yin, N.; Li, H.; Li, D.; Zhou, Y.; Chen, S.; Song, L.; et al. Progress in peptide and protein therapeutics: Challenges and strategies. *Acta Pharm. Sin. B* **2025**, *15*, 6342–6381. [CrossRef] [PubMed]
246. Bi, Y.; Xie, S.; Li, Z.; Dong, S.; Teng, L. Precise nanoscale fabrication technologies, the "last mile" of medicinal development. *Acta Pharm. Sin. B* **2025**, *15*, 2372–2401. [CrossRef] [PubMed]

Disclaimer/Publisher's Note: The statements, opinions and data contained in all publications are solely those of the individual author(s) and contributor(s) and not of MDPI and/or the editor(s). MDPI and/or the editor(s) disclaim responsibility for any injury to people or property resulting from any ideas, methods, instructions or products referred to in the content.